

UC Berkeley

UC Berkeley Electronic Theses and Dissertations

Title

Novel valleytronics in IV-VI monochalcogenides

Permalink

<https://escholarship.org/uc/item/1t2851c1>

Author

Lin, Shuren

Publication Date

2019

Peer reviewed|Thesis/dissertation

Novel valleytronics in IV-VI monochalcogenides

By

Shuren Lin

A dissertation submitted in partial satisfaction of the
requirements for the degree of

Doctor of Philosophy

in

Engineering – Materials Science and Engineering

in the

Graduate Division

of the

University of California, Berkeley

Committee in charge:

Professor Jie Yao, Chair

Professor Junqiao Wu

Professor Ming C. Wu

Summer 2019

Novel valleytronics in IV-VI monochalcogenides

Copyright © 2019

by

Shuren Lin

Abstract

Novel valleytronics in IV-VI monochalcogenides

by

Shuren Lin

Doctor of Philosophy in Materials Science and Engineering

University of California, Berkeley

Professor Jie Yao, Chair

Since its inception, the field of valleytronics has always carried the hopes of generating an additional degree of freedom to electronic and spintronic devices, allowing complementary usage of these functions in a single device and hence greatly increasing the processing power. However, several candidates that presumably possess potential in valley manipulation have since fall short of being practical.

Valleytronics is the control of population at “valleys” of certain qualifying materials, and valleys are essentially different conduction band minima or, in general, band gaps that can be distinctively selected by certain selection rules. In diamond-structured materials, this means forcing electrons out of one of the three pairs of degenerate conduction band minima along $\langle 100 \rangle$ by magnetic or electric field. For transition metal dichalcogenides, this means using circularly polarized light to selectively excite one of the two band gaps at the $\pm K$ points. Both systems require some sort of bias, low temperature, and/ or stringent material quality/ size, making them impractical.

Following the hype on layered materials, from graphene to transition metal dichalcogenides, and anisotropic materials, such as black phosphorus, we decided to explore a close analogue in IV-VI systems. Anisotropy is rather common, but IV-VI systems have the unique additional attribute of having two local band gaps that are along high symmetry lines in reciprocal space. Because the global band gap is not at a high symmetry point, the two relevant band gaps becomes significant and the behaviour near these band edges are then well-defined and well-separated by symmetry due to the anisotropic nature of the bandstructure.

Using bulk Tin (II) Sulfide (SnS) as a novel system, we found that the two band gaps along ΓX (smaller energy) and ΓY (larger energy) are respectively only excited by light polarized along the x (zigzag) and y (armchair) directions. The implication of this is that we now have a valleytronic system that is inherently polarized and can be activated via light-matter interaction without material or experimental conditional constraints. The non-degeneracy in the band gap values also means that we can decouple the valley degree of freedom with the excitation energy, making the system more robust.

Theoretical efforts have allowed us to understand this novel form of valleytronics behaviour. We found that the conduction band minima are predominantly made up of 5p orbitals from Sn, while the valence band maxima are mainly composed of 3p orbitals of S atoms. The exact symmetries of the orbitals that make up the bands allow the simplification of transition dipole moment integral analyses, which gives the selection rules.

As a proof of concept that such valleytronics can be generalized, we also investigated the effect on $\text{SnS}_x\text{Se}_{1-x}$ and showed both the tunability of both band gaps as well as the retainment of the valleytronics effect across the compositions. The band gap tunability is continuous, a consequence of the hybridization of Se 4p orbitals and S 3p orbitals. Similarly, the retainment of symmetry across all compositions means that the polarization degree, an important figure of merit in valleytronic system, is not compromised.

Finally, we fabricated optoelectronic devices out of SnS with the general configuration of photodetectors, where two pairs of electrodes were placed along the x and y axes respectively. We then subsequently probed the photocurrent of the devices with a combination of excitation wavelengths (above, in between, and below the two band gaps), excitation polarization (along x and y), and current direction (along x and y), obtaining distinctly different photocurrent response. This is the first demonstration of a device that utilizes the valleytronics effect to control current flow, paving the way to a multi-digit switch that can provide additional degrees of freedom per device. Through this multi-digit device, we also identified the key limitations and fundamental mechanisms contributing to the lack of perfect valleytronics selectivity in the photoresponse and propose critical areas of improvements of the system.

In conclusion, we identified a novel form of valleytronics that is more practical than its previous counterpart. Our demonstration includes light-matter interaction and photoresponse of SnS, and also generalization in the $\text{SnS}_x\text{Se}_{1-x}$ system. We acknowledge the limitations of our system but remain optimistic about the potential of such a form of symmetry-driven valleytronics, specifically when key limitations such as growth methods are solved, and/ or the quest of multifunctional materials have been fulfilled.

To my parents,

Lim Chin Aik
and
Ng Kwee Hiong

Contents

List of Figures	vi
List of Tables	xiv
Acknowledgements	xv
1. Introduction.....	1
1.1. Review on valleytronics.....	1
1.1.1. Valleytronics in diamond-structured materials	2
1.1.2. Valleytronics in transition metal dichalcogenides (TMDCs)	2
1.1.3. Origin of selection rules in monolayer TMDCs	3
1.2. Motivation	4
1.2.1. Current limitations in valleytronics systems.....	4
2. Demonstration of novel valleytronics in Tin(II) Sulfide (SnS).....	6
2.1. Bulk Tin(II) Sulfide (SnS) as a valleytronics material.....	6
2.1.1. Transitioning from TMDCs – the search for a complementary valleytronics system.....	6
2.1.1.1. Black phosphorus (BP) as a representative two-dimensional (2D) anisotropic material.....	6
2.1.1.2. Monolayer IV-VI monochalcogenides as BP analogues	7
2.1.1.3. Bandstructures of IV-VI monochalcogenides.....	8
2.1.2. Manifestation of valleytronics in SnS - Redefining the term “valley”	9
2.1.2.1. Selection rules in bulk SnS using Group Theory and symmetry	9
2.1.2.2. Detour: Application of selection rules in monolayer SnS	11
2.1.2.3. Detour: Application of selection rules in TMDCs – alternative way of understanding TMDCs valleytronics	11
2.2. Synthesis of bulk SnS plates	13
2.2.1. Experimental setup and procedures.....	13
2.2.2. Trends in varying parameters for SnS synthesis	14
2.2.3. Physical Vapor Deposition (PVD).....	15
2.2.4. Chemical Vapor Deposition (CVD).....	16
2.3. Accessing valley degree of freedom via optical means.....	16
2.3.1. Experimental setup and procedures.....	16

2.3.2. Identification of main crystal axes.....	17
2.3.2.1. Identifying facets of grown SnS plates via surface energy arguments	17
2.3.2.2. Raman measurements.....	18
2.3.3. White light reflection (R) and transmission (T) measurements.....	19
2.3.3.1. Determining absorption coefficient and degree of optical dichroic anisotropy from R and T of samples on substrates	21
2.3.3.2. Variations of band gaps with temperature.....	22
2.3.3.3. Estimating sample thickness from R and T of samples on substrates.....	23
2.3.4. Photoluminescence (PL) measurements	24
2.3.4.1. Polarization degrees.....	25
2.4. Concluding remarks	26
3. Generalization of valleytronics effect to IV-VI monochalcogenides – Tuneable valleytronics in SnS_xSe_{1-x} alloy system	28
3.1. Motivation for generalization - SnS _x Se _{1-x} as a model system	28
3.2. Synthesis of bulk SnS _x Se _{1-x} plates	29
3.2.1. Experimental procedures - Physical Vapor Deposition (PVD)	29
3.2.2. Material characterization.....	29
3.2.3. Limitations in alloying using PVD	30
3.3. Symmetry-dependent valleytronics demonstrated via optical means.....	31
3.3.1. Experimental procedures.....	31
3.3.2. Raman measurements – variations in Raman modes across alloy compositions	32
3.3.3. White light reflection (R) and transmission (T) measurements.....	33
3.3.3.1. Tunability of band gaps.....	33
3.3.4. Photoluminescence (PL) measurements	34
3.3.4.1. Vegard’s Law and Polarization degrees.....	35
3.3.4.2. Trends in PL peaks’ intensity and full-width at half-maximum (FWHM) across alloy compositions.....	36
3.3.4.4. Excitation power-dependent measurements.....	36
3.4. Theoretical validations via analysis of SnS _x Se _{1-x} band diagrams.....	37
3.4.1. Incremental variations in bandgap values at both valleys.....	40
3.4.2. Retainment of symmetry and selection rules of conduction and valence bands at both valleys.....	41
3.5. Concluding remarks	42

4. Engineering multi-digit devices based on valleytronics principles	43
4.1. Device work and transport measurements of SnS	43
4.2. Reading valley polarization via optoelectronic means.....	43
4.2.1. Utilization of light-matter interaction for anisotropic transport properties.....	43
4.2.2. Experimental setup.....	44
4.2.3. Design of multi-digit device.....	44
4.2.3. Basic material and device characterization	45
4.2.3.1. Electric field distribution in SnS based on shape of electrodes.....	47
4.3. Multi-digit device based on valleytronics	48
4.3.1. General power-dependent photocurrent trends	48
4.3.2. Biexponential, fast and slow switching times	49
4.3.3. Identification of multiple states.....	50
4.3.3.1. Signal to noise ratio	51
4.3.3.2. Non-ideal manifestation of valley selectivity in photoresponse.....	52
4.3.4. Key performance of device characterized as a photodetector	52
4.3.4.1. Responsivity	52
4.3.4.2. Differential responsivity, ΔR	53
4.3.4.3. Specific detectivity	54
4.3.4.4. External quantum efficiency, η	55
4.3.4.5. Noise equivalent power, NEP	55
4.3.5. Power-dependent I_p and relation to recombination mechanism	56
4.4. Understanding fundamental mechanisms effecting photoresponse.....	57
4.4.1. Temperature-dependent I_p	57
4.4.1.1. Key temperature-dependent photoresponse features	58
4.4.2. Analysis of I_p -contributing mechanisms.....	59
4.4.2.1. Relating slow rising and decay times	61
4.4.2.2. Relating fast rising and decay times	61
4.4.2.3. Attributing switching times to fundamental mechanisms	61
4.4.2.4. Contributions of valley excitation to selectivity in I_p	62
4.4.2.5. Quantifying trap states.....	62
4.5. Concluding remarks	63
5. Outlook and future directions	64

5.1. Review of work in this thesis and limitations	64
5.1.1. Summary of Chapter 1	64
5.1.2. Summary of Chapter 2	64
5.1.3. Summary of Chapter 3	65
5.1.4. Summary of Chapter 4	65
5.2. Potential improvements in synthesis	66
5.2.1. Monolayer SnS and its advantageous attributes	66
5.2.2. Synthesis of other members of IV-VI monochalcogenides	66
5.3. Identification of symmetry-driven valleytronics in other material systems	67
5.3.1. Truly multifunctional material systems	67
5.4. Revealing fundamental valleytronics mechanisms in SnS	67
5.4.1. Time-resolved PL (TRPL) measurements	68
5.4.2. Transient absorption (TA) measurements	68
References	70

List of Figures

Figure 1: Brilluoin zone of a typical diamond-structured material, showing the presence of 3 degenerate valleys (adapted from [7]) 2

Figure 2: (a) Crystal structure and unit cell of a monolayer TMDC, showing the lack of inversion symmetry and the presence of six \mathbf{K} points in reciprocal space. The \mathbf{K} points are energy degenerate and is further separated into alternating $+K$ and $-K$ points by valley selection rules. (b) Schematic showing selection rules in monolayer TMDCs, where $-K$ ($+K$) valleys can only be excited by σ^- (σ^+) circularly polarized light and only spin up (down) electrons can be excited at the $-K$ ($+K$) valleys. (adapted from [1]) 3

Figure 3: (a) Optical microscopy image of a MoS_2 monolayer flake, showing the unpredictability of exfoliated samples. (b) Temperature-dependent polarization degrees of monolayer MoS_2 , showing a sharp decrease beyond cryogenic temperatures. (c) Band diagrams showing the breaking of degeneracy of the two valleys of monolayer MoS_2 via the valley Zeeman effect. ((a) and (b) adapted from [14], (c) adapted from [19])..... 5

Figure 4: Calculated band structure of bulk BP, showing a direct band gap at Γ point, but also a local band gap along ΓX (adapted from [20]) 7

Figure 5: (a) A section of the periodic table of elements, showing that the relationship of IV-VI systems and Group V systems, highlighted in red, is analogous to that between III-V systems and Group IV systems, highlighted in blue. (b) Crystal structure of a single layer of BP and IV-VI monochalcogenides, showing the puckered structure. ((a) is adapted from [22], (b) is adapted from [23])..... 7

Figure 6: (c) Calculated band structure of bulk and monolayer IV-VI monochalcogenides. The red and green dots in each bandstructure refers to the global conduction band minimum (CBM) and valence band maximum (VBM). Potential valleytronics materials (with two distinct band gaps at different \mathbf{k} points) are boxed out in red, while other systems did not fulfil the requirement; blue boxes signify global band gap at the Γ point while black box signifies the lack of two band gaps. The bandstructure of SnS and SnSe show two local band gaps along ΓX and ΓY . Both band gaps have smaller energy difference than the local band gap at the Γ point (adapted from [23]) 8

Figure 7: Bandstructure of bulk SnS . The directions y and x are the armchair and zigzag directions, respectively. The respective irreducible representations of the conduction band,

valence band, and position vectors, as well as the point group and two-fold rotation axis, are indicated for each direction (adapted from [8]). 10

Figure 8: Schematic band diagram of monolayer WSe₂, showing the effect of spin splitting on the spinor IRs and the eventual valley selection rules at -K and +K. The green arrow shows that the x (in-plane) polarized light, with IR of E', is able to excite both valleys. However, only components of E' with IR of Γ_2 (Γ_3) is able to cause excitation at -K and +K respectively. This forms the basis of valley selectivity by circularly polarized light (adapted from [32])..... 13

Figure 9: Schematics of experimental setups for (a) PVD and (b) CVD growths of bulk SnS plates respectively..... 14

Figure 10: $\log(P_v^*)$ against $1/T$ graph of SnS, Sn₂S₃, SnS₂. Dotted overlaid arrow signifies the cooling down of the gas as it moves downstream at a gas pressure within the range of our study, showing that the sequence of supersaturation follows SnS to Sn₂S₃ to SnS₂..... 15

Figure 11: Schematic of the experimental setup for Raman, PL, and reflection (R) measurements. Transmission (T) measurements were conducted with the detection light path on the back side of the sample. Excitation was conducted using linearly polarized laser (for Raman and PL) and white light (for R and T) on a sample that can be rotated to give an angle θ between the polarization axis and the armchair direction. A second polarizer was also placed either parallel or perpendicular to the excitation polarization for Raman and PL measurements (adapted from [8])..... 17

Figure 12: (a) Optical microscopy image of a SnS sample, showing a clear difference in angles made by the edges and ease of identifying the in-plane directions. Scale bar is 10 μ m. Inset shows scanning electron microscopy (SEM) images and energy-dispersive X-ray spectroscopy (EDX) maps, demonstrating a flat surface and homogeneous distribution of Sn and S in equal ratio. (b) Illustration of a Wulff plot, where perpendicular lines are drawn at a distance proportional to the surface energy of the plane normal to each lattice direction. The shape of a grown crystal is the shape of the smaller area or volume enclosed by these lines. ((a) is adapted from [9], (b) is adapted from [40])..... 18

Figure 13: (a) An example of Raman spectra obtained under parallel polarization, showing clear trends in intensities for the A_g and B_{3g} modes, thus ascertaining the identity and orientation of the measured SnS sample (adapted from [9]). (b) Four polar plots of peak height intensity variations in Raman peaks assigned to either A_g or B_{3g} modes. The intensity

variations follow the trend in published results and allowed us to have a rigorous derivation of the material axes directions (vibration modes adapted from [41]). 19

Figure 14: Reflection and transmission measurements of SnS. White light with wavelengths ranging from 700 to 1050 nm illuminated the sample without a second polarizer (adapted from [8]). 20

Figure 15: Reflection spectra of SnS grown on Si/SiO₂ substrates with sample rotated every 20° for a full θ rotation. Results clearly show that the onset of Fabry-Pérot oscillations for most θ values is at 775nm. When the polarization is aligned exactly to the zigzag direction, the oscillations are fully dampened (presumably because absorption at 775nm is no longer allowed) and another onset of Fabry-Pérot oscillations is shown to be 950nm..... 21

Figure 16: (Left axis) Tauc plots of both directions, with fitting lines denoting band gaps at 1.28 and 1.48 eV for zigzag and armchair directions, respectively. (Right axis) Degree of optical dichroic anisotropy, $\alpha_{\text{zigzag}}/\alpha_{\text{armchair}}$. (adapted from [8])..... 22

Figure 17: (a) Absorption coefficients of both directions under different temperatures, showing a distinct increase in band gap with decreasing temperature. (b) Vashni plot extracted from the temperature varying absorption measurements. ((a) and (b) adapted from [8]). 23

Figure 18: Photoluminescence measurements of SnS. (a) Deconvolutions of PL peaks under parallel polarization at 817 and 995 nm give clear, opposite trends with respect to sample orientation, demonstrating the identity of the valley positions. (b), (c) Polar plots of PL peak height intensities conducted under parallel polarization for the valleys at 817 and 995 nm, respectively (squares). The single circular data point in each polar plot represents the PL peak height intensities of the corresponding measurements conducted with the second polarizer perpendicular to the incident light when the respective axes are aligned to the excitation polarization. The black dashed arrows connect the two data points before and after the 90° rotation of the second polarizer, showing 95% and 96% decrease in PL intensities at the ΓY and ΓX valleys respectively. (adapted from [8]). 25

Figure 19: Optical microscopy image, scanning electron microscopy (SEM) images and Energy-dispersive X-ray spectroscopy (EDX) maps of nominally (a) SnS_{0.875}Se_{0.125}, (b) SnS_{0.75}Se_{0.25}, (c) SnS_{0.625}Se_{0.375}, (d) SnS_{0.5}Se_{0.5}, (e) SnS_{0.375}Se_{0.625}, (f) SnS_{0.25}Se_{0.75}, (g) SnS_{0.125}Se_{0.875}, and (h) SnSe, demonstrating flat surfaces and homogeneous distributions of Sn, S, and Se. Scale bars are 5 μ m. (adapted from [9]). 30

Figure 20: (a) and (b) Peak intensities for S and Se in SEM-EDX spectra. Trends in peak height intensity of (a) Se and (b) S at the respective energies of 1.4eV and 2.3eV, showing a general trend of increasing (decreasing) intensity with more Se content for the Se (S) peak. (c) Trend in actual composition versus nominal (design) composition, showing a general excess of Se content. (adapted from [9]). 31

Figure 21: Reflection mode, $c(xx)c^-$ Raman spectra. The first and second letters in the parentheses denotes the alignment of the incident light and emitted signal. Only spectra aligned along x and y directions are presented. (a) Raman spectra obtained under parallel polarization using 532nm excitation, showing clear trends in intensities for the A_g modes, thus ascertaining the identity and orientation of the measured samples. (b) Raman spectra obtained under cross polarization using 532nm excitation, showing clear trends in intensities for the B_{3g} modes. (c) Raman spectra obtained under parallel polarization using 785nm excitation aligned along the y axis, showing two-mode behavior for the $A_g^{(3)}$ mode. (adapted from [9])..... 32

Figure 22: Normalized Tauc plots of both directions for different alloy compositions obtained from white light R and T measurements, showing a distinct decrease in bandgap value with increasing Se content. (adapted from [9]). 33

Figure 23: PL peaks under parallel polarization. Only spectra aligned along x and y directions are presented, showing that for all alloy compositions, the high (low) energy peak has the strongest intensity when the excitation light is polarized along the y (x) direction, showing the retainment of valley selectivity across all alloy compositions. There is also a clear trend of decrease in bandgap value with increasing Se content. (adapted from [9]). 34

Figure 24: (a) Optical bandgaps obtained by white light R and T as well as PL measurements, plotted with fitting functions using Vegard's law. Calculated bandgap values are presented in the inset, showing a smooth variation and similar trends for both ΓY and ΓX valleys respectively. (b) Trends in polarization degrees with compositional variation, showing the retainment of high valley selectivity across all alloy compositions in SnS_xSe_{1-x} . Intervalley (intravalley) polarization degrees are presented as squares (circles), with dashed (dotted) lines demarcating the respective average values. Solid and open data points denotes the polarization degrees that depends predominantly on PL signals of the ΓY and ΓX valleys respectively. (adapted from [9]) 35

Figure 25: Nature of bandgap transitions in SnS_xSe_{1-x} . (a) Trends in FWHM (darker shade) for the ΓY peak with compositional variation, showing an increasing trend with more Se respectively. The exact location of the boundaries of the peak at FWHM is also presented in

a lighter shade. (b) Corresponding trends in FWHM for the ΓX peak. (c) Trends in PL peak height intensity with alloy composition, showing a decreasing trend with more Se (lower x). The intensity for SnS is normalized to one for clarity in presentation. (d) Fitted k coefficient of $IPL \propto I_{excitation} k$, obtained from power dependence PL measurements at the respective peak height positions. $k = 1$ denotes the boundary between the presence and absence of donor/ acceptor assisted exciton recombination. (adapted from [9])..... 36

Figure 26: 2x2 supercells of molecular structures of SnS, SnSe, and the SnS_{0.5}Se_{0.5} alloy with the simplest case of homogeneous alloying. The puckered arrangement of atoms and the high anisotropy along the y (armchair) and x (zigzag) directions is maintained across the whole compositional range while the lattice parameters increase with Se content. (adapted from [9]). 38

Figure 27: Calculated Energy above hull per atom of SnS _{x} Se_{1- x} , showing that the energy above hull difference is within 5 meV/atom for all models used in our calculation (adapted from [9]). 38

Figure 28: Calculated band structures for selected SnS _{x} Se_{1- x} . Orbital projected band structures along $Y-\Gamma-X$ of representative alloy compositions of (a) SnSe, (b) SnS_{0.5}Se_{0.5}, and (c) SnS are presented. Band structures are projected on elements of Sn, S and Se. Red, green, and blue shades correspond to contributions of each subband by p_x , p_y , and p_z orbitals respectively. Our elemental and orbital specific band structures denote that for all alloy compositions, p orbitals from Sn and the chalcogenides make up predominantly the conduction and valence bands, (adapted from [9])..... 39

Figure 29: Calculated bandstructures and density of states (DOS) plots for SnS _{x} Se_{1- x} . The bandstructures and DOS plots for alloys, calculated using unit cells with 32 atoms, are included in (a) SnSe, (b) SnS_{0.125}Se_{0.875}, (c) SnS_{0.375}Se_{0.625}, (d) SnS_{0.5}Se_{0.5}, (e) SnS_{0.625}Se_{0.375}, (f) SnS_{0.875}Se_{0.125}, and (g) SnS. Band structures are projected on elements of Sn, S and Se. Red, green, and blue shades correspond to contributions of each subband by p_x , p_y , and p_z orbitals respectively, (adapted from [9]). 40

Figure 30: Schematic of the anisotropic photocurrent device measured in this work. Three levels of control of the multi-digit switch is envisioned, via (i) the excitation energy (shown to be 650nm and 900nm which corresponds to the above- and between-bandgaps wavelengths respectively), (ii) the excitation polarization (shown to be along either armchair or zigzag to selectively excite the ΓY and ΓX valleys respectively), and (iii) the current detection. Inset is the schematic bandstructure that shows the valley optical selection rules. 44

Figure 31: Semi-quantitative schematic of Tauc plots for SnS along armchair and zigzag directions overlaid with five bands that represent the five wavelength ranges that we employed in this work. The five wavelengths include 650nm ($h\nu > E_{g,Zig}$), 840nm and 900nm ($E_{g,Zig} > h\nu > E_{g,Arm}$), 1090nm ($E_{g,Arm} > h\nu > E_{absorption\ tail}$), and 1300nm ($h\nu < E_{absorption\ tail}$)..... 45

Figure 32: (a) Optical microscopy image of the device, showing that the electrodes are aligned along the armchair and zigzag directions of the SnS microplate respectively. Scale bar is 20 μ m. Inset shows the zoomed-out view of the electrodes. Scale bar is 50 μ m. (b) Reflection mode Raman spectra obtained along both electrode axes under parallel and cross polarizations. Trends in the Raman modes ascertain that the direction along the horizontal (vertical) direction of the image in (a) corresponds to the armchair (zigzag) direction of the SnS microplate and the spectra were labelled according to the axis directions. The first and second letters in the parentheses denotes the alignment of the incident light and emitted signal..... 46

Figure 33: (a) I_{ds} - V_{ds} graphs of the device along armchair and zigzag directions. The straight lines denote that the device remains Ohmic with $V_{ds} = \pm 3V$. (b) I_{ill} were measured using 900nm illumination at the highest power setting of the light source without any polarizer. The linear trend of I_{ill} signifies Ohmic response of the device even under illumination. 47

Figure 34: COMSOL simulations of electric field distributions for various electrode shapes. Three electrode structures were investigated: (a) flat edge, (b) pointed edge, and (c) rounded edge. The radius of curvature of the rounded edge structure was obtained from the actual deposited electrodes in our device. 47

Figure 35: I_{ds} - I_d versus t curve for Z900Zig and Z900Arm, performed with sequentially on-off procedure with five increasing excitation intensities. The I - t relationships show clear biexponential trends upon excitation (rising curve) and deexcitation (decay curve). Valley selectivity is manifested in the distinct $I_{p,Z900Zig}$ - $I_{p,Z900Arm}$ for all excitation intensities..... 48

Figure 36: (a) I_p versus P_{inc} values for current detected along the armchair direction. Valley selectivity is clearly shown as $I_{p,A900Zig} > I_{p,A900Arm}$ and $I_{p,A840Zig} > I_{p,A840Arm}$. Anisotropic absorption is validated by $I_{p,A650Arm} > I_{p,A650Zig}$. Non-zero and similar $I_{p,A1090Arm}$ and $I_{p,A1090Zig}$ shows the presence of in-gap states. (b) I_p versus P_{inc} values for current detected along the zigzag direction, giving similar trends between excitation polarization directions. (a) and (b) gives multiple distinct I_p values at a constant P_{inc} for different configurations. 49

Figure 37: I_{ds} - I_d versus t curves (lighter shades) for Z900Zig and Z900Arm at the highest power setting at room temperature were both fitted with biexponential trends (darker

fits). Both rising and decay profiles fit well with the biexponential fits and they give two, fast and slow, distinct characteristic times..... 50

Figure 38: (a) Rising and (b) decay times for Z900Arm, Z900Zig, Z650Arm, and Z650Zig respectively, showing the presence of a slow and fast time and a general lack of dependence of switching time values on incident light intensities..... 50

Figure 39: Histogram showing I_p of various configurations obtained from Figure 36 and normalized to an incident light intensity of 1.5mWcm^{-2} 51

Figure 40; Histogram of noise. Difference in fitted exponential curves and experimental data was calculated for a representative Z900Zig rising curve at the highest power setting at room temperature. The resulting histogram presents a distribution of noise values, which can then be fitted with a Lorentz distribution to give the noise of our measurements. 52

Figure 41: R versus incident light intensity for electrode direction along (a) armchair and (b) zigzag respectively. 53

Figure 42: Summary of ΔR values for photoresponse of reported anisotropic materials, including black phosphorus, GeAs_2 , and ReSe_2 . ΔR of SnS in this work in the valley-selective regime is orders of magnitude larger than the reported materials and SnS in the non-valley-selective regime..... 54

Figure 43: D^* versus incident light intensity for electrode direction along (a) armchair and (b) zigzag respectively. 55

Figure 44: η versus incident light intensity for electrode direction along (a) armchair and (b) zigzag respectively. 55

Figure 45: NEP versus incident light intensity for electrode direction along (a) armchair and (b) zigzag respectively..... 56

Figure 46: $\ln(I_p)$ versus $\ln(P_{\text{inc}})$ for electrode direction along (a) armchair and (b) zigzag respectively. The exponent $I_p \propto P_{\text{inc}}^\beta$ can be fitted from the slope of the graphs, giving values that ranges from 0.42 to 0.72..... 56

Figure 47: I_{ds} - I_d versus t curves for Z900Zig and Z900Arm, performed with an on-off procedure at the highest excitation intensity of our light source. The same measurement was conducted from 80K to 300K at 20K intervals. Graphs are offset by a fixed magnitude.

..... 58

Figure 48: (a) $(I_{p,Zig}/I_{p,Arm})$ versus T results. $I_{p,Z900Zig}/I_{p,Z900Arm}$ stays relatively constant with a value of ~ 1.3 at low T and rises sharply at $\sim 220K$ to a value of ~ 2.0 at 300K. This increase in selectively can be attributed to the deactivation of a non-selective component with T above $\sim 220K$. $I_{p,Z650Zig}/I_{p,Z650Arm}$ stays close to but slightly lower than 1 at all T , showing the difference in absorption coefficient along armchair and zigzag. (b) Switching time, τ , versus T , showing both fast and slow components of the biexponential fits for both rising and decay curves. The slow component has a relatively T -insensitive τ_{slow} at $\sim 15s$. The fast component remains relatively constant at $\sim 300ms$ at low T but decreases beyond $\sim 220K$ to $\sim 70ms$ at 300K. (c) I_d - T results of the device measured along armchair and zigzag, showing that $I_{d,Z} > I_{d,A}$ for all T . I_d remains low at low T and increases sharply at high T , signifying the typical semiconductor behaviour that transitions from extrinsic to intrinsic conduction regimes as T increases. 59

Figure 49: Analysis of current contributions and correlation to fundamental mechanisms related to recombination/ trap states. (a) Schematic of a typical on-off curve investigated in this work, plotted as I_{ds} - I_d versus t . The photocurrent, I_p , can be viewed from the perspective of a rising curve or decay curve. This rising curve can be decomposed into a fast (1) component that is temporally followed by a slow (2) component. These two processes are characterized by currents, $I_{Rising,fast}$ and $I_{Rising,slow}$, and switching times, $\tau_{Rising,fast}$ and $\tau_{Rising,slow}$, respectively. The decay curve can also be decomposed into a fast (3) component that is temporally followed by a slow (4) component, but also possesses a persistent photocurrent, PPC, (5) component that gives a residual current greater than I_d . These three processes are characterized by currents, $I_{Decay,fast}$, $I_{Decay,slow}$, and I_{PPC} , and switching times, $\tau_{Decay,fast}$, $\tau_{Decay,slow}$ and τ_{PPC} , respectively. Note that τ_{PPC} is modelled as being infinitely large. (b) I - T measurements results for Z900Zig. $I_{Rising,slow}$ is almost identical to $I_{Decay,slow}$ (open squares), demonstrating that the slow components of the rising and decay curves are mirror and reverse process. I_p , $I_{Rising,fast}$ and $I_{Decay,fast}$ (solid squares) tend towards each other beyond $\sim 220K$, showing the diminishing slow process and PCC that can be attributed to deactivate of trap states. (c) I_p - T measurements results for Z900Zig and Z900Arm, showing similar trends of constant values at low T that decreases beyond $\sim 220K$. The difference, $\Delta I_p = I_{p,Z900Zig} - I_{p,Z900Arm}$ is also plotted, giving a constant value independent of T for all T , and can be almost fully attributed to $\Delta I_{Rising,fast}$. This means that the selective component of I_p is mostly due to the fast component. $\Delta I_{Rising,slow}$ is negligible for all T . (d) $\ln(I)$ versus $1/T$ for $I_{Decay,slow}$ and I_{PPC} . The slope of these two curves at T beyond 220K signifies the activation energy, E_A , of trap states based on an Arrhenius relationship.

..... 60

List of Tables

Table 1: Character table for C_{2v} point group for k points along ΓX (top) and ΓY (bottom) (adapted from [6]).....	10
Table 2: Character table of C_{3h} space group (adapted from [21]).....	11
Table 3: Spinor representation of character table of C_{3h} space group (adapted from [22]).	12
Table 4: List of parameters varied for PVD.....	15
Table 5: List of parameters varied for PVD [26].	16

Acknowledgements

I would like to thank my adviser, Prof. Jie Yao, for his hosting me throughout my time as a student in UC Berkeley.

I would like to thank my Qualifying Examinations committee members, Prof. Junqiao Wu, Prof. Ming Wu, Prof. Mark Asta, and Prof. Mary Scott, especially Prof. Junqiao Wu for being the chair of the committee and also the former two members for being in my thesis committee. The suggestions given during and after the QE have been insightful and valuable.

I would like to thank past and present members of the Yao Group in UC Berkeley, specifically people whom I have worked with and/ or given me assistance in one way or another at work, including Shuai Lou, Yin Liu, Rui Chen, Jinhua Cao, Chi So, Cher Yeoh, Shancheng Yan, Fei Zhou, Zixuan Fang, and Lu Lu. Special thanks go to the following: Kyle Tom, for being a responsible first student of the group who took it upon himself to ensure the lab was run smoothly and safely. Roger Li, for being the most hardworking Masters/ undergraduate student I have ever seen and being willing to go above and beyond his call of duty. I would not have been able to finish the synthesis phase of the first project without him sharing half of the workload. Fuyi Yang, for being selfless in agreeing to help out to fix the optical setup and cleaning up the mess even though she was busy and she didn't have to. Ting Wan Hsu, for being committed in the device project and willing to share her knowledge and experience in the field. Discussions with her has greatly expedited the progress of the project. Sujung Kim, for being willing to take on lesser roles with passion in projects and most importantly, for being a great neighbour in the office! Special mention goes to a certain postdoc who shall not be named, whose constant sabotage has motivated me to be an independent researcher.

I would like to all thank my collaborators, including the people responsible for the theoretical calculations in my projects, Alexandra Carvalho, Aleksandr Rodin, Lídia Carvalho, and Prof. Antonio H. Castro Neto from NUS for the first project on SnS as well as Tingzheng Hou and Prof. Kristin Persson for the alloy project. I would specifically want to thank Dr. Emory Chan from LBL for his tremendous support given to me, my project, and the Yao Group in general. Most of the key experimental results in this thesis has been obtained in the Molecular Foundry Inorganic facility. While most of the staff and users there were very welcoming and the atmosphere was always very positive, Emory was the one who actively provided assistance and guidance to users like me. This was very instrument for us getting good work done and I am very grateful for that.

I would like to thank everyone else that I have met throughout my journey here, industrious or indolent, scrupulous or unsavoury, sincere or pious, because pain is temporary, pride is forever.

Last but not least, I would like to thank the MSE department of UC Berkeley, the faculty and staff for providing me with a place that I can call home for my time here.

Chapter One

1. Introduction

1.1. Review on valleytronics

In the past decade, immense interest in the field of two-dimensional (2D) materials has led to a plethora of branch-off topics pertaining to 2D systems, all of which has generated great interest amongst the communities. One of such topics is valleytronics, which has been deeply researched into in the transition metal dichalcogenides (TMDCs) [1] [2]. But what exactly is valleytronics? Also, amidst the hype about its intrigue, why exactly is it significant in the scientific world?

In a general sense, valleytronics can be succinctly defined as the study of multiple “valleys” that exist in the bandstructure of certain materials. For the features to qualify as valleys, they must be distinguishable from and, to a huge degree, independent of each other. The distinction of the valleys obeys certain selection rules, which can be leveraged by the application of an externally applied control bias. In a system with high enough fidelity, the electronic population of different states in the bandstructure can be selected using the said bias, which serves as a means for information storage or switches.

The value of a valleytronic device lies in the promise of providing a complementary mechanism to electronic systems, essentially providing an additional degree of freedom of control. This can potentially provide the answer to the miniaturization of electronic devices, where the current state of research has already brought us way into the nanometer (quantum) regime, and further scaling down to increase the number of devices per unit area to increase processing speed is becoming less viable.

However, even though the idea of valleytronics has been long proposed and the concept, albeit not exactly the same as in TMDCs and our Tin(II) Sulfide (SnS) systems, demonstrated in Si [3] [4], AlAs [5] [6], and recently, diamond [7], practical limitations have impeded much progress in the field. Much like the field of spintronics, which chronologically serves as the bridge between electronics and valleytronics, the concurrent utilization of valley polarization in electronic devices has never been achieved. Barring that, the lack of a robust valleytronics system in terms of polarization stability and ease of control are problems yet to be solved.

This thesis details the discovery of a novel valleytronics system in SnS [8] and, at large, IV-VI monochalcogenides [9]. Compared to previous systems, valleytronics in SnS presents a phenomenologically similar system where valleys can be accessed in a practical way. Such valleytronics is first revealed via light-matter interaction and subsequently demonstrated in an anisotropic optoelectronic device [10].

Due to the difference in physical mechanisms responsible for various valleytronics effect, the rest of the chapter will be devoted to the elaboration of valleytronics in other systems, generically grouped into diamond-structured materials and TMDCs.

1.1.1. Valleytronics in diamond-structured materials

In diamond-structured materials, energy minima of conduction bands (CB) resides along $\langle 100 \rangle$ family of directions. These three pair of energy minima, as shown in the Brilluoin zone (Figure 1 [7]), are inherently degenerate and they are defined as valleys with no relation to the valence band (VB). Valleytronics in such structures thus depends on the selective population of one of these three pairs of CB minima.

Valley splitting has been shown to occur with the application of magnetic field [4] (where it results in 2D confinement in Si, causing the valley along the confinement axis to have the lowest lying states) and electric field [7] (where electrons in valleys along the field axis is heated less than the other axis, leading to hot electrons scattering to repopulate the cooler valleys), both by virtue of the anisotropy in effective mass

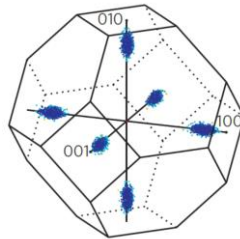


Figure 1: Brilluoin zone of a typical diamond-structured material, showing the presence of 3 degenerate valleys (adapted from [7]).

1.1.2. Valleytronics in transition metal dichalcogenides (TMDCs)

Valleytronics in 2D TMDCs [11] [12] [13] [14] has shown interesting properties, since the absence of inversion symmetry and the presence of time reversal symmetry in 2D TMDCs dictate that the band gaps at the K points in reciprocal space, albeit degenerate, can be classified into two sets of valleys that reside at $+K$ and $-K$ points, shown in Figure 2a [1]; the Berry curvature has opposite signs at the two valleys while the spin of electrons and holes that reside at the CB and VB have to have opposite spins for the two valleys. These lead to spin-valley coupling, where the spin and valley indices are inherently coupled. Thus, the electrons from the VB to CB at $-K$ valleys can only be excited by σ^- circularly polarized light as dictated by the valley index, while at the same time, only spin up states can be excited. Correspondingly, only spin down states at $+K$ valleys can be excited by σ^+ circularly polarized light [1]. This is shown in Figure 2b [1]. This lays the foundation for the selection

rules in 2D TMDCs valleytronics; by using circularly polarized light, each valley can be independently excited.

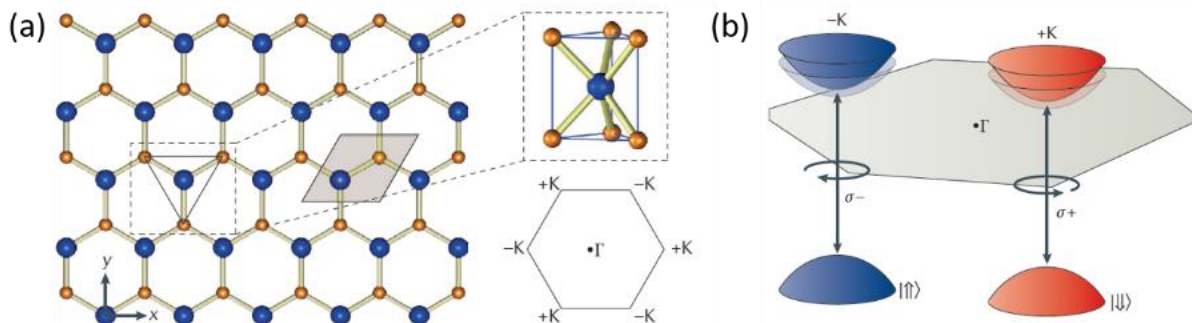


Figure 2: (a) Crystal structure and unit cell of a monolayer TMDC, showing the lack of inversion symmetry and the presence of six \mathbf{K} points in reciprocal space. The \mathbf{K} points are energy degenerate and is further separated into alternating $+K$ and $-K$ points by valley selection rules. (b) Schematic showing selection rules in monolayer TMDCs, where $-K$ ($+K$) valleys can only be excited by σ^- (σ^+) circularly polarized light and only spin up (down) electrons can be excited at the $-K$ ($+K$) valleys. (adapted from [1])

1.1.3. Origin of selection rules in monolayer TMDCs

The above-mentioned selection rules in monolayer originate [13] from the bandstructure composition. Taking MoS_2 as an example, the band edges (CB and VB) of the bandstructure is made up of entirely Mo d orbital bands, which resides in between the bonding and anti-bonding s-p hybridised bands. Since the Mo d bands are partially filled, CB to VB transitions are thus fully determined by the symmetry of the hybridised d orbitals. Since monolayer MoS_2 contains reflection symmetry in the z direction, only A_1 (d_{z^2}) and E ($d_{x^2-y^2}$ and d_{xy}) orbitals can be hybridized while E' (d_{xz} and d_{yz}) orbitals do not form the band edges.

This hybridization of d orbitals opens up a band gap, giving basis functions of the CB and VB to be $|\Phi_c\rangle = |d_{z^2}\rangle$ and $|\Phi_v\rangle = \frac{1}{\sqrt{2}}(|d_{z^2-y^2}\rangle + i\tau|d_{xy}\rangle)$ respectively. τ takes values of ± 1 at $\pm K$ points respectively, also known as the valley indices.

It turns out that the coupling or oscillator strength for optical fields, $P_{\pm}(\mathbf{k})$, with circularly polarization, σ_{\pm} , is calculated as $P_{\pm}(\mathbf{k}) = P_x(\mathbf{k}) \pm iP_y(\mathbf{k})$, where $P_a(\mathbf{k}) = m_0 \left\langle u_c(\mathbf{k}) \left| \frac{1}{\hbar} \frac{\partial H}{\partial k_a} \right| u_v(\mathbf{k}) \right\rangle$. The mathematical derivation of transition probability, $|P_{\pm}(\mathbf{k})|^2$, is presented in [13], knowing the Hamiltonian, essentially approximating $|P_{\pm}(\mathbf{k})|^2$ as a function of $(1 \pm \tau)^2$ when the energy gap is much larger than the product of the lattice parameter, hopping integral, and wavevector. This is generally the case at the $\pm K$ points, which means that transitions are only coupled for one polarization per valley.

The presence of valley-contrasting K points leads to a valley-contrasting Berry curvature, Ω_n [15], a gauge field that is even with inversion symmetry ($\Omega_n(\mathbf{k}) = \Omega_n(-\mathbf{k})$) and odd with

time-reversal symmetry ($\Omega_n(\mathbf{k}) = -\Omega_n(-\mathbf{k})$). Since inversion symmetry is not present in monolayer TMDCs, $\Omega_n(\mathbf{k}) = -\Omega_n(-\mathbf{k})$, Ω_n acts like an effective magnetic field that leads to the observation of the valley Hall effect [16], which follows the aforementioned valley indices.

Another unique feature of valleytronics in monolayer TMDCs that is previously unseen in diamond-structured materials is the presence of robust spin-valley coupling [17]. The robustness of such coupling is due to the fact that it originates from symmetry constraints.

Monolayer TMDCs are known to have strong spin-orbit coupling at each valley, where the CB and VB are split into spin-up and spin-down bands. Spin splitting, or the general lack of spin degeneracy in a band, is also a general consequence of inversion symmetry breaking, which states that $E(\mathbf{k}, \uparrow) \neq E(-\mathbf{k}, \uparrow)$. Since monolayer TMDCs obeys time-reversal symmetry, $E(\mathbf{k}, \uparrow) = E(-\mathbf{k}, \downarrow)$, $E(\mathbf{k}, \uparrow) \neq E(-\mathbf{k}, \downarrow)$ results. Because time-reversal symmetry is obeyed, the spin state of degenerate bands at the $\pm K$ points should be opposite, which means that the CB to VB transition at each valley now only occurs for the opposite spin state, leading to the coupling of the spin and valley indices.

The coupling of spin and valley indices, though robust and interesting, may also be a disadvantage for monolayer TMDCs as valleytronics materials. Since spin and valley indices cannot be separated, the degrees of freedom caused by spin and valley polarization becomes the same. This means that monolayer TMDCs as a valleytronic material does not actually provide an additional means of control on top of its spintronic capabilities.

1.2. Motivation

1.2.1. Current limitations in valleytronics systems

While 2D TMDCs, given the strong exciton binding energy and spin-orbit coupling, has been shown to possess previously unseen valley physics [18], fundamental issues remain. We note that experiments conducted to probe such valley effects are extremely impractical.

First, the need for monolayer [13] [14](or any odd-layered 2D) TMDCs makes sample preparation unpredictable. Monolayer samples are often of lower quality and low reproducibility in terms of size and defect levels (Figure 3a [14]). Furthermore, the exfoliation processes often used to generate monolayers are very time consuming.

Second, due to strong phonon-assisted scattering, cryogenic temperatures are often required to observe the valley effects (Figure 3b [14]) [11] [12]. All these render the material system only suitable as proofs of concept and rather impractical for real applications.

Third, energy degeneracy of the valleys means that strong biases such as magnetic fields, used to split the CB and VB via the valley Zeeman effect (Figure 3c [19]), has to be applied to clearly distinguish the two valleys [19]. In this sense, the valley degree of freedom becomes inaccessible without such biases.

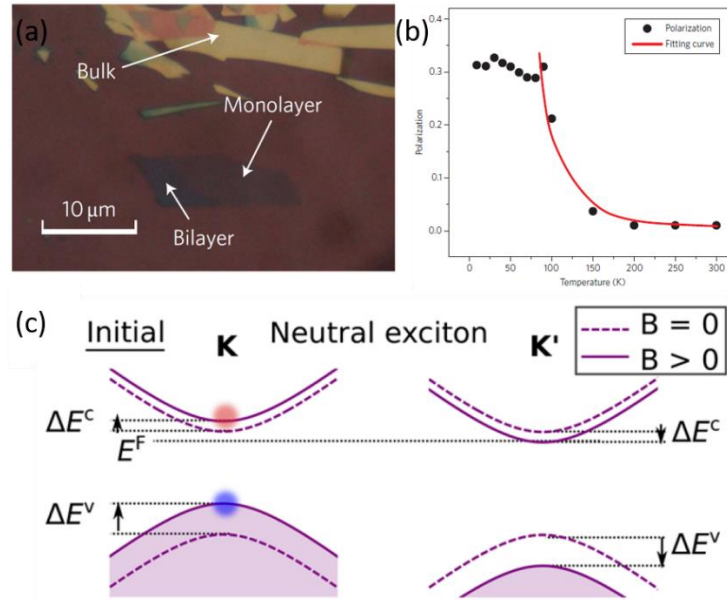


Figure 3: (a) Optical microscopy image of a MoS₂ monolayer flake, showing the unpredictability of exfoliated samples. (b) Temperature-dependent polarization degrees of monolayer MoS₂, showing a sharp decrease beyond cryogenic temperatures. (c) Band diagrams showing the breaking of degeneracy of the two valleys of monolayer MoS₂ via the valley Zeeman effect. ((a) and (b) adapted from [14]. (c) adapted from [19]).

Such disadvantages spurred us on towards finding a new material system that can phenomenologically provide us with the same or similar opportunities in accessing the valley degree of freedom. Specifically, we want to find a bulk system that has multiple sets of valleys governed by certain selection rules and can also be probed without using strong biases or cryogenic temperatures. This system should also, in theory, contain new physical origins that can create new opportunities for more fundamental studies.

Chapter Two¹

2. Demonstration of novel valleytronics in Tin(II) Sulfide (SnS)

2.1. Bulk Tin(II) Sulfide (SnS) as a valleytronics material

2.1.1. Transitioning from TMDCs – the search for a complementary valleytronics system

2.1.1.1. Black phosphorus (BP) as a representative two-dimensional (2D) anisotropic material

The natural progression of our search for a suitable valleytronic material began with some of the more well-known materials. As we ruled out graphene and TMDCs since they are already known 2D valleytronic material, the next potential material would be black phosphorus (BP). BP has gained much attention as 2D materials became more popular and the key attributes of BP make it a feasible starting point. BP has strong anisotropy along the two in-plane directions and thickness variations are known to be able to tune the direct band gap values over a large energy range [20]. Although BP does not possess multiple sets of band gap, we are inspired by the potential of having valleytronic materials with valleys selection rules determined by the anisotropy. Further, close inspection of BP's band structure reveals the presence of a local band gap along the ΓX axis, as shown in Figure 4 [20].

From our knowledge of TMDCs' band structures, we know that the valleys in TMDCs exist in bulk as local direct bandgaps with band gap energies much larger than that of the indirect bandgaps between the VB at Γ point and CB along ΓK [21]. As the wavefunctions that make up this indirect band gap are due to orbitals between the MX_2 layers, this indirect band gap widens with a decrease in number of layers and TMDCs eventually become direct band gap materials at the $\pm K$ points. Along the same line, we hypothesize that we can modify the interlayer interactions of BP to make the local band gap along ΓX (Figure 4) the global band gap, while at the same time leveraging on the anisotropy of the system.

¹ Reproduced in part with permission from [8].

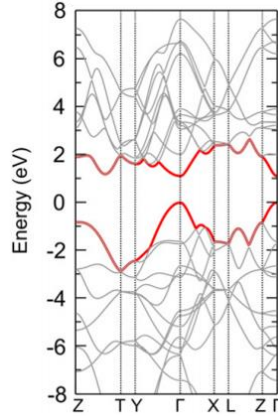


Figure 4: Calculated band structure of bulk BP, showing a direct band gap at Γ point, but also a local band gap along ΓX (adapted from [20]).

2.1.1.2. Monolayer IV-VI monochalcogenides as BP analogues

One way to achieve this change is to find another material system with the same symmetry and orbital compositions (and hence hybridization of orbitals) as BP, because slight changes in interlayer interactions may lead to the desired valley structure. From our knowledge of semiconductor compounds, we know that an obvious step is to move from Group V, where BP resides in, to IV-VI compounds (Figure 5a [22]). This is analogous to the relationship between III-V systems and Group IV systems. It turns out that IV-VI compounds indeed have the same crystal structure as their stable phase at room temperature when compared with BP (Figure 5b [23]). Note that the crystal structure of bulk IV-VI monochalcogenides in the orthorhombic phase is standardised to be $Pm\bar{c}n$ in this thesis, where the armchair and zigzag directions are defined to be y and x respectively. This follows the convention of labelling high symmetry k -points as previously reported in [24].

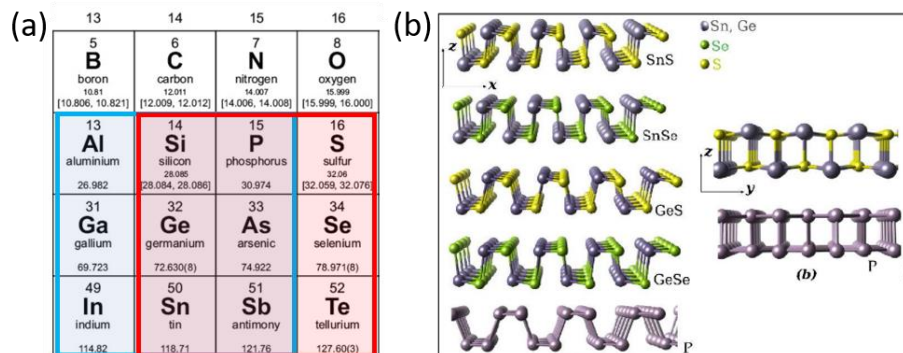


Figure 5: (a) A section of the periodic table of elements, showing that the relationship of IV-VI systems and Group V systems, highlighted in red, is analogous to that between III-V systems and Group IV systems, highlighted in blue. (b) Crystal structure of a single layer of BP and IV-VI monochalcogenides, showing the puckered structure. ((a) is adapted from [22], (b) is adapted from [23]).

2.1.1.3. Bandstructures of IV-VI monochalcogenides

Theoretical calculations of the bandstructures of bulk and monolayer IV-VI monochalcogenides are presented in Figure 6 [23]. We then identified possible valleytronics systems by the presence of two distinct local band gaps at different points in reciprocal space (\mathbf{k} points) and both band gaps must have smaller energy differences than other direct VB to CB transitions. The bandstructures show the presence of two non-degenerate band gaps along ΓX and ΓY for bulk and monolayer SnS and SnSe across all thicknesses (boxed in red), while materials systems boxed in black (lack of two band gaps) and blue (global band gap at Γ point) are deemed to be not suitable.

While the exact derivation of the selection rules will be presented in the next section, it is interesting to look at the key features of these bandstructures. Taking monolayer SnS as an example, we see that the band gaps reside along high symmetry lines (ΓX and ΓY) in \mathbf{k} space, as opposed to the high symmetry points (K^+ and K^-) of TMDCs [12]. This means that symmetry of wavefunctions at such band gaps will be lower than that at high symmetry points and will be different along ΓX and ΓY , making it highly possible for the local bandgaps to be valleys that obey certain selection rules.

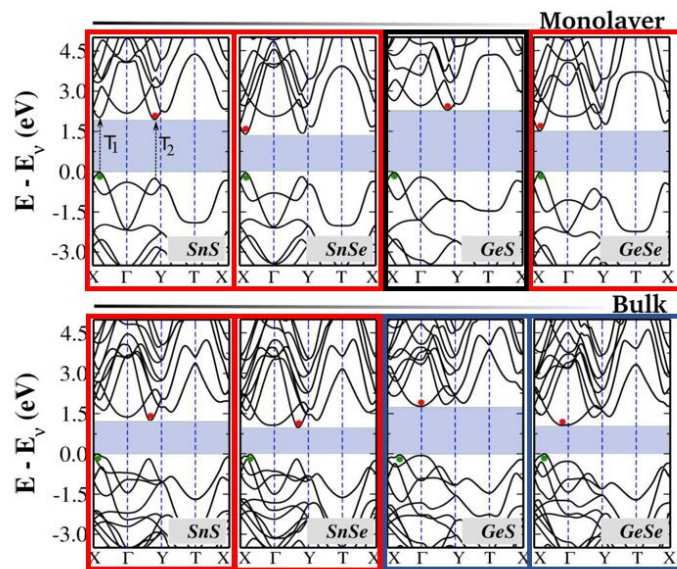


Figure 6: (c) Calculated band structure of bulk and monolayer IV-VI monochalcogenides. The red and green dots in each bandstructure refers to the global conduction band minimum (CBM) and valence band maximum (VBM). Potential valleytronics materials (with two distinct band gaps at different \mathbf{k} points) are boxed out in red, while other systems did not fulfil the requirement; blue boxes signify global band gap at the Γ point while black box signifies the lack of two band gaps. The bandstructure of SnS and SnSe show two local band gaps along ΓX and ΓY . Both band gaps have smaller energy difference than the local band gap at the Γ point (adapted from [23]).

2.1.2. Manifestation of valleytronics in SnS - Redefining the term “valley”

We can redefine a more general notion of valleys as two parts: (a) the presence of multiple groups of local bandgaps in the reciprocal space and (b) selection rules that allow separate control of each group of bandgaps. This definition plays into the strength of IV-VI systems; their band gaps are non-degenerate. The subtle, and yet immense, implication is that valleytronics systems no longer have to be confined to highly symmetric systems, where valley polarization is never inherent and can only be generated externally.

2.1.2.1. Selection rules in bulk SnS using Group Theory and symmetry

It turns out that the anisotropic nature of IV-VI systems stems from the unique orthorhombic crystal structure, which possesses lower symmetry than most cubic or hexagonal systems.

Figure 7 [8] shows the band structure of bulk SnS, comprising of two nearly direct transitions T_y and T_x , calculated based on density function theory (DFT). The calculations were performed using the Quantum ESPRESSO code [25]. The core electrons were treated using a Troulier–Martins pseudopotential [26]. The Kohn–Sham orbitals were expanded in a plane-wave basis with a cutoff energy of 50 Ry. The exchange and correlation interaction were described using the PBE functional [25]. Dipole matrix elements were calculated with the epsilon code, which is part of the Quantum ESPRESSO package [27].

The valley selection rules via optical means in bulk SnS can be derived as such [8]. We utilize the electric dipole approximation to determine the transition rate of an electron from the CB to VB at each valley and note that it is proportional to $|\hat{i} \cdot \langle i|r|f\rangle|^2$ where $|i, f\rangle$ denote the initial and final states, \hat{i} is the direction of the polarization of the electromagnetic wave, and r is the position operator. By invoking group theory arguments, we know that the direct product of the irreducible representations (IR) of $|i\rangle$, $|f\rangle$, and r must belong to the totally symmetric representation A1 for the integral and hence the transition rate to be non-zero.

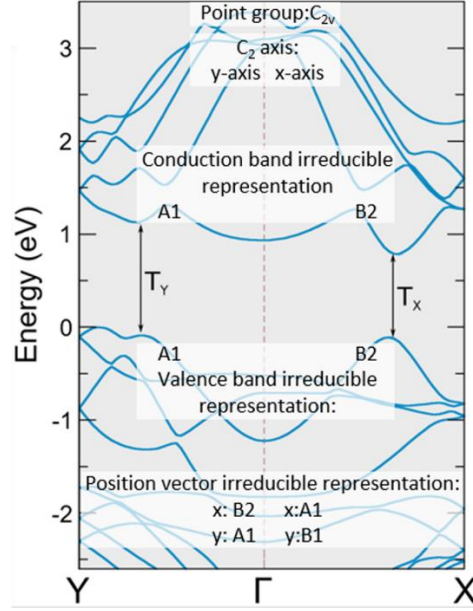


Figure 7: Bandstructure of bulk SnS. The directions y and x are the armchair and zigzag directions, respectively. The respective irreducible representations of the conduction band, valence band, and position vectors, as well as the point group and two-fold rotation axis, are indicated for each direction (adapted from [8]).

We consider the valleys along ΓX and ΓY separately.

For the \mathbf{k} points along ΓX (excluding the Γ and X points), the symmetries of the CB and VB can be fully described by the C_{2v} point group [28], with the 2-fold rotation symmetry axis C_2 along the x axis. We note that for the CB and VB, respectively, every \mathbf{k} point along the high symmetry ΓX line contains the same symmetry and hence the selection rules apply to any CB-VB transition within ΓX . The IRs of the CB, x position vector, and VB are determined to be B_2 , A_1 , and B_2 respectively, meaning $\langle i|\mathbf{x}|f\rangle$ transforms as $B_2 \otimes A_1 \otimes B_2 = A_1$ and the transition is allowed. The IR of the y position vector is B_1 , thus $\langle i|\mathbf{y}|f\rangle$ transforms as $B_2 \otimes B_1 \otimes B_2 = B_1$ and the transition is not allowed. This means that transitions between the CB and VB along ΓX can only occur with x -polarized light.

Following the same argument, for the \mathbf{k} points along ΓY (excluding the Γ and Y points), $\langle i|\mathbf{r}|f\rangle$ transforms as $A_1 \otimes B_2 \otimes A_1 = B_2$ for light polarized along x and thus the transition is not allowed while $\langle i|\mathbf{r}|f\rangle$ transforms as $A_1 \otimes A_1 \otimes A_1 = A_1$ for light polarized along y and thus the transition is allowed. We see that transitions between the CB and VB along ΓY can only occur with x -polarized light.

The character tables for both ΓX and ΓY are presented in Table 1 [8].

Table 1: Character table for C_{2v} point group for \mathbf{k} points along ΓX (top) and ΓY (bottom) (adapted from [8]).

C_{2v} (ΓX)	E	$C_2(x)$	$\sigma_v(xy)$	$\sigma_v(xz)$	Position vectors	Bands
A1	+1	+1	+1	+1	x	CB, VB
A2	+1	+1	-1	-1		
B1	+1	-1	+1	-1	y	
B2	+1	-1	-1	+1	z	

C_{2v} (ΓY)	E	$C_2(y)$	$\sigma_v(yz)$	$\sigma_v(xy)$	Position vectors	Bands
A1	+1	+1	+1	+1	y	CB, VB
A2	+1	+1	-1	-1		
B1	+1	-1	+1	-1	z	
B2	+1	-1	-1	+1	x	

2.1.2.2. Detour: Application of selection rules in monolayer SnS

We note that there is also a theoretical work on the valley selection rules of monolayer SnS [29]. In that work, a similar approach by group theory was carried out. However, because the theoretical valley selectivity is not exact, the authors utilized $\mathbf{k}\cdot\mathbf{p}$ approximation to calculate the matrix elements of the transition moment integral $\langle i|\mathbf{r}|f\rangle$. For monolayer SnS, while the ΓY valley is totally selective to y -polarized light, x - and y -polarized light have a 40:1 ratio in exciting the ΓX valley.

2.1.2.3. Detour: Application of selection rules in TMDCs – alternative way of understanding TMDCs valleytronics

In Chapter 1, we discussed about the origin of valleytronics in TMDCs via Berry curvature arguments. At this juncture, it is interesting to look at valleytronics in TMDCs via group theory arguments. TMDC monolayers have a C_{3h} space group, presented in Table 2 [30].

Table 2: Character table of C_{3h} space group (adapted from [30]).

C_{3h}	E	$\varepsilon = \exp(2\pi i/3)$					linear functions, rotations	quadratic functions	cubic functions
		$C_3(z)$	$(C_3)^2$	σ_h	S_3	$(S_3)^5$			
A'	+1	+1	+1	+1	+1	+1	R_z	x^2+y^2, z^2	$y(3x^2-y^2), x(x^2-3y^2)$
E'	+1	$+\varepsilon$	$+\varepsilon^*$	+1	$+\varepsilon$	$+\varepsilon^*$	$x+iy$	(x^2-y^2, xy)	$(xz^2, yz^2) [x(x^2+y^2), y(x^2+y^2)]$
	+1	$+\varepsilon^*$	$+\varepsilon$	+1	$+\varepsilon^*$	$+\varepsilon$	$x-iy$		
A''	+1	+1	+1	-1	-1	-1	z	-	$z^3, z(x^2+y^2)$
E''	+1	$+\varepsilon$	$+\varepsilon^*$	-1	$-\varepsilon$	$-\varepsilon^*$	R_x+iR_y	(xz, yz)	$[xyz, z(x^2-y^2)]$
	+1	$+\varepsilon^*$	$+\varepsilon$	-1	$-\varepsilon^*$	$-\varepsilon$	R_x-iR_y		

However, because the CB and VB of TMDCs undergo spin-splitting, spin up and spin down electrons essentially reside at different subbands in the CB and VB. This means that we have

to include additional inversion symmetry and their multiplication for all symmetry operations; the spinor representation (Table 3 [31]) of the space group has to be used. Table 3 is essentially a duplicate of Table 2, where each IR is now divided into spin up and down.

Table 3: Spinor representation of character table of C_{3h} space group (adapted from [31]).

C_6	E	\bar{E}	C_6	\bar{C}_6	C_3	\bar{C}_3	C_2	\bar{C}_2	C_3^{-1}	\bar{C}_3^{-1}	C_6^{-1}	\bar{C}_6^{-1}	Time	Bases	Bases
C_{3h}	E	\bar{E}	S_3^{-1}	\bar{S}_3^{-1}	C_3	\bar{C}_3	σ_h	$\bar{\sigma}_h$	C_3^{-1}	\bar{C}_3^{-1}	S_3	\bar{S}_3	Inv.	for C_6	for C_{3h}
Γ_1	1	1	1	1	1	1	1	1	1	1	1	1	a	R or z or S_x	R
Γ_2	1	1	$-\omega^2$	$-\omega^2$	ω^4	ω^4	1	1	$-\omega^2$	$-\omega^2$	ω^4	ω^4	b	$(x - iy)^2$	$(x - iy)^2$
Γ_3	1	1	ω^4	ω^4	$-\omega^2$	$-\omega^2$	1	1	ω^4	ω^4	$-\omega^2$	$-\omega^2$	b	$(x + iy)^2$	$(x + iy)^2$
Γ_4	1	1	-1	-1	1	1	-1	-1	1	1	-1	-1	a	$(x \pm iy)^3$	z
Γ_5	1	1	ω^2	ω^2	ω^4	ω^4	-1	-1	$-\omega^2$	$-\omega^2$	$-\omega^4$	$-\omega^4$	b	$-(S_x + iS_y)$	$-(S_x + iS_y)$
Γ_6	1	1	$-\omega^4$	$-\omega^4$	$-\omega^2$	$-\omega^2$	-1	-1	ω^4	ω^4	ω^2	ω^2	b	$(S_x - iS_y)$	$(S_x - iS_y)$
Γ_7	1	-1	ω	$-\omega$	ω^2	$-\omega^2$	i	-i	$-\omega^4$	ω^4	$-\omega^5$	ω^5	b	$\phi(1/2, 1/2)$	$\phi(1/2, 1/2)$
Γ_8	1	-1	$-\omega^5$	ω^5	$-\omega^4$	ω^4	-i	i	ω^2	$-\omega^2$	ω	$-\omega$	b	$\phi(1/2, -1/2)$	$\phi(1/2, -1/2)$
Γ_9	1	-1	$-\omega$	ω	ω^2	$-\omega^2$	-i	i	$-\omega^4$	ω^4	ω^5	$-\omega^5$	b	$\phi(5/2, -5/2)$	$\phi(5/2, -5/2)$
Γ_{10}	1	-1	ω^5	$-\omega^5$	$-\omega^4$	ω^4	i	-i	ω^2	$-\omega^2$	$-\omega$	ω	b	$\phi(5/2, 5/2)$	$\phi(5/2, 5/2)$
Γ_{11}	1	-1	-i	i	-1	1	i	-i	-1	1	i	-i	b	$\phi(3/2, -3/2)$	$\phi(3/2, -3/2)$
Γ_{12}	1	-1	i	-i	-1	1	-i	i	-1	1	-i	i	b	$\phi(3/2, 3/2)$	$\phi(3/2, 3/2)$

$\omega = \exp(\pi i/6)$

From the character tables, we can see that our symmetry-based selection rules are fully applicable to TMDCs. Taking monolayer WSe₂ as an example (Figure 8 [32]), the IRs for the VB_{-K} , VB_{+K} , CB_{-K} , and CB_{+K} are A' , A' , E' , and E' respectively. These translate into Γ_1 , Γ_1 , Γ_2 , and Γ_3 in spinor representation. Because a spin up (spin down) electron possesses an IR of Γ_7 (Γ_8), after spin splitting, the IRs at $VB_{-K(\uparrow)}$, $VB_{+K(\downarrow)}$, $CB_{-K(\uparrow)}$, and $CB_{+K(\downarrow)}$ respectively becomes $\Gamma_1 \times \Gamma_7 = \Gamma_7$, $\Gamma_1 \times \Gamma_8 = \Gamma_8$, $\Gamma_3 \times \Gamma_7 = \Gamma_{10}$, and $\Gamma_2 \times \Gamma_8 = \Gamma_9$. For the transformation of $\langle i|\mathbf{r}|f \rangle$ to be that of A_1 or Γ_1 , the respective IRs for \mathbf{r} at $-K$ and $+K$ must be Γ_3 (transforms as $x-iy$) and Γ_2 (transforms as $x+iy$), which happens to be that of σ^- and σ^+ polarizations. From Figure 8, we can see that while x (in-plane) polarized light can excited electrons from both VBM to the next spin-conserved state, each valley is only excited by either left or right circularly polarization.

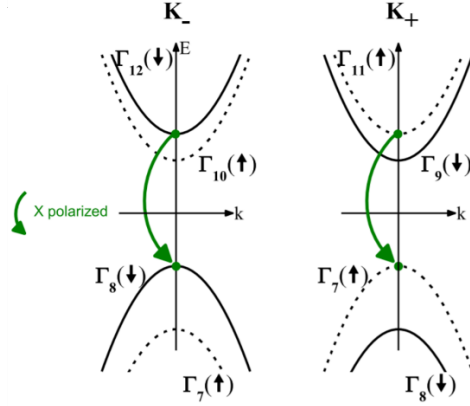


Figure 8: Schematic band diagram of monolayer WSe₂, showing the effect of spin splitting on the spinor IRs and the eventual valley selection rules at $-K$ and $+K$. The green arrow shows that the x (in-plane) polarized light, with IR of E' , is able to excite both valleys. However, only components of E' with IR of Γ_2 (Γ_3) is able to cause excitation at $-K$ and $+K$ respectively. This forms the basis of valley selectivity by circularly polarized light (adapted from [32]).

The important takeaway from the success of using the electric dipole approximation and transition moment integral to determine valley selection rules for both TMDCs and IV-VI systems is that such a formalism based on symmetry is highly robust and possibly widely applicable to many systems.

2.2. Synthesis of bulk SnS plates

2.2.1. Experimental setup and procedures

Bulk SnS plates were prepared on fused silica substrate (for R and T measurements) and on Si/SiO₂ substrates (for PL measurements). Plates can be either mechanically exfoliated or synthesized, with the exfoliated pieces generally thinner and smaller in lateral size. The initial phase of the project was thus focused on fine tuning the parameters of physical vapor deposition (PVD) or chemical vapor deposition (CVD), with the aim of obtaining large pieces suitable for optical measurements. The methods are adopted from [33] and [34] respectively.

The experimental setups are shown in Figure 9. In the nominal PVD method (Figure 9a), SnS powder (~100mg) is placed in the middle of a tube furnace. The nominal CVD method (Figure 9b) utilizes SnO (~15mg) and S (~350mg) powder as sources, placed in the middle of a tube furnace and 13cm upstream respectively. In both methods, substrates are placed 6cm to 15cm downstream. Argon (Ar) is used as a carrier gas and pumped in at 100sccm at an equilibrium pressure of 10-760Torr. The tube is heated until 500-800°C at 20°C/min, held at that temperature for 10-60min and then air cooled.

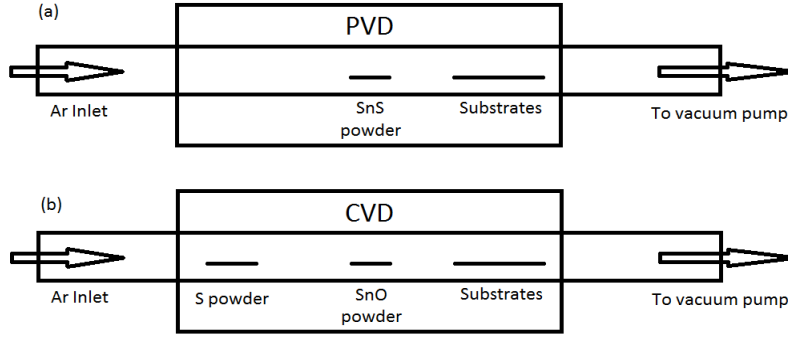


Figure 9: Schematics of experimental setups for (a) PVD and (b) CVD growths of bulk SnS plates respectively.

2.2.2. Trends in varying parameters for SnS synthesis

The main implication of tuning parameters for SnS synthesis in both PVD and CVD methods is the alteration of the synergistic effect between source temperature (T_s), substrate temperature (T_{sub}), and pressure (P). While it is difficult to quantitatively calculate an optimal condition due to the complex gas flow in the tube furnace, trends in growth by vapor deposition can be adequately predicted by considering fundamental P-T relationship [35].

T_s increases the evaporation rate of the source and by increasing the equilibrium vapor pressure (P_v^*) of the source. A higher T_s also causes an increase in T_{sub} at the same source-substrate distance. Both T_s and T_{sub} are important because two other sulfides of tin, namely Tin(III) Sulfide (Sn_2S_3) and Tin(IV) Sulfide (SnS_2) are frequently present as impurities in SnS [36]. P_v^* of these three phases increase in the order $SnS < Sn_2S_3 < SnS_2$ [37]. Using information from [37], we can plot the graphs of P_v^* against T , as shown in Figure 10. We see that if we overlay a cooling sequence of T_{sub} (dotted arrow) under a reasonable P , the order of saturation (when P exceeds P_v^* at the particular T_{sub}) and hence deposition/ condensation follows SnS to Sn_2S_3 to SnS_2 as the gas flows downstream or to lower T_{sub} . Along the same line, the order of evaporation for PVD as T_s increases follows the reverse order of SnS_2 to Sn_2S_3 to SnS. This means that when SnS_2 or Sn_2S_3 is observed, either T_s or T_{sub} must be increased.

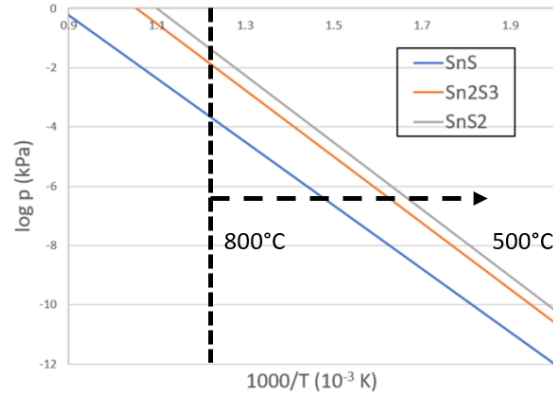


Figure 10: $\log(P_v^*)$ against $1/T$ graph of SnS, Sn₂S₃, SnS₂. Dotted overlaid arrow signifies the cooling down of the gas as it moves downstream at a gas pressure within the range of our study, showing that the sequence of supersaturation follows SnS to Sn₂S₃ to SnS₂.

Via the above-mentioned parametric study, we observed that the PVD method yields large SnS pieces (up to 50µm in width) while the CVD method allows more versatility in sample composition and morphology. Both methods also follow the general trend of increasing plate size and thickness while maintaining similar aspect ratio with increasing source pressure and Ar pressure.

2.2.3. Physical Vapor Deposition (PVD)

Table 4 shows the list of parameters varied for PVD. The optimized parameters are then determined to have substrates are placed 9cm downstream, with Ar pumped in at 30sccm at an equilibrium pressure of 760Torr, and the tube heated until 700°C and held for 10min before being air cooled.


Table 4: List of parameters varied for PVD.

		Temp [C]		500		600		650		700		750		800	
		Time (min)		10	30	10	30	10	30	30	30	30	10		
Pressure (Torr)	Flow rate (sccm)														
		10	30												
20	200														
	60														
80	60														
	60														
200	30														
	60														
760	60														
	100														
	100														
	200														

2.2.4. Chemical Vapor Deposition (CVD)

Table 5 shows the list of parameters varied for PVD. The optimized parameters are then determined to have substrates are placed 9cm downstream, with Ar pumped in at 30sccm at an equilibrium pressure of 760Torr, and the tube heated until 700°C and held for 10min before being air cooled.

Table 5: List of parameters varied for CVD [38].



Temp [C]	500			550		600			650		705	
Time (min)	30	40	60	30	40	30	40	60	30	40	20	40
Distance (cm)	6											
	7											
	8											
	9											
	10											
	11											
	12											
	13											
	14											
	15											

2.3. Accessing valley degree of freedom via optical means

2.3.1. Experimental setup and procedures

As mentioned, in our description of SnS's crystal structure, we use the Pmcn space group, which denotes, by convention [39], the x , y , and z axes to be the zigzag, armchair, and out-of-plane directions respectively. According to this convention, the x (y) axis also coincides with the ΓX (ΓY) axis in reciprocal space. This ensures clarity when applying the selection rules.

Verification of the selection rules was performed via optical means. Figure 11 [8] shows the reflection mode optical setup configuration used for Raman, PL, and R measurements, where the sample is rotated with respect to the polarization axis of the linearly polarized excitation light, giving an angle θ . ($\theta = 0^\circ$ is set by default to the armchair (y) direction via analysis of Raman results; the procedure of which documented in the next section.) T measurements were conducted with the detection light path on the back side of the sample.

Linearly polarized incident light is shone with normal incidence on the sample, and the resulting signal is detected in the reflection mode. Excitation was conducted using laser (for Raman and PL) and white light (for R and T) on a sample that can be rotated to give an angle θ between the polarization axis and the armchair direction. A second polarizer was also placed either parallel or perpendicular to the excitation polarization for Raman and PL measurements. Polar plots of signal intensity against θ were then constructed.

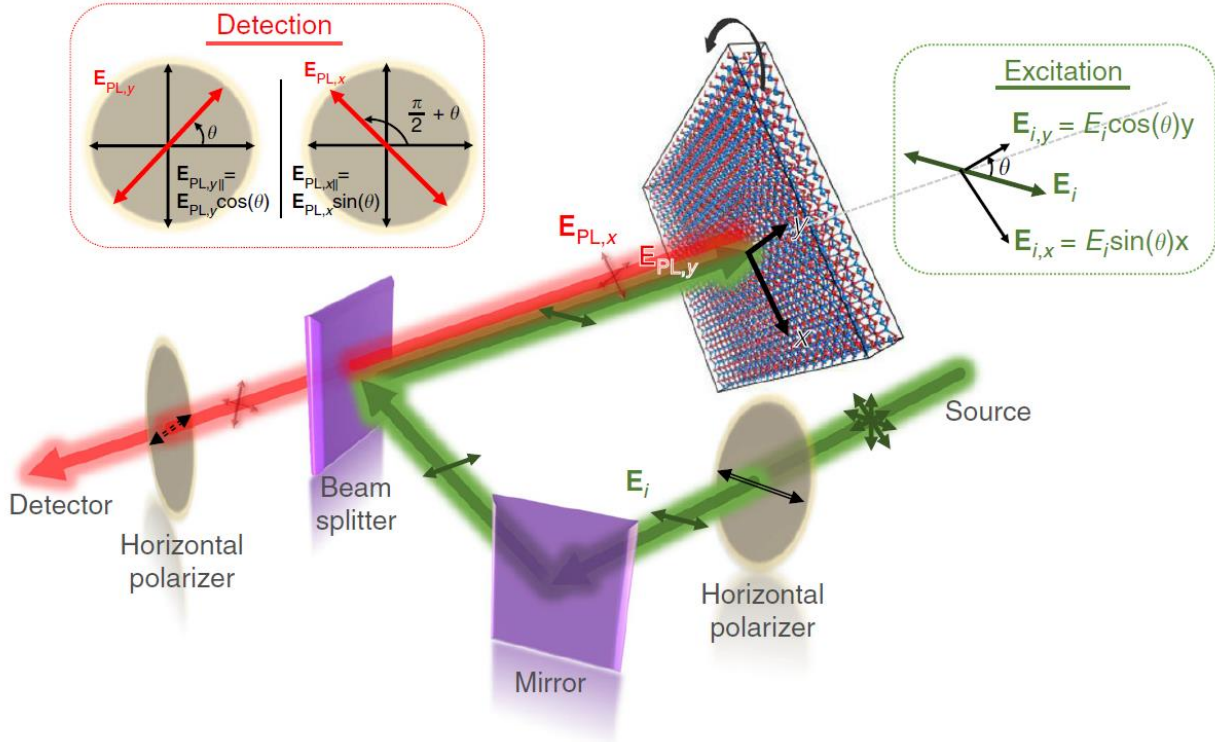


Figure 11: Schematic of the experimental setup for Raman, PL, and reflection (R) measurements. Transmission (T) measurements were conducted with the detection light path on the back side of the sample. Excitation was conducted using linearly polarized laser (for Raman and PL) and white light (for R and T) on a sample that can be rotated to give an angle θ between the polarization axis and the armchair direction. A second polarizer was also placed either parallel or perpendicular to the excitation polarization for Raman and PL measurements (adapted from [8]).

2.3.2. Identification of main crystal axes

2.3.2.1. Identifying facets of grown SnS plates via surface energy arguments

Figure 12a [8] shows a representative piece of SnS grown using the PVD method. Scanning electron microscopy (SEM) images and energy-dispersive X-ray spectroscopy (EDX) maps show a homogeneous distribution of Sn and S in a bulk SnS plate without any macroscopic defects. Note that subsequent optical results are also reproducible using CVD or exfoliated samples.

Before conducting linearly polarized optical measurements, it is important to identify the main axes of the sample. In grown samples, this can be done by direct observation of the angles made by each corner. Using surface energy (ϵ) arguments, we know that for SnS, ϵ , and hence growth rate, follows the trend (100) and $(010) > (200) > (1-10) > (110)$, which means that the preferred lateral faces go in the order $(110) > (1-10) > (200) > (100)$ and (010) . Gibbs-Curie-Wulff law states that the normal growth rates of crystal faces are proportional to the corresponding surface free energies. Using a Wulff plot as shown in Figure 12b [40], we get the equilibrium shape of the SnS crystal to be a parallelogram with

the two sides being (110) and (1-10). Since the lattice parameters along the armchair (y) and zigzag (x) directions are 4.32Å and 3.98Å respectively, the bisectors of 85° and 95° in the crystal are the y and x directions respectively.

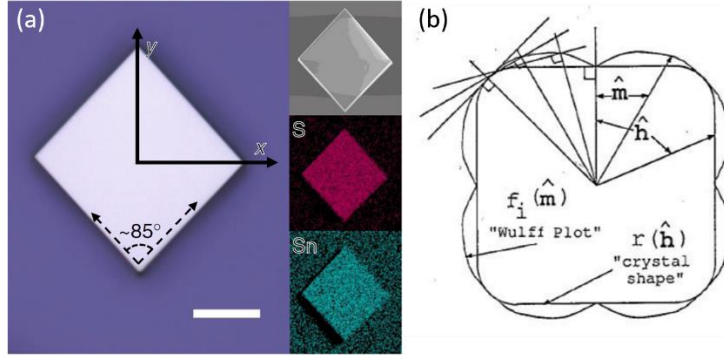


Figure 12: (a) Optical microscopy image of a SnS sample, showing a clear difference in angles made by the edges and ease of identifying the in-plane directions. Scale bar is 10 μm . Inset shows scanning electron microscopy (SEM) images and energy-dispersive X-ray spectroscopy (EDX) maps, demonstrating a flat surface and homogeneous distribution of Sn and S in equal ratio. (b) Illustration of a Wulff plot, where perpendicular lines are drawn at a distance proportional to the surface energy of the plane normal to each lattice direction. The shape of a grown crystal is the shape of the smaller area or volume enclosed by these lines. ((a) is adapted from [9], (b) is adapted from [40]).

2.3.2.2. Raman measurements

The Raman spectra of crystalline bulk SnS plates consists of multiple peaks, which upon deconvolution yield important information about the angular dependence of the Raman modes. From previous work, Raman tensors of the four observable Raman modes, which reside at 95.5 cm^{-1} , 190.7 cm^{-1} , and 216.8 cm^{-1} for A_g and 162.5 cm^{-1} for B_{3g} , have been shown to have only two (one) non-zero components that contributes to the polarization dependent Raman under excitation in the -z (normal to plate surface) direction for the A_g (B_{3g}) mode [34] [41]. The equations provided in [34] are:

$$I_{A_{g,\parallel}} = B \cos^2(\theta) + C \sin^2(\theta) \quad (1)$$

$$I_{A_{g,\perp}} = \frac{(C - B)^2}{4} \sin^2(2\theta) \quad (2)$$

$$I_{B_{3g,\parallel}} = F^2 \sin^2(2\theta) \quad (3)$$

$$I_{B_{3g,\perp}} = F^2 \cos^2(2\theta) \quad (4)$$

In order to rigorously determine the main axes directions of our samples, we utilized the listed equations to determine the sample orientation and fixed $\theta=0^\circ$ to the armchair (y direction). The B_{3g} peak was fitted first because of simplicity in handling the fitting constant,

F. We define a phase offset ω to account for the initial sample orientation not being at $\theta=0^\circ$ but at $\theta=\omega$. The average ω value for $B_{3g,\parallel}$ and $B_{3g,\perp}$ was then used to offset all subsequent θ values presented to ensure consistency in our analysis.

Figure 13a [9] shows the typical Raman spectra of SnS plates under parallel polarization, showing that all four Raman peaks are distinguishable even without deconvolution, have a small FWHM of 1nm and position approximately that of the established Raman modes. We fitted the three remaining peaks to the said A_g Raman modes and present all polar plots in Figure 13b [41]. The trend of the A_g modes fits well with the listed equations, ascertaining the identity of the plates to be SnS.

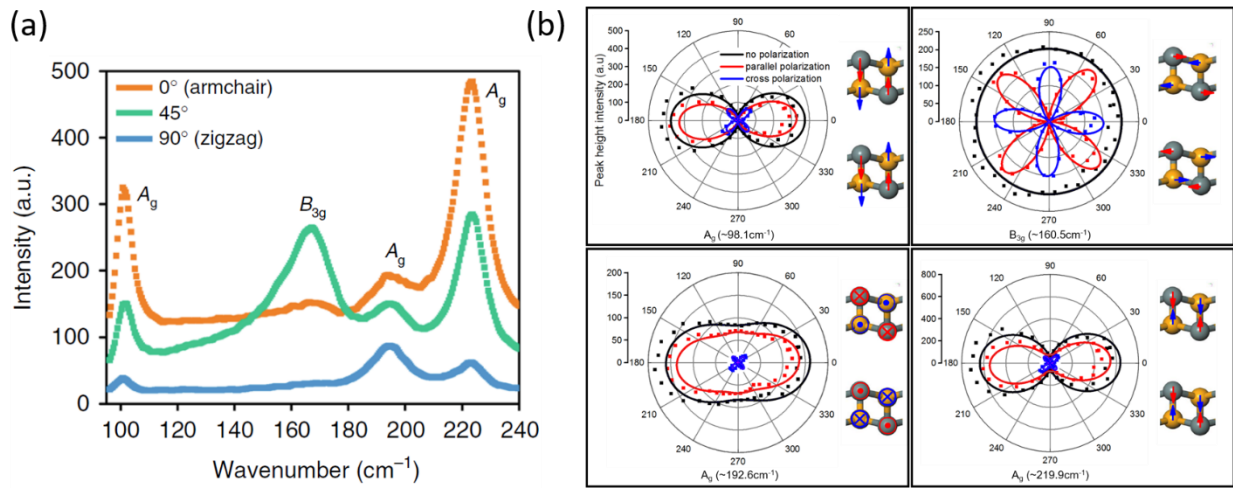


Figure 13: (a) An example of Raman spectra obtained under parallel polarization, showing clear trends in intensities for the A_g and B_{3g} modes, thus ascertaining the identity and orientation of the measured SnS sample (adapted from [9]). (b) Four polar plots of peak height intensity variations in Raman peaks assigned to either A_g or B_{3g} modes. The intensity variations follow the trend in published results and allowed us to have a rigorous derivation of the material axes directions (vibration modes adapted from [41]).

2.3.3. White light reflection (R) and transmission (T) measurements

Linearly polarized broadband white light was illuminated on the SnS samples on fused silica substrates and the R and T signals were obtained without a second polarizer. We conducted the experiment without a second polarizer because we are only interested in observing the selectivity of the valleys for the absorption of polarized light across the visible-near IR range. We used the reflection spectrum of a clean gold substrate (T spectrum of a clean fused SiO_2 substrate) to normalize the R (T) spectra by considering the theoretical R (T) of gold (fused SiO_2) obtained from reported literature values [42] [43]. We observed clear valley selectivity, as shown in Figure 14 [8].

R and T of our sample remains stable at short wavelengths until the onset of fluctuations due to Fabry-Pérot interference oscillations [44], which denotes the region where the

absorption of SnS decreases rapidly. This agrees with the observation that the percentage of transmitted light is very small at wavelengths shorter than the oscillations. Distinct onsets are observed when the polarization of light is aligned to the armchair (zigzag) directions, respectively.

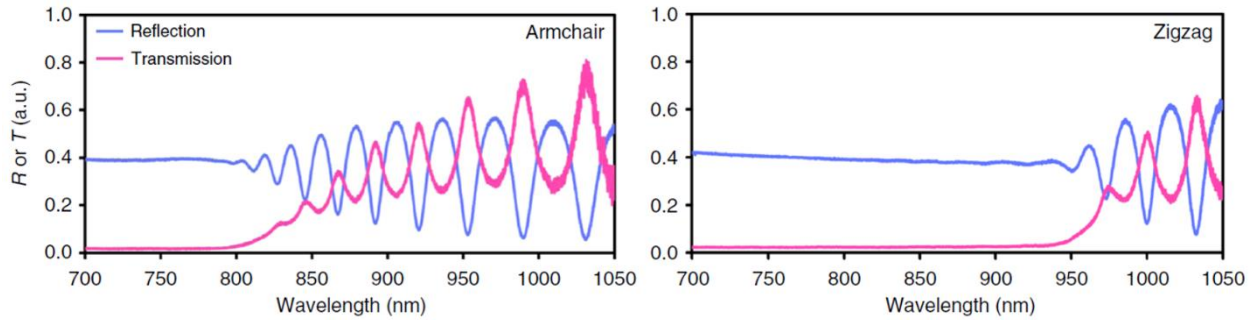


Figure 14: Reflection and transmission measurements of SnS. White light with wavelengths ranging from 700 to 1050 nm illuminated the sample without a second polarizer (adapted from [8]).

R measurements were also conducted on samples that were grown on Si/SiO₂ substrates, as shown in Figure 15, to eliminate the possibility of light transmitting through the substrate after passing through the samples. This ensures that the generation of such Fabry-Pérot modes is mostly governed by the samples' optical response.

Figure 15 shows that under the orientation where the armchair direction is aligned to the axis of polarization, the Fabry-Pérot modes begin to appear at wavelengths longer than 775nm. More accurately, this signifies that the material starts to absorb light at wavelengths shorter 775nm and hence the Fabry-Pérot modes cease to occur because the reflection intensity is solely based on the reflection off the surface of the material, which remains relatively constant barring some slight dispersion-induced effects. This selective absorption is attributed to the Γ Y valley.

Increasing the angle between the polarization and material symmetry axes, we see that these Fabry-Pérot modes are dampened but the peak positions between 775nm and 950nm do not shift. This agrees with our understanding that light with wavelength longer than 775nm are now attenuated because the portion of light with E-field parallel to the zigzag direction can now be absorbed at the Γ X valley, and hence there is a seemingly attenuated amount of light available for Fabry-Pérot oscillations.

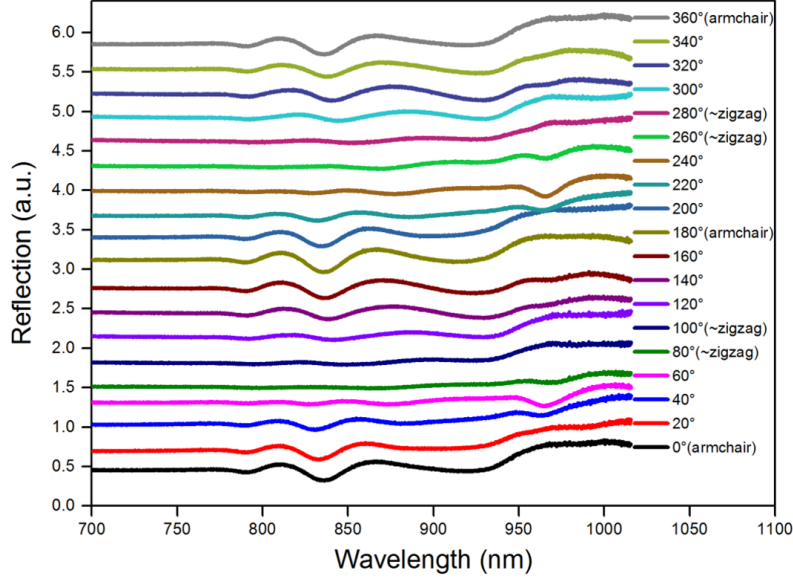


Figure 15: Reflection spectra of SnS grown on Si/SiO₂ substrates with sample rotated every 20° for a full θ rotation. Results clearly show that the onset of Fabry-Pérot oscillations for most θ values is at 775nm. When the polarization is aligned exactly to the zigzag direction, the oscillations are fully dampened (presumably because absorption at 775nm is no longer allowed) and another onset of Fabry-Pérot oscillations is shown to be 950nm.

2.3.3.1. Determining absorption coefficient and degree of optical dichroic anisotropy from R and T of samples on substrates

Absorption coefficients, α , were obtained from the normalized R and T data via $\alpha = -\frac{1}{d} \ln\left(\frac{T}{1-R}\right)$ [45] [46] and plotted, disregarding the thickness, d, in a self-consistent manner without a loss of generality. It is important to note the effectiveness of using the equation listed above for the determining of α without any information on the value of d, which is especially crucial in our work because our grown samples often have thicknesses that exceeds the limit of atomic force microscopes (AFM), which is generally more than 3 μ m. Our method, derived in detail in and adapted from [46], follows the following logic:

The wavelength-dependent absorption coefficient of SnS is given by $\alpha_{\text{SnS}} = \frac{4\pi k_{\text{SnS}}}{\lambda}$, where $N_{\text{SnS}} = n_{\text{SnS}}(\lambda) - ik_{\text{SnS}}(\lambda)$ is the complex refractive index of SnS. With a configuration of measurement being Air|Sample|Quartz|Air, and knowing $N_{\text{air}} = 1$ and $N_{\text{quartz}} = n_{\text{quartz}}(\lambda)$ [42] both only contain the real part to the refractive index, $n_{\text{SnS}}(\lambda)$ and $k_{\text{SnS}}(\lambda)$ can be solved by knowing that at every interface $R = \frac{|N_2 - N_1|^2}{|N_2 + N_1|^2}$ and within SnS, $1 - A = \frac{1}{I_0} = e^{-\alpha_{\text{SnS}}d}$. Taking the experimental data of R and T, both functions of only $n_{\text{SnS}}(\lambda)$ and $k_{\text{SnS}}(\lambda)$, α_{SnS} can be obtained via iteration. However, such a method not only requires accurate d values, but often results in artefacts carried over due to experimental errors. Mathematical derivations in [46] has shown that $\frac{T}{1-R}$ should have minimal “wavy” interference features, which can be used as a

quick check for data validity. It is also a very accurate approximation such that the value of d can be ignored.

Band-gap values were then obtained by determining the x-intercept of the corresponding direct Tauc plots [47], plotted as $(\alpha h\nu)^2$ against $h\nu$ in the left axis of Figure 16, where $E = h\nu$ is the incident photon energy. The Tauc plots give band-gap values of 1.48 eV and 1.28 eV, clearly distinguishing the two sets of valleys.

The selectivity of the absorption to polarized light can be quantified by the degree of optical dichroic anisotropy, which is given by the ratio $\alpha_{\text{zigzag}}/\alpha_{\text{armchair}}$ in our system (right axis of Figure 16). We see that SnS is able to maintain a $\alpha_{\text{zigzag}}/\alpha_{\text{armchair}} > 200\%$ for a range of more than 0.2 eV and also possesses a maximum $\alpha_{\text{zigzag}}/\alpha_{\text{armchair}} > 600\%$. This wide range and large anisotropy may potentially relax the strict requirements usually present in valleytronic systems.

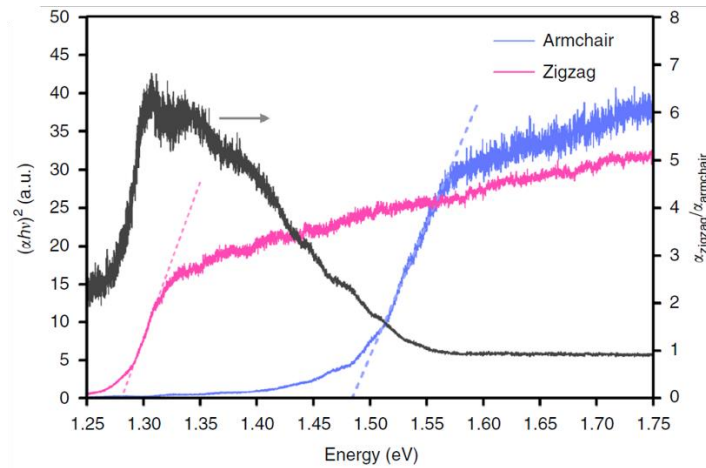


Figure 16: (Left axis) Tauc plots of both directions, with fitting lines denoting band gaps at 1.28 and 1.48 eV for zigzag and armchair directions, respectively. (Right axis) Degree of optical dichroic anisotropy, $\alpha_{\text{zigzag}}/\alpha_{\text{armchair}}$. (adapted from [8]).

2.3.3.2. Variations of band gaps with temperature

Because the valley behavior in SnS is due to polarization-dependent band-gap transitions, we further investigated the temperature dependence of the absorption coefficients along the two axes directions. From the plots of α (Figure 17a [8]), we see that the x-axis intercept increases with decreasing temperatures, which agrees with the typical behavior of band gaps. The variations in band-gap values with temperature are then fitted with the Varshni equation [48] (Figure 17b [8]), which shows that the valley behavior extends across the whole investigated temperature range.

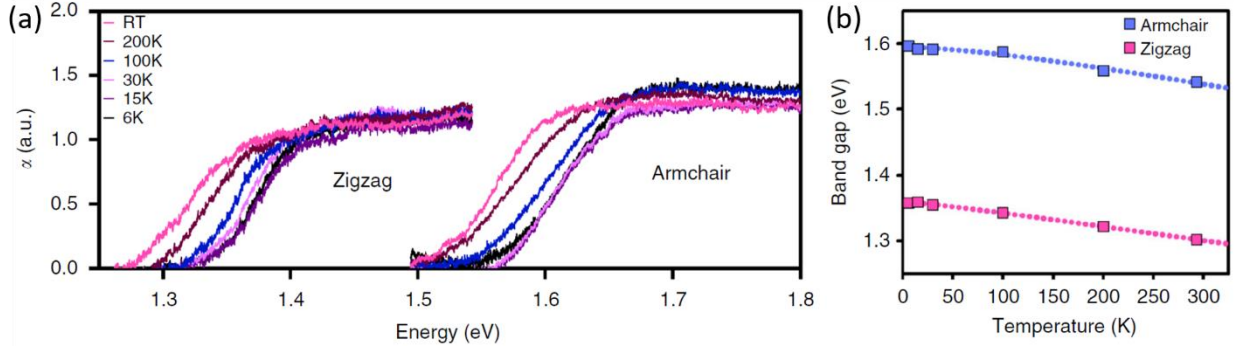


Figure 17: (a) Absorption coefficients of both directions under different temperatures, showing a distinct increase in band gap with decreasing temperature. (b) Vashni plot extracted from the temperature varying absorption measurements. ((a) and (b) adapted from [8]).

2.3.3.3. Estimating sample thickness from R and T of samples on substrates

While knowledge on sample thicknesses (d) are often less critical for measurements of material properties in the bulk regime, it may sometimes be useful to have an effective method to quickly estimate a sample's thickness. We can conduct such an exercise by understanding the origin of the interference peaks and hence the relationship between the peak position (λ), d , and the refractive index (n).

The interference pattern occurs because in the wavelength range where the sample has minimal absorption, light undergoes multiple reflections within the sample. At specific wavelengths, the reflected light will be completely out of phase (and alternating in phase) with the incident light, leading to destructive (constructive) interference and a large dip (peak) in reflection. The condition for destructive (constructive) interference under normal incidence is given as $2n_{SnS}d = m\lambda$, where m is the order of the reflection peak. For adjacent peaks, $2n_1d = m\lambda_1$ for $n_1 = n_{SnS}(\lambda_1)$ and $2n_2d = (m+1)\lambda_2$ for $n_2 = n_{SnS}(\lambda_2)$, giving $d = \frac{\lambda_1\lambda_2}{2(\lambda_1n_2 - \lambda_2n_1)}$ or $d = \frac{\lambda_1\lambda_2}{2n(\lambda_1 - \lambda_2)}$ if we assume a wavelength-independent n . Note that a more sophisticated method of fitting the R and T interference profiles can be found in [49].

There are multiple methods to determine n [50]. In our estimation, we utilized a common method developed by Moss [50], which assumes typical semiconductor behaviour where absorption of photons leads to the raising of an electron to an excited state. The electron thus behaves as a hydrogen atom's electron but with the bulk material's effective dielectric constant. Following Bohr's model, $E \propto \frac{1}{\epsilon^2} \propto \frac{1}{n^4}$. Empirically, semiconductors have been known to follow $E_g n^4 = 95 eV$ [51], giving $n \approx 3$ for SnS. Taking λ values from Figure 14, we obtain $d \approx 6 \mu m$.

2.3.4. Photoluminescence (PL) measurements

For PL measurements, a polarizer was placed before the detector parallel to the excitation polarization and the sample was rotated to give different θ values (shown in Figure 11). Parallel polarization allows us to demonstrate selectivity for emission. Similar emission peaks were observed with excitation using linearly polarized lasers at 532, 633, and 785 nm, giving, which confirms the PL nature of the peaks.

We observed two PL peaks at 760nm (with a higher energy shoulder at 817nm) and 995 nm (Figure 18a). The polarization dependence of both PL peaks is clearly observed. The 817 nm peak maximizes at the polarization that minimizes the 995 nm peak, and vice versa, demonstrating a 90° phase shift between the peaks and hence the orthogonality in polarization selectivity of the two sets of valleys responsible for such PL emissions. The polar plots of the peak height intensities against θ for the 817nm and 995nm peaks are presented in Figure 18b and c respectively.

We attribute the presence of a double peak at the short wavelength regime to the presence of two peaks in the valence band along the ΓY direction, which can potentially allow two transitions of different energy values from the conduction band to the valence band. As both peaks lie on the ΓY axis, they will obey the same selection rules. This observation may also be caused by other higher order transitions and has yet to be fully understood by the time this thesis is written.

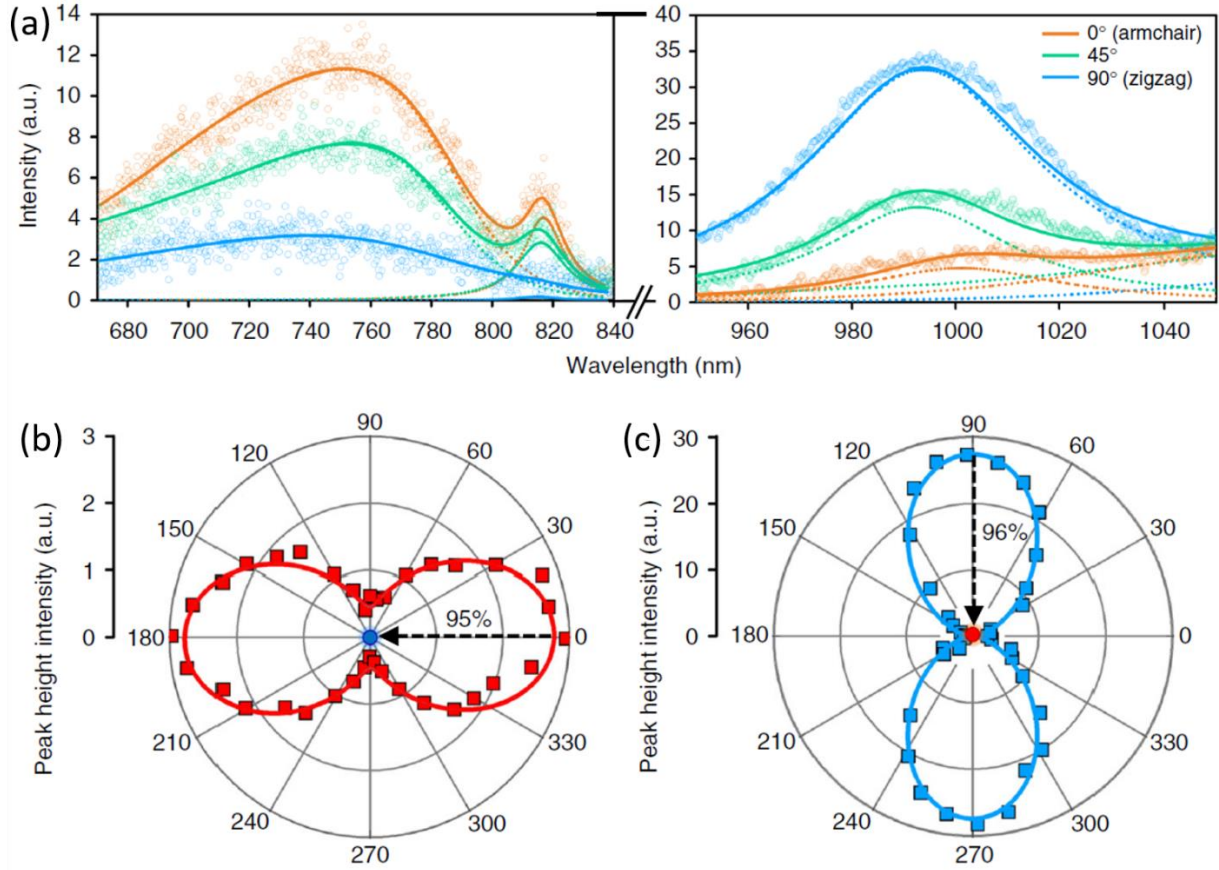


Figure 18: Photoluminescence measurements of SnS. (a) Deconvolutions of PL peaks under parallel polarization at 817 and 995 nm give clear, opposite trends with respect to sample orientation, demonstrating the identity of the valley positions. (b), (c) Polar plots of PL peak height intensities conducted under parallel polarization for the valleys at 817 and 995 nm, respectively (squares). The single circular data point in each polar plot represents the PL peak height intensities of the corresponding measurements conducted with the second polarizer perpendicular to the incident light when the respective axes are aligned to the excitation polarization. The black dashed arrows connect the two data points before and after the 90° rotation of the second polarizer, showing 95% and 96% decrease in PL intensities at the ΓY and ΓX valleys respectively. (adapted from [8]).

2.3.4.1. Polarization degrees

An important figure of merit for valleytronic systems is the polarization degrees of the valleys, P [12], which can be obtained by comparing the PL intensities at each valley. For previously demonstrated 2D systems, P_{2D} has been defined as [12]:

$$P_{2D} = \frac{I(\sigma_-) - I(\sigma_+)}{I(\sigma_-) + I(\sigma_+)}$$

where $I(\sigma_{-/ +})$ represents the PL intensities that are left and right circularly polarized respectively. Since the transitions at each valley in SnS is purely symmetry-dependent, PL at

each valley will be linearly polarized along the same direction as the incident excitation-allowed light; PL conducted under parallel polarization will thus demonstrate valley selectivity for both absorption and emission and can be used to calculate the polarization degrees between the non-degenerate valleys. We define these as the intervalley polarization degrees:

$$P_{intervalley,\Gamma X} = \frac{I_{\Gamma X\parallel}(\theta=90^\circ) - I_{\Gamma Y\parallel}(\theta=90^\circ)}{I_{\Gamma X\parallel}(\theta=90^\circ) + I_{\Gamma Y\parallel}(\theta=90^\circ)} \text{ and } P_{intervalley,\Gamma Y} = \frac{I_{\Gamma Y\parallel}(\theta=0^\circ) - I_{\Gamma X\parallel}(\theta=0^\circ)}{I_{\Gamma Y\parallel}(\theta=0^\circ) + I_{\Gamma X\parallel}(\theta=0^\circ)}$$

where $P_{intervalley,i}$ and $I_{i\parallel}(\theta)$ stands for the polarization degree and PL intensity under parallel polarization for the i valley respectively. $P_{intervalley,i}$ are lower-bound estimations of the polarization degrees at both sets of SnS valleys due to certain logical simplifications made because of the non-degeneracy of the valleys. Such estimations include (i) comparing the intensities at the two valleys at 0° and 90° only under parallel polarization, (ii) taking the intensity values from the fitted polar plots, and (iii) using normalized intensity at each valley to eliminate issues of differing emission and detection efficiencies at the two valleys.

For the peaks at 817nm (ΓY) and 995nm (ΓX), as shown in Figure 18b and c, we calculated $P_{intervalley,\Gamma Y} = 92\%$ and $P_{intervalley,\Gamma X} = 62\%$ respectively.

The uniqueness of SnS as a valleytronic system lies in the non-degeneracy of the valleys, which, unlike previous 2D materials, can be viewed as not only having an additional valley degree of freedom, but one that can be accessed via two routes; between valleys and within valleys, thereby allowing an additional valley selection pathway for applications. For anisotropy within each valley, we define the intravalley polarization degrees:

$$P_{intravalley,\Gamma X} = \frac{I_{\Gamma X\parallel}(\theta=90^\circ) - I_{\Gamma X\perp}(\theta=90^\circ)}{I_{\Gamma X\parallel}(\theta=90^\circ) + I_{\Gamma X\perp}(\theta=90^\circ)} \text{ and } P_{intravalley,\Gamma Y} = \frac{I_{\Gamma Y\parallel}(\theta=0^\circ) - I_{\Gamma Y\perp}(\theta=0^\circ)}{I_{\Gamma Y\parallel}(\theta=0^\circ) + I_{\Gamma Y\perp}(\theta=0^\circ)}$$

We identified the maximum PL intensities for both valleys ($\theta=90^\circ$ for ΓX and $\theta=0^\circ$ for ΓY) and conducted PL measurements under cross polarization (second polarizer placed perpendicular to excitation polarization (Figure 11)), obtaining near-zero $I_{i\perp}(\theta)$ for both valleys (Figure 18b and c), giving $P_{intravalley,\Gamma Y} = 95\%$ and $P_{intravalley,\Gamma X} = 96\%$ respectively. The large difference between $I_{i\perp}(\theta)$ and $I_{i\parallel}(\theta)$ at each valley further reinforces the notion of strong valley emission anisotropy at both valleys. Our P values are amongst the highest polarization degrees reported, even rivalling those of monolayer dichalcogenides obtained from experiments conducted at cryogenic temperatures [12] [14] [52].

2.4. Concluding remarks

In conclusion, we discovered the existence of two band gaps at 1.28eV and 1.48eV in bulk SnS under ambient conditions and without additional biases. These band gaps reside along the ΓY and ΓX axes in reciprocal space, are strongly and solely excited by y- and x-polarized light and also mostly emits y- and x-polarized light respectively, effectively serving as non-degenerate valleys. Our PL and absorption data complement each other, providing a definite

proof of the selectivity towards the absorption of polarized light, specifically backing the claim that the valleys indeed possess selectively for both absorption and emission of light. Our system also has, nominally, the advantage of superior optical dichroic anisotropy of up to 600%, intravalley polarization degrees of 96% and 95% respectively and intervalley polarization degrees of 62% and 92% respectively. Such attributes make SnS a model system and allow future work to be conducted with more controllability and potential for practical applications.

Chapter Three²

3. Generalization of valleytronics effect to IV-VI monochalcogenides – Tuneable valleytronics in $\text{SnS}_x\text{Se}_{1-x}$ alloy system

3.1. Motivation for generalization - $\text{SnS}_x\text{Se}_{1-x}$ as a model system

In the previous chapter we show the first demonstration of the actual manipulation of valley population under ambient and bias-free conditions with a high polarization degree in a novel form of valleytronics in SnS [8]. Such novelty has a two-fold manifestation. First, the two sets of valleys in SnS reside along the ΓY and ΓX directions in reciprocal space respectively, and, by the selection rules, are exclusively selected by y and x polarized light respectively. Second, the anisotropic nature of the material bestows upon the valleys the non-degeneracy in bandgap values. As such, both incident light polarization and energy can potentially be used to independently access each valley, granting the material system more flexibility in terms of excitation conditions.

However, the choice of working wavelengths is still limited to only that of SnS. An important extension to such flexibility is then to expand such novel valleytronics to the rest of the IV-VI family, which will not only allow a wider wavelength range for excitation/emission but, more importantly, prove that such novel valleytronics is a general behavior within the material system, i.e. specific material composition is not critical to the utilization of such properties, hence demonstrating the suitability of such material system for practical applications.

Herein, we report a model system in $\text{SnS}_x\text{Se}_{1-x}$, $0 \leq x \leq 1$, demonstrating both the retainment of valley selectivity and the gradual tuning of bandgaps at both valleys across all alloy compositions. This is the first demonstration of a tunable valleytronics platform; the retainment of PL intensity and polarization degrees across the whole compositional range proves that IV-VI materials are suitable for such novel valleytronics in general.

$\text{SnS}_x\text{Se}_{1-x}$ was chosen because of the similarity in band structures for SnS and SnSe, with the presence of two valleys along the ΓY and ΓX axes and the band separation at the Γ point having a larger value than the two valleys [23]. Since both materials' band structures arise from combinations of the same constituent wavefunctions [53], which satisfies the same symmetry considerations [54], valley selection rules in SnS have to also apply to SnSe, along

² Reproduced in part with permission from [9].

with all $\text{SnS}_x\text{Se}_{1-x}$ compositions. We present the verification of this hypothesis by experiments and theory in detail in the following sections.

3.2. Synthesis of bulk $\text{SnS}_x\text{Se}_{1-x}$ plates

3.2.1. Experimental procedures - Physical Vapor Deposition (PVD)

PVD was employed to synthesize the bulk $\text{SnS}_x\text{Se}_{1-x}$ plates, as detailed in the previous chapter, on fused silica substrates (for PL measurements) and on Si/SiO₂ substrates (for reflection measurements). 99.5% -4 mesh SnS powder and 99.999% (metals basis) SnSe powder, both from Alfa Aesar are used. We synthesized alloys of nine different compositions, with nominal decrements of $\Delta x = 0.125$, by replacing 1-x amount of SnS by an equal molar ratio of SnSe. The SnS-SnSe mixture was ground using mortar and pestle to ensure well mixing before being placed in the furnace as the source.

3.2.2. Material characterization

Figure 19 [9] shows the optical microscopy, SEM, and SEM-EDX results of alloy samples with nominal decrements of $\Delta x = 0.125$. Similar to SnS (Figure 12 [8]), we observed flat surfaces and homogeneous distributions of Sn, S, and Se across all alloy compositions. This means that our PVD method only produced single alloy compounds and no phase segregation occurred.

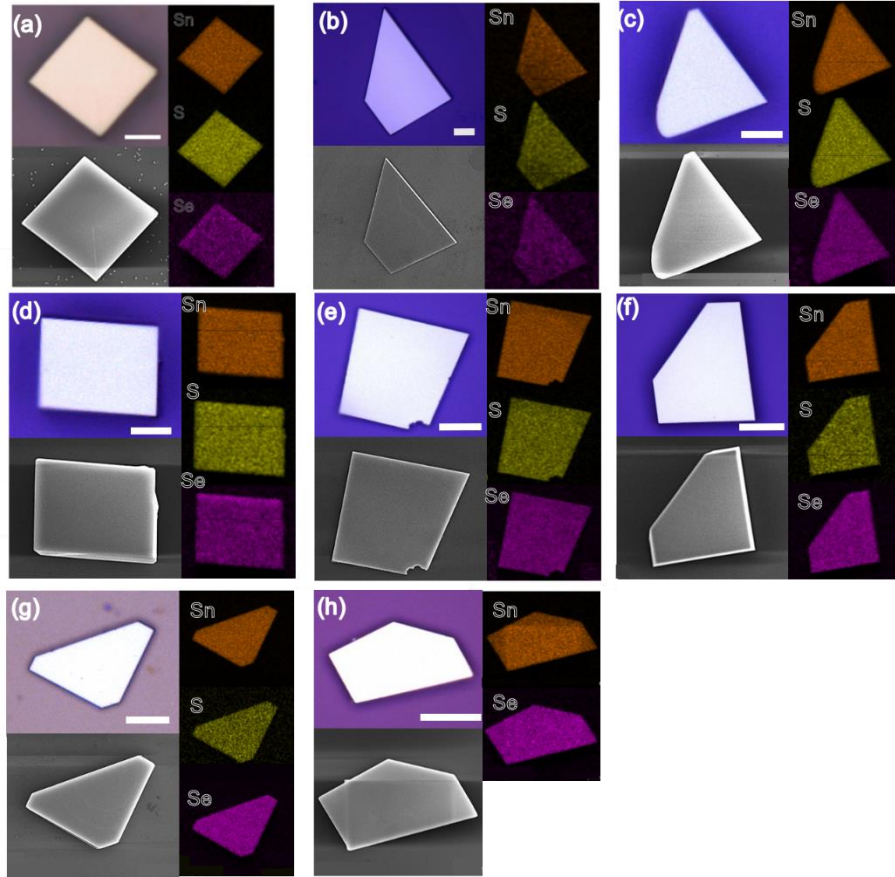


Figure 19: Optical microscopy image, scanning electron microscopy (SEM) images and Energy-dispersive X-ray spectroscopy (EDX) maps of nominally (a) $\text{SnS}_{0.875}\text{Se}_{0.125}$, (b) $\text{SnS}_{0.75}\text{Se}_{0.25}$, (c) $\text{SnS}_{0.625}\text{Se}_{0.375}$, (d) $\text{SnS}_{0.5}\text{Se}_{0.5}$, (e) $\text{SnS}_{0.375}\text{Se}_{0.625}$, (f) $\text{SnS}_{0.25}\text{Se}_{0.75}$, (g) $\text{SnS}_{0.125}\text{Se}_{0.875}$, and (h) SnSe , demonstrating flat surfaces and homogeneous distributions of Sn, S, and Se. Scale bars are $5\mu\text{m}$. (adapted from [9])

3.2.3. Limitations in alloying using PVD

The exact S:Se ratios obtained from SEM-EDX (Figure 20a and b [9]) follow a gradual trend, as presented in the plot of actual composition versus nominal (design) composition (Figure 20c [9]); our SEM-EDX results reflect the continuous compositional tunability using our growth method. However, the Se content of all compositions is consistently higher than the design amount. While this can be attributed to the lower equilibrium vapor pressure of SnSe as compared with SnS [37] [55], which is commonly reflected in the higher required PVD growth temperature of SnSe as compared with SnS [34] [41], further tuning of alloy composition for large S content will require more complicated methods, such as S compensation [56] or multi-sourced CVD methods [33] [57].

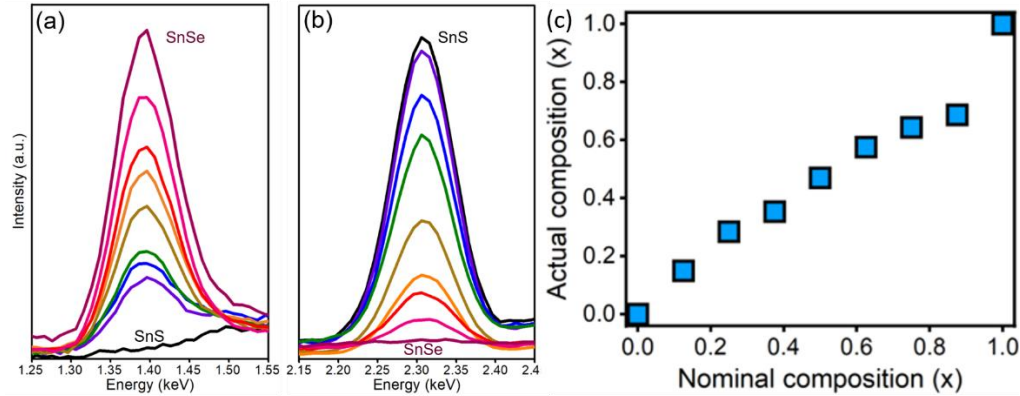


Figure 20: (a) and (b) Peak intensities for S and Se in SEM-EDX spectra. Trends in peak height intensity of (a) Se and (b) S at the respective energies of 1.4eV and 2.3eV, showing a general trend of increasing (decreasing) intensity with more Se content for the Se (S) peak. (c) Trend in actual composition versus nominal (design) composition, showing a general excess of Se content. (adapted from [9]).

Further, in our preliminary attempts in growing alloys of SnS and GeS, we realized that the much larger difference in optical growth conditions [58] for the single phase material, which again signifies the larger difference in equilibrium vapor pressures at our chosen growth conditions, prevents the simultaneous deposition of both materials into a single alloy compound. This limits the utility of PVD in these alloy growths.

3.3. Symmetry-dependent valleytronics demonstrated via optical means

3.3.1. Experimental procedures

Optical methods and analyses applied to the alloys are built upon the procedures listed in the previous chapter. Because SnSe and the alloys have increasing smaller band gaps (features at longer wavelengths) as compared with SnS, the PL peak position, intensity, and FWHM values for the Γ X valley transitions that are beyond the detection range of the visible Si detector were obtained from PL spectra with 785nm excitation and using an infrared InGaAs detector. Since both detectors' efficiencies, based on the spectral response of Si and InGaAs, drop within the range of \sim 900nm to \sim 1100nm [59], we note that the exact peak position and intensity values measured within that range may not reflect quantitatively the exact values of the emission. For consistency, we extrapolated these values, using overlapping measurements of alloy compositions $x = 0.5, 0.625,$ and 0.75 into the measured visible data to obtain the trends reported in this work.

3.3.2. Raman measurements – variations in Raman modes across alloy compositions

Raman spectra of SnS [34] and SnSe [41] under $-z$ excitation (perpendicular to the layers) contain characteristic peaks that correspond to three A_g modes and one B_{3g} mode. We observed that these modes follow gradual shifts for the alloys (Figure 21a and b [9]). We used the relative peak intensities [8] to determine the armchair (y) and zigzag (x) directions of each alloy composition, and presented the respective spectra under 532nm excitation when the incident polarization is aligned along the x and y axes for parallel ((Figure 21a [9]) and cross ((Figure 21b [9]) polarization configurations. Note that the peak for the $A_g^{(1)}$ mode of SnSe cannot be observed due to the wavenumber being lower than the Raman filter edge. Also, for clarity, Raman spectra aligned along the y axis under parallel excitation is repeated using 785nm excitation to clearly distinguish and reveal the trends for the $A_g^{(3)}$ modes of the alloys, presented in Figure 21c [9].

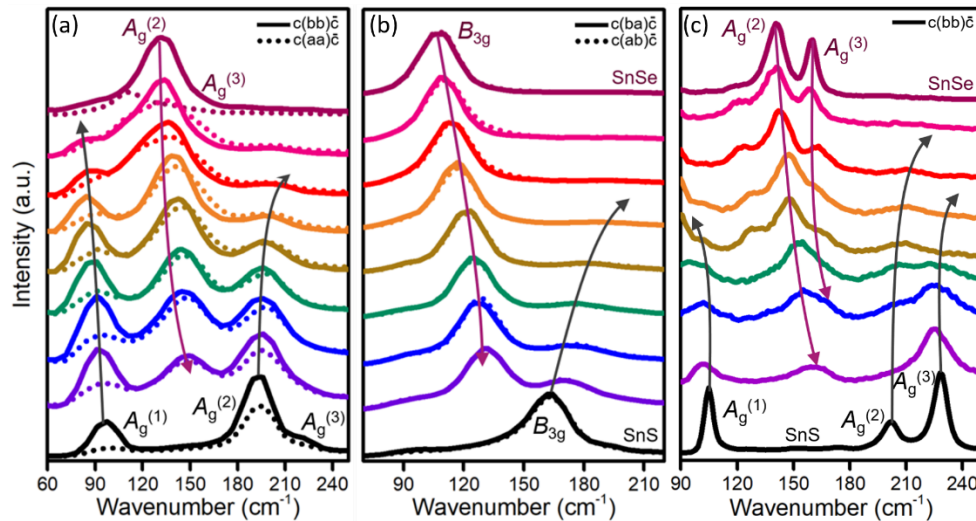


Figure 21: Reflection mode, $c(xx)c^-$ Raman spectra. The first and second letters in the parentheses denotes the alignment of the incident light and emitted signal. Only spectra aligned along x and y directions are presented.

(a) Raman spectra obtained under parallel polarization using 532nm excitation, showing clear trends in intensities for the A_g modes, thus ascertaining the identity and orientation of the measured samples. (b) Raman spectra obtained under cross polarization using 532nm excitation, showing clear trends in intensities for the B_{3g} modes. (c) Raman spectra obtained under parallel polarization using 785nm excitation aligned along the y axis, showing two-mode behavior for the $A_g^{(3)}$ mode. (adapted from [9]).

We observed a clear two-mode behavior for all Raman peaks, where the alloys can exhibit two peaks (SnS-like and SnSe-like) that belong to the same Raman mode. This alloy behavior can be explained using the modified random element isodisplacement (MREI) model [60] [61], where strong S-Se interactions gives two eigenvalues, one SnS-like and one SnSe-like, as the solutions to the quadratic equation of the model. This observation agrees with the common understanding that SnS and SnSe possess comparable interlayer and intralayer

forces, as evidenced by the relatively small difference in interlayer and intralayer atomic distances [23]. Since all Raman modes of concern here are related to relative interlayer motions [41], S-Se interactions should be significant, which explains the two-mode behavior.

3.3.3. White light reflection (R) and transmission (T) measurements

3.3.3.1. Tunability of band gaps

Tunability of bandgap values at each valley is demonstrated using R and T measurements (and substantiated using PL measurements, as presented in the following section). R and T measurements were conducted with the incident excitation polarized along the y or x direction, hence demonstrating valley selectivity for absorption. Normalized Tauc plots are presented in Figure 22 [9], clearly showing the decrease in optical bandgap values as Se content increases. Using Tauc plot analyses, we show that the bandgaps can be gradually tuned within a range of 1.28eV to 1.05eV and 1.48eV to 1.24eV for the ΓX and ΓY valleys respectively.

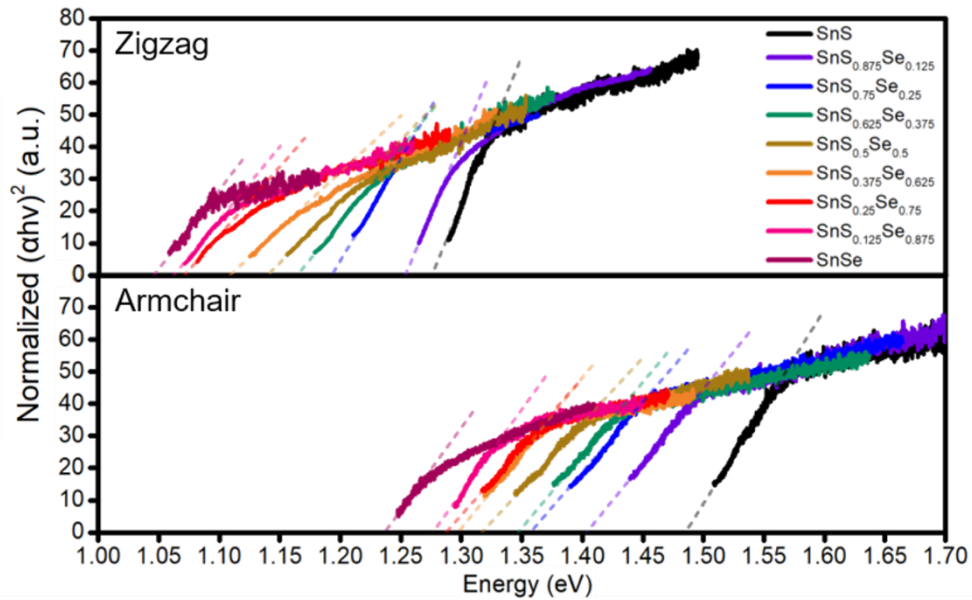


Figure 22: Normalized Tauc plots of both directions for different alloy compositions obtained from white light R and T measurements, showing a distinct decrease in bandgap value with increasing Se content. (adapted from [9]).

Through this, we demonstrate the continuous tuning of bandgaps for both valleys across the whole compositional range; the range of bandgaps (1.28eV to 1.05eV and 1.48eV to 1.24eV for the two valleys respectively) is much larger than that of 2D semiconductor alloys [60] [62] [63] [64], especially when considering the combined effects of both valleys under

different polarizations. This ensures the practicality of using such systems in devices with stringent operational wavelength considerations. Furthermore, typical advantages of semiconductor alloys over pure semiconductors, including the flexibility in choice of synthesis methods [62] and the additional parameter of lattice matching [65], can be utilized on top of bandgap tunability.

3.3.4. Photoluminescence (PL) measurements

PL measurements were conducted under parallel or cross polarization, with a second polarizer serving as an analyser placed before the detector, to further demonstrate selectivity for emission. Figure 23 [9] shows the PL spectra under parallel polarized 532nm that is aligned to the y and x axes for all alloy compositions, which elucidates the presence of a single PL peak in each spectrum that corresponds to the ΓY and ΓX valleys respectively. It can be observed that the PL peak positions red-shifts with more Se for a range of 1.29eV to 1.20eV and 1.64eV to 1.45eV respectively. This agrees with the decrease in optical bandgap values obtained from R and T spectra.

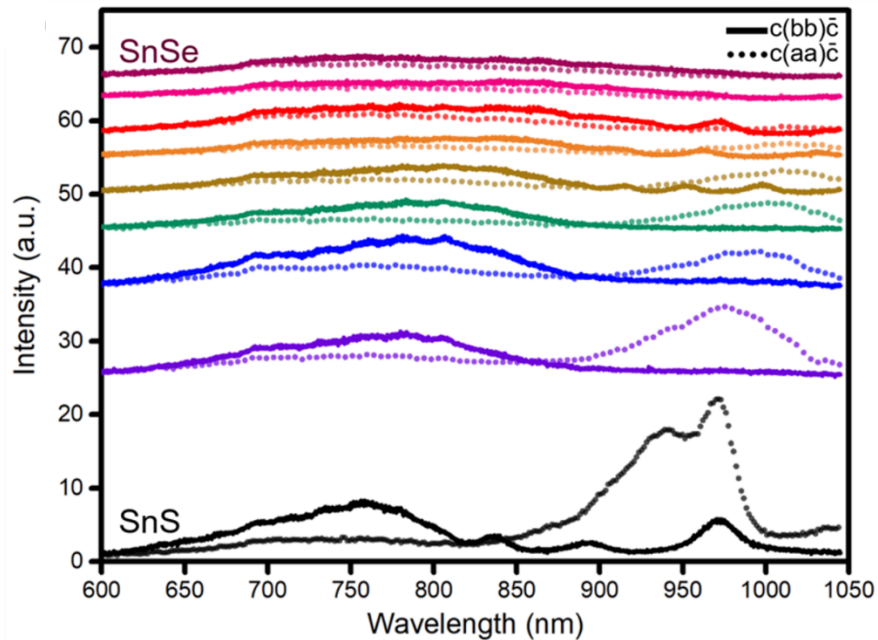


Figure 23: PL peaks under parallel polarization. Only spectra aligned along x and y directions are presented, showing that for all alloy compositions, the high (low) energy peak has the strongest intensity when the excitation light is polarized along the y (x) direction, showing the retainment of valley selectivity across all alloy compositions. There is also a clear trend of decrease in bandgap value with increasing Se content. (adapted from [9]).

3.3.4.1. Vegard's Law and Polarization degrees

Optical bandgaps obtained by white light R and T, as well as PL measurements, are presented in Figure 24a, clearly showing the first observation of tunable, wavelength-dependent, non-degenerate valleytronics in $\text{SnS}_x\text{Se}_{1-x}$. For practical purposes, it is thus important to apply Vegard's law [66] to generate a database for the bandgap values and the bowing parameter, b [67]. Fig. 4b shows the optical bandgap values obtained via white light R and T as well as PL for both valleys, plotted in compositional space. Using

$$E_{g,\text{SnS}_x\text{Se}_{1-x}} = xE_{g,\text{SnS}} + (1-x)E_{g,\text{SnSe}} + bx(1-x)$$

we obtained $b_{\Gamma Y(\text{white light})} = -0.11185\text{eV}$, $b_{\Gamma X(\text{white light})} = -0.0331\text{eV}$, $b_{\Gamma Y(\text{PL})} = -0.06843\text{eV}$, and $b_{\Gamma X(\text{PL})} = -0.0521\text{eV}$, respectively. The fitted functions are also overlaid in Figure 24a. We note that the bowing parameters obtained for the valleys using both absorption and PL methods are close to each other and very small [68], which gives a rather linear relationship that simplifies the tunability.

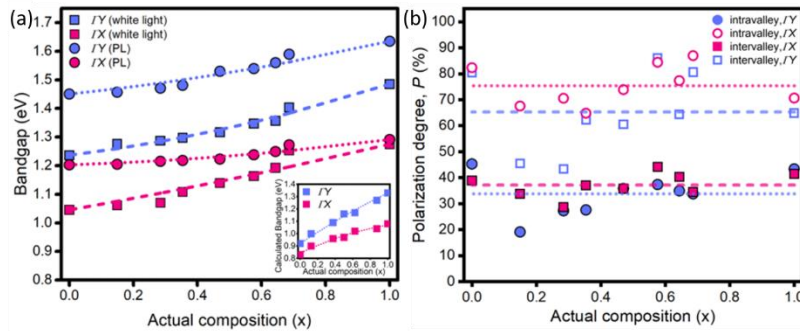


Figure 24: (a) Optical bandgaps obtained by white light R and T as well as PL measurements, plotted with fitting functions using Vegard's law. Calculated bandgap values are presented in the inset, showing a smooth variation and similar trends for both ΓY and ΓX valleys respectively. (b) Trends in polarization degrees with compositional variation, showing the retainment of high valley selectivity across all alloy compositions in $\text{SnS}_x\text{Se}_{1-x}$. Intervalley (intravalley) polarization degrees are presented as squares (circles), with dashed (dotted) lines demarcating the respective average values. Solid and open data points denotes the polarization degrees that depends predominantly on PL signals of the ΓY and ΓX valleys respectively. (adapted from [9])

We further quantify such retainment of valley selectivity with the figures of merit, the intervalley ($P_{\text{intervalley},\Gamma Y/\Gamma X}$) and intravalley ($P_{\text{intravalley},\Gamma Y/\Gamma X}$) polarization degrees, as mentioned in the previous chapter. It is clear from Figure 23, that $P_{\text{intervalley},\Gamma Y/\Gamma X}$ (Figure 24b) remains significant across all compositions. Results from PL measurements conducted under cross polarization were then used to calculate $P_{\text{intravalley},\Gamma Y/\Gamma X}$, which are also presented in Figure 24b. The strong polarization degrees of, for example, up to 91% and an average of 75% for $P_{\text{intravalley},\Gamma Y/\Gamma X}$, proves that the alloys still rival results obtained using monolayer TMDCs from experiments conducted at cryogenic temperatures [12] [14] [52].

3.3.4.2. Trends in PL peaks' intensity and full-width at half-maximum (FWHM) across alloy compositions

Interestingly, we also observe from Figure 23 that the full-width at half-maximum (FWHM) of the PL peaks (Figure 25a and b) increases with greater Se content, along with a decrease in PL intensity (Figure 25c).

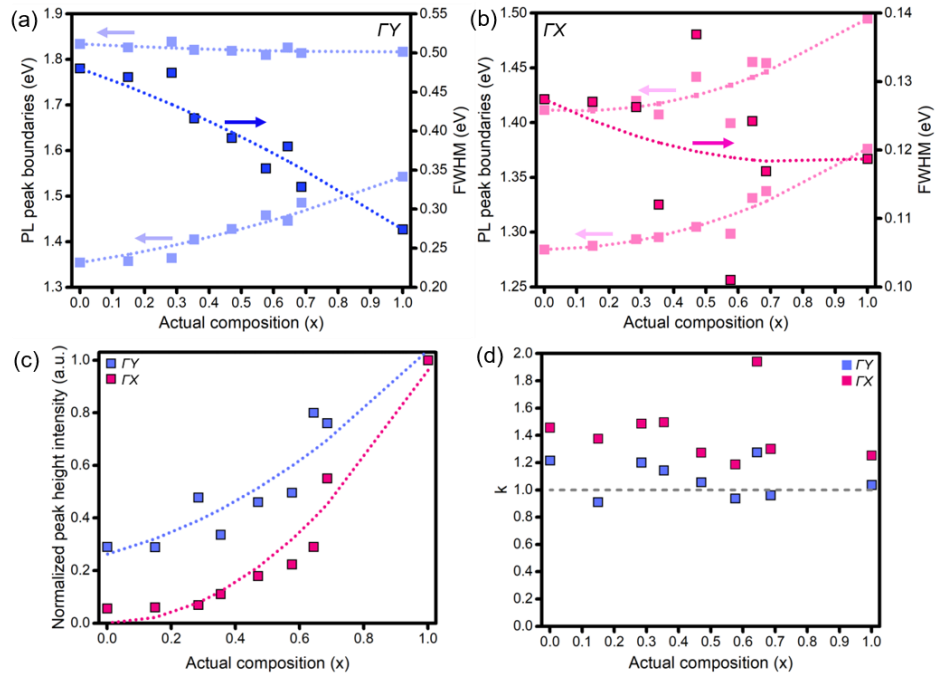


Figure 25: Nature of bandgap transitions in $\text{SnS}_x\text{Se}_{1-x}$. (a) Trends in FWHM (darker shade) for the ΓY peak with compositional variation, showing an increasing trend with more Se respectively. The exact location of the boundaries of the peak at FWHM is also presented in a lighter shade. (b) Corresponding trends in FWHM for the ΓX peak. (c) Trends in PL peak height intensity with alloy composition, showing a decreasing trend with more Se (lower x). The intensity for SnS is normalized to one for clarity in presentation. (d) Fitted k coefficient of $I_{PL} \propto I_{excitation}^k$, obtained from power dependence PL measurements at the respective peak height positions. $k = 1$ denotes the boundary between the presence and absence of donor/ acceptor assisted exciton recombination. (adapted from [9]).

3.3.4.4. Excitation power-dependent measurements

To understand the effect on the nature of the bandgap transitions with alloying, we conducted power-dependent PL measurements and fitted the PL peak intensity using a power law, $I_{PL} \propto I_{excitation}^k$, where, for an excitation energy higher than the bandgap, the exact value of the coefficient k lies in the range $1 < k < 2$ for free or bound exciton recombination and $0.5 < k < 1$ for free-to-bound recombination involving donors or acceptors, a sign of eventual saturation of PL intensity with a saturation of donor or acceptor states [69] [70].

Figure 25d shows the trends in PL intensities and the fitted k coefficients, clearly showing that the k coefficients for transitions at both valleys generally remain close to or above 1 for most alloy compositions. This shows that acceptor and donor levels generally are not involved in the recombination that leads to the emission of PL, hence serving as a secondary evidence that we are only probing the CB to VB transitions. This agrees with other observations and theoretical understanding of the above-mentioned selection rules, thus re-ascertains the validity of the notion that valley selectivity is retained across all alloy compositions.

We also note that while the k coefficients of ΓX transitions averaged to be 1.42, the corresponding average value for ΓY transitions is 1.08. The above-mentioned power law is derived [69] from the relation $I_{PL} \propto n^2$ for free or bound excitons recombination assuming charge neutrality, coupled with the relations $n \propto I_{excitation}$ or $n \propto I_{excitation}^{0.5}$ for free electron-hole pairs recombining via defect states or excitons being the dominant mechanisms respectively, hence giving $I_{PL} \propto I_{excitation}^2$ and $I_{PL} \propto I_{excitation}^1$ respectively. For free-to-bound transitions, assuming an excitation intensity- independent donor/acceptor concentration, $I_{PL} \propto n$, hence giving $I_{PL} \propto I_{excitation}^1$ and $I_{PL} \propto I_{excitation}^{0.5}$ for the two above-mentioned recombination mechanism.

We see that while the ΓX transitions are clearly due to free or bound excitonic recombination with a mixture of recombination mechanisms, the acceptor levels may, albeit in a non-dominant fashion, contribute to the ΓY transitions, leading to the much lower observed k values. This can be explained by the higher energies of the ΓY VB edge as compared with that of the ΓX VB, which for most self-doped cases of SnS, lie closer to or coincides with that of the acceptor levels contributed by the Sn vacancies [71] [72].

This may also explain for the much lower $P_{intravalley,\Gamma Y}$ and $P_{intervalley,\Gamma X}$ as compared with $P_{intravalley,\Gamma X}$ and $P_{intervalley,\Gamma Y}$ across all compositional range, as presented in Figure 24b, since the two former figures of merit are compromised with substantial $I_{\Gamma Y \perp}(\theta = 0^\circ)$ and $I_{\Gamma Y \parallel}(\theta = 90^\circ)$; one possible area of improvement for valleytronics performance is thus by dopant level engineering.

3.4. Theoretical validations via analysis of $\text{SnS}_x\text{Se}_{1-x}$ band diagrams

Both SnS and SnSe have the Pmcn crystal structure with an orthorhombic unit cell comprising of puckered layers [73], and the lattice parameters of $\text{SnS}_x\text{Se}_{1-x}$ has been experimentally shown to vary gradually across the alloy compositions [74]. As such, we calculated the bandstructures $\text{SnS}_x\text{Se}_{1-x}$ by constructing supercells in $\Delta x=0.125$ increments. Using a quadratic fit of experimentally measured lattice parameters from [74], we adopted the simplest case of homogeneous alloying [62], where S and Se are positioned in the most well-mixed and randomly-occupied fashion. $2 \times 2 \times 2$ (8 atoms) supercells of SnS, SnSe, and $\text{SnS}_{0.5}\text{Se}_{0.5}$, as presented in Figure 26, were used. For other alloy compositions, $4 \times 4 \times 2$ (32

atoms) supercells were required to have sufficient number of atoms for the representation of mixing.

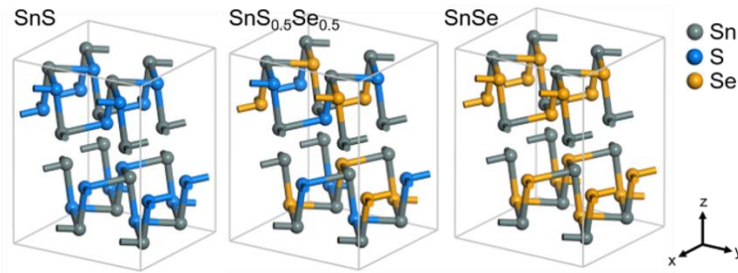


Figure 26: 2x2 supercells of molecular structures of SnS, SnSe, and the SnS_{0.5}Se_{0.5} alloy with the simplest case of homogeneous alloying. The puckered arrangement of atoms and the high anisotropy along the y (armchair) and x (zigzag) directions is maintained across the whole compositional range while the lattice parameters increase with Se content. (adapted from [9]).

DFT calculations were conducted in the Vienna Ab initio Simulation package (VASP) [75] to compute the electronic structures. The projector augmented-wave (PAW) [76] pseudopotentials and the Perdew--Burk--Ernzerhof generalized-gradient approximation functional [27] were adopted with an energy cutoff of 520 eV. The self-consistent-field and geometry convergence tolerance values were set to 1×10^{-3} and 1×10^{-2} eV, respectively. The energy, band character and band gap of the 8-atom cells were compared with those of randomly occupied 32-atom cells, to validate the simplified 8-atom models. The energy above hull difference is within 5 meV/atom for all models used in our calculation, as presented in Figure 27. Despite the issue of band folding in the 32-atom cells bandstructures, the $p_x/p_y/p_z$ orbital components near the band edge are primarily the same, and the band gap values were consistent within 0.03 eV for 8- and 32-atom structures of SnS, SnS_{0.5}Se_{0.5}, and SnSe.

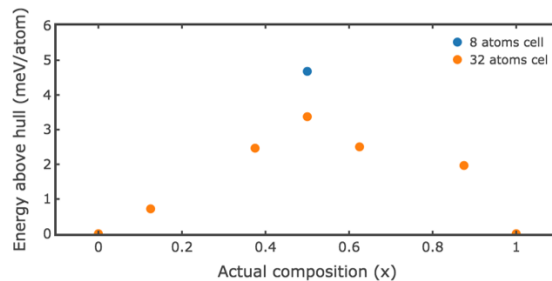


Figure 27: Calculated Energy above hull per atom of SnS_xSe_{1-x}, showing that the energy above hull difference is within 5 meV/atom for all models used in our calculation (adapted from [9]).

Our DFT calculations yield band structures with two local band gaps along the ΓY and ΓX axes, denoted by $E_{g,\Gamma Y}$ and $E_{g,\Gamma X}$ respectively, across the whole compositional range. 8-atom cells bandstructures for SnS, SnS_{0.5}Se_{0.5}, and SnSe are presented in Figure 28, while 32-atom cells bandstructures for all compositions are presented in Figure 29.

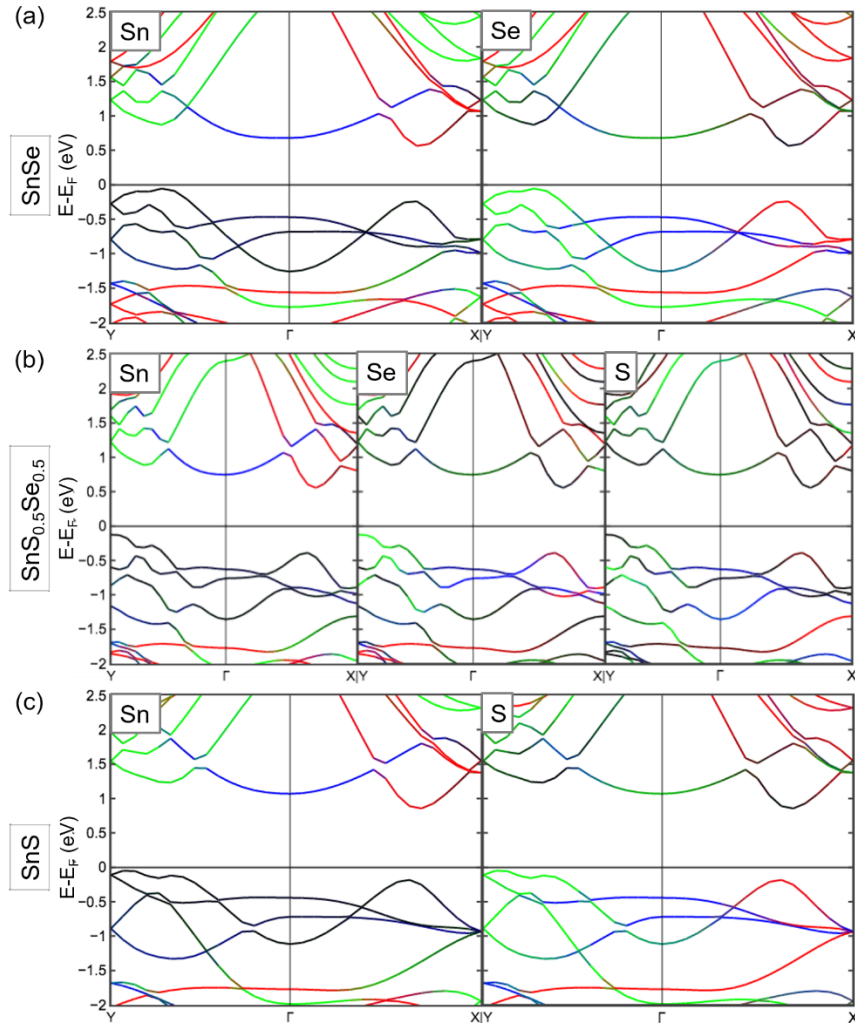


Figure 28: Calculated band structures for selected SnS_xSe_{1-x}. Orbital projected band structures along Y- Γ -X of representative alloy compositions of (a) SnSe, (b) SnS_{0.5}Se_{0.5}, and (c) SnS are presented. Band structures are projected on elements of Sn, S and Se. Red, green, and blue shades correspond to contributions of each subband by p_x, p_y, and p_z orbitals respectively. Our elemental and orbital specific band structures denote that for all alloy compositions, p orbitals from Sn and the chalcogenides make up predominantly the conduction and valence bands, (adapted from [9]).

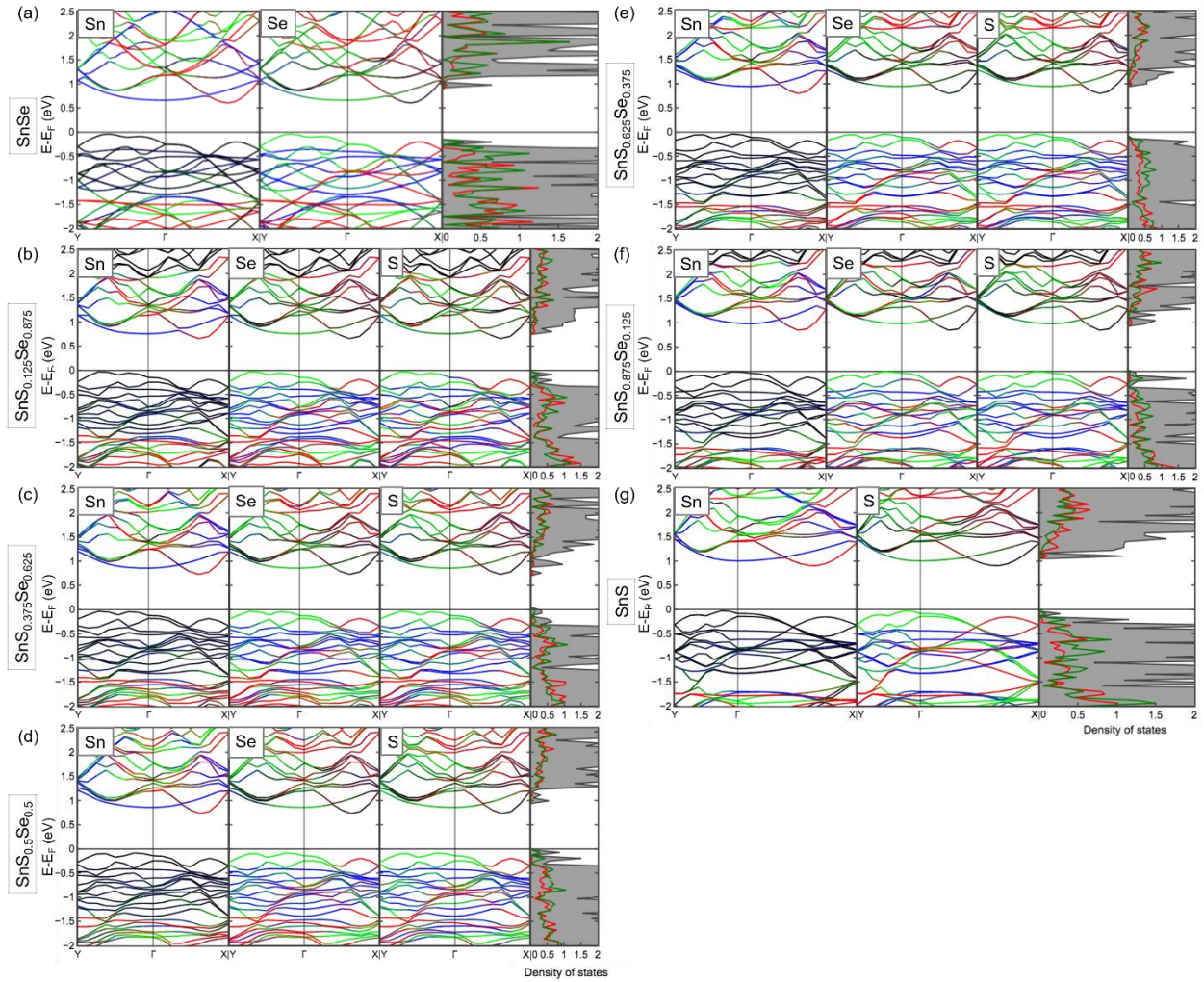


Figure 29: Calculated bandstructures and density of states (DOS) plots for $\text{SnS}_x\text{Se}_{1-x}$. The bandstructures and DOS plots for alloys, calculated using unit cells with 32 atoms, are included in (a) SnSe , (b) $\text{SnS}_{0.125}\text{Se}_{0.875}$, (c) $\text{SnS}_{0.375}\text{Se}_{0.625}$, (d) $\text{SnS}_{0.5}\text{Se}_{0.5}$, (e) $\text{SnS}_{0.625}\text{Se}_{0.375}$, (f) $\text{SnS}_{0.875}\text{Se}_{0.125}$, and (g) SnS . Band structures are projected on elements of Sn, S and Se. Red, green, and blue shades correspond to contributions of each subband by p_x , p_y , and p_z orbitals respectively. (adapted from [9]).

3.4.1. Incremental variations in bandgap values at both valleys

The trends in calculated band gap values agrees with that of the PL and white light band gap values for the valleys, as shown in the inset of Optical bandgaps obtained by white light R and T, as well as PL measurements, are presented in Figure 24a, clearly showing the first observation of tunable, wavelength-dependent, non-degenerate valleytronics in $\text{SnS}_x\text{Se}_{1-x}$. For practical purposes, it is thus important to apply Vegard's law to generate a database for the bandgap values and the bowing parameter, b . Fig. 4b shows the optical bandgap values obtained via white light R and T as well as PL for both valleys, plotted in compositional space. Using

$$E_{g,SnS_xSe_{1-x}} = xE_{g,SnS} + (1-x)E_{g,SnSe} + bx(1-x)$$

we obtained $b_{\Gamma Y(\text{white light})} = -0.11185\text{eV}$, $b_{\Gamma X(\text{white light})} = -0.0331\text{eV}$, $b_{\Gamma Y(\text{PL})} = -0.06843\text{eV}$, and $b_{\Gamma X(\text{PL})} = -0.0521\text{eV}$, respectively. The fitted functions are also overlaid in Figure 24a. We note that the bowing parameters obtained for the valleys using both absorption and PL methods are close to each other and very small, which gives a rather linear relationship that simplifies the tunability.

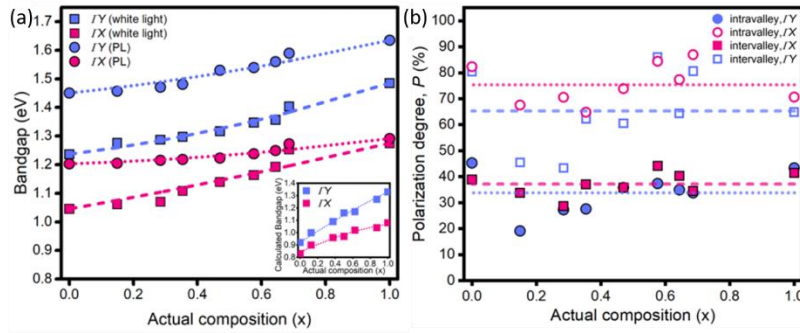


Figure 24a [9], and can be explained using the difference in contributions of elemental atomic orbitals to the sub-bands that make up the CBM and VBM. Orbital projected band structures in Figure 28 [9] and Figure 29 [9] show that the CBMs are predominantly made up of 5p orbitals from Sn, while the VBMs are mainly composed of p orbitals of chalcogenide atoms. The contribution by Se is from the 4p orbitals, which is higher in energy as compared with the 3p orbitals of S. Therefore, with a greater Se content, the hybridised orbitals that make up the VBM of alloys will have more Se character, hence leading to a smaller bandgap. This is clearly shown in Figure 28b [9], where the VBM of $\text{SnS}_{0.5}\text{Se}_{0.5}$ is contributed mostly by Se orbitals.

3.4.2. Retainment of symmetry and selection rules of conduction and valence bands at both valleys

Our DFT calculations show that the CBM and VBM along ΓX (ΓY) is contributed almost entirely by p_x (p_y) orbitals. This confirms that the symmetry of the wavefunctions that make up the CB and VB along ΓX and ΓY for all alloy compositions remain the same as that of SnS; the irreducible representations of orbitals that make up the CBM and VBM remain the same across all compositions. Hence, using our previously discussed selection rules in the previous chapter, CB to VB transitions at the valleys can only occur for light polarized along the x and y directions respectively; valley selectivity is retained across all $\text{SnS}_x\text{Se}_{1-x}$ alloy compositions, in agreement with the experimental results shown above.

3.5. Concluding remarks

In this chapter, we elucidate the robustness and tunability of a novel form of non-degenerate valleytronics in a $\text{SnS}_x\text{Se}_{1-x}$ alloy system, a clear and important extension and generalization of the effect on SnS as presented in the previous chapter. The novel form of valleytronics presented is purely symmetry-dependent. This means that such valleytronic effect will potentially be present in many different materials with non-degenerate bandgaps as long as the symmetry requirements are fulfilled. Such generalization may allow the discovery of a large family of valleytronics materials, which may provide more versatile options for various practical applications. It will also be intriguing to see if such symmetry will lead to other combinations of properties beyond valleytronics. Such discovery may also allow future work on practical applications with $\text{SnS}_x\text{Se}_{1-x}$ as a model system to be conducted.

Chapter Four

4. Engineering multi-digit devices based on valleytronics principles³

4.1. Device work and transport measurements of SnS

Beyond our discovery of the valleytronics effect, SnS is a material system widely researched for thin film applications in photovoltaics [77] due to its large absorption coefficient [78]. As such, there has been a substantial number of device work that investigates the electronic properties of SnS, specifically pertaining to its use as an absorber layer [77] [79]. These publications provided a vast amount of information on the key material properties of SnS, such as mobility, albeit having a wide range of values that is dependent on sample quality and morphology [56] [80] [81] [82].

4.2. Reading valley polarization via optoelectronic means

4.2.1. Utilization of light-matter interaction for anisotropic transport properties

As an information storage and processing tool, developments in SnS valleytronics [8] [9] and valleytronics in general are currently limited by the ease of generating selective valley polarization and then the subsequent reading of the polarized states. Optical methods presented in the previous chapters only reveal the presence of light-matter interaction and the potential of storing information. To fully utilize the valleytronic effect, there is a need to devise some form of read-out method. An optoelectronic device will serve the above-mentioned purpose.

Recent focus on the anisotropy of layered materials have led to an increase in publications that utilize the difference in effective mobilities [82] [83] [84] and dielectric constants and thus absorption coefficient [85] along armchair and zigzag in demonstrations of polarization dependent photodetectors. However, such measurements are based on simple absorption differences and the applicability of such devices hinges upon external parameters such as thickness [86]; fidelity can be easily compromised. There has not been any incorporation of valley properties in an optoelectronic device.

This chapter reports the first demonstration of the inclusion of valleytronics capabilities in an optoelectronic device via a simple photodetector device. Our device design allows the observation of multiple states that corresponds to distinct photocurrent (I_p) responses, with each state generated optically and detected electrically by a different configuration

³ Reproduced in part with permission from [10].

comprising a combination of excitation energy, excitation polarization, and detection direction. This practical multi-digit optoelectronic device is based solely on fundamental valleytronics principles. Further, using the same device design, we revealed fundamental mechanisms that contribute to I_p via optoelectronic measurements, allowing an understanding of the potential and limitations of implementing this valleytronic system.

4.2.2. Experimental setup

Figure 30 shows the schematic of the experimental setup, which is essentially a standard anisotropic photodetector device. SnS microplates were mechanically exfoliated on a Si/SiO₂ substrate and electron-beam deposition was used to deposit two pairs of electrodes along the major (armchair and zigzag) axes of the sample. 10nm of Palladium (Pd) was first deposited as the adhesion layer, followed up 100nm of Au.

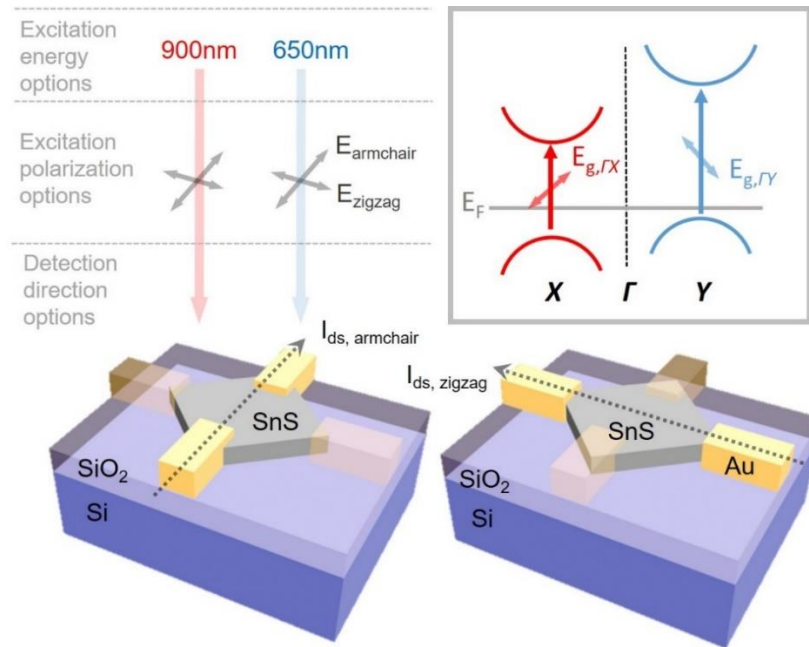


Figure 30: Schematic of the anisotropic photocurrent device measured in this work. Three levels of control of the multi-digit switch is envisioned, via (i) the excitation energy (shown to be 650nm and 900nm which corresponds to the above- and between-bandgaps wavelengths respectively), (ii) the excitation polarization (shown to be along either armchair or zigzag to selectively excite the ΓY and ΓX valleys respectively), and (iii) the current detection. Inset is the schematic bandstructure that shows the valley optical selection rules.

4.2.3. Design of multi-digit device

Optoelectronic measurements were conducted with three levels of control, via: (i) the anisotropic transport properties of SnS and the valleytronic capabilities of SnS (inset of Figure 30), namely (ii) perpendicular excitation polarizations and (iii) non-degenerate

excitation wavelengths, since the excitation of charge carriers at the valleys are selective to both excitation polarization and energy.

Figure 31 shows a schematic of the Tauc plot of SnS microplates, as adopted from [8], overlaid with five separate bands that differ in energy values, 1300nm, 1090nm, 900nm, 840nm, and 650nm, to illustrate the chosen excitation wavelength ranges for our measurements. Because the difference in the onset of absorption, as shown in the absorption spectra, is a manifestation of the valleytronic effect, different excitation wavelengths thus allow different population regimes in the valley structure to be probed. The chosen wavelength ranges allow the demonstration of the relationship between the valleytronic effect and photoresponse by probing the above- ($h\nu > E_{g,Zig}$), between- ($E_{g,Zig} > h\nu > E_{g,Arm}$), and below-bandgaps ($h\nu < E_{g,Arm}$) states of SnS.

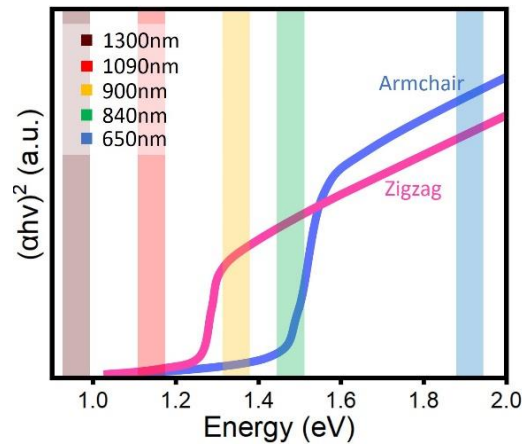


Figure 31: Semi-quantitative schematic of Tauc plots for SnS along armchair and zigzag directions overlaid with five bands that represent the five wavelength ranges that we employed in this work. The five wavelengths include 650nm ($h\nu > E_{g,Zig}$), 840nm and 900nm ($E_{g,Zig} > h\nu > E_{g,Arm}$), 1090nm ($E_{g,Arm} > h\nu > E_{absorption\ tail}$), and 1300nm ($h\nu < E_{absorption\ tail}$).

We define a naming convention for each of the optoelectronic configuration as $(I_{||})(\lambda)(E_{||})$ where $I_{||}$, the current direction with respect to the sample axes, takes “A” or “Z”, λ , the excitation wavelength, is expressed in nm, and $E_{||}$, the excitation polarization with respect to the sample axes, takes “Arm” or “Zig”. For example, the configuration under 900nm excitation along armchair axis and current detected along the zigzag direction is labelled as Z900Arm.

4.2.3. Basic material and device characterization

Figure 32a shows the optical microscope image of the device investigated in this work. Raman spectroscopy was used to verify that the directions of the deposited electrodes coincide with the main axes of the sample. Figure 32b shows the Raman spectra of the SnS

sample when the incident laser was polarized along each pair of electrodes, under both parallel and cross-polarization configurations, demonstrating key trends in the A_g and B_{3g} modes that represents the armchair (A) and zigzag (Z) directions [8].

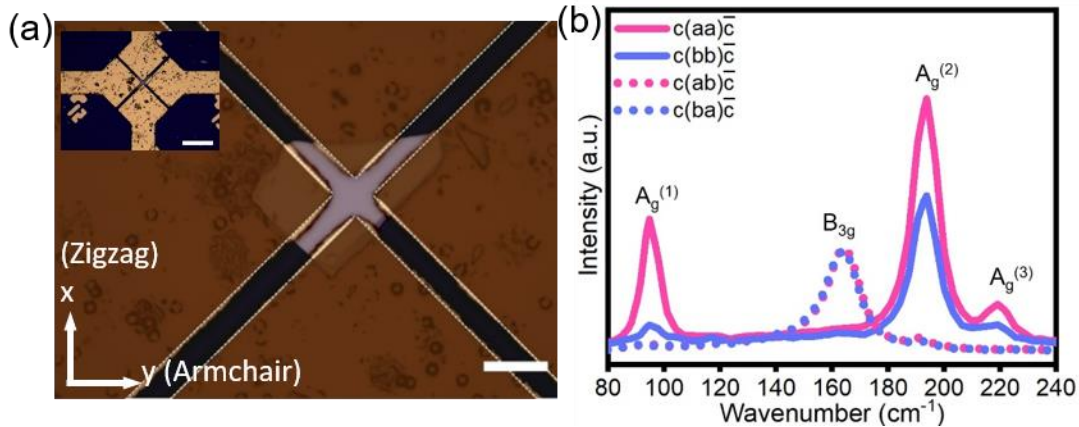


Figure 32: (a) Optical microscopy image of the device, showing that the electrodes are aligned along the armchair and zigzag directions of the SnS microplate respectively. Scale bar is $20\mu\text{m}$. Inset shows the zoomed-out view of the electrodes. Scale bar is $50\mu\text{m}$. (b) Reflection mode Raman spectra obtained along both electrode axes under parallel and cross polarizations. Trends in the Raman modes ascertain that the direction along the horizontal (vertical) direction of the image in (a) corresponds to the armchair (zigzag) direction of the SnS microplate and the spectra were labelled according to the axis directions. The first and second letters in the parentheses denotes the alignment of the incident light and emitted signal.

We further characterized the device with source-drain current versus source-drain voltage, $I_{ds}-V_{ds}$, measurements and show that the electrode contacts are Ohmic for both directions under dark (Figure 33a) and illuminated (Figure 33b) conditions. We standardised our subsequent source-drain current versus time, $I_{ds}-t$, and source-drain current versus temperature, $I_{ds}-T$, measurements to be conducted at $V_{ds}=3\text{V}$. The slightly larger I_{ds} values for the zigzag (Z) direction as compared with the armchair (A) direction, in agreement with previously reported values [84], also serves as a complementary evidence to the Raman results in Figure 32b.

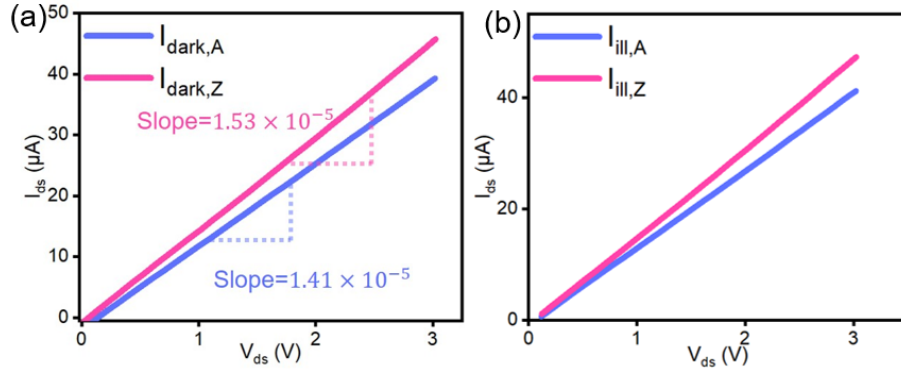


Figure 33: (a) I_{ds} - V_{ds} graphs of the device along armchair and zigzag directions. The straight lines denote that the device remains Ohmic with $V_{ds}=\pm 3V$. (b) I_{ill} were measured using 900nm illumination at the highest power setting of the light source without any polarizer. The linear trend of I_{ill} signifies Ohmic response of the device even under illumination.

4.2.3.1. Electric field distribution in SnS based on shape of electrodes

In deciding on our electrode design, we calculated the electric field distribution in the sample for various representative electrode shapes using COMSOL and presented them in Figure 34. Electrodes of the two extreme shapes for the front edge, (a) flat [56] and (b) pointed [85], were considered. The electrodes were designed to have the flat edges being $10\mu m$ apart to maximize coverage and to allow an economical choice of soft mask for photolithography. Dielectric constant of SnS was obtained from [87]. The model for the sample was designed to have dimensions of $50\mu m \times 50\mu m \times 500nm$ to best mimic that of the actual SnS microplate and the electrodes were subjected to $V_{ds}=3V$ to mimic that of actual experimental conditions.

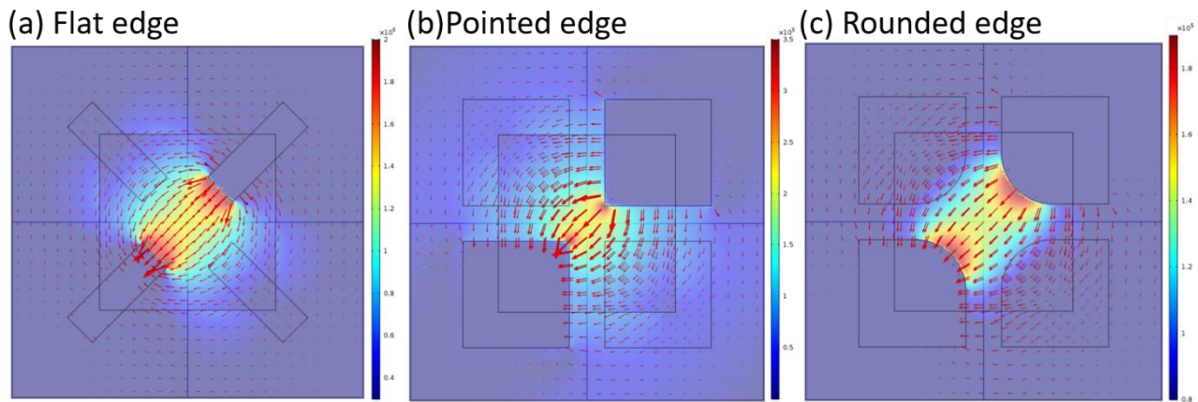


Figure 34: COMSOL simulations of electric field distributions for various electrode shapes. Three electrode structures were investigated: (a) flat edge, (b) pointed edge, and (c) rounded edge. The radius of curvature of the rounded edge structure was obtained from the actual deposited electrodes in our device.

Our results show that the flat edge electrode design, albeit having substantial electric field components along the electrode central axis, has an electric field distribution that extends further away from the central axis compared with the pointed edge design. We further performed a volume integration of the electric field in the whole sample and obtained the percentage of electric field along the electrode axis to be 67.3% and 70.3% for the flat and pointed edge designs respectively.

After choosing the slightly more ideal pointed edge design, which also maximizes the coverage of Au on the sample, imperfections in photolithography and electron beam deposition led to the edge to be (c) rounded. We obtained the radius of curvature from the actual electrode of our device (Figure 32a) and performed the same calculation and volume integration, obtaining an electric field distribution well-confined parallel to and near the central axis of the electrodes and the percentage of electric field along the electrode axis to be 76.2%, ascertaining the validity of our design for use in anisotropic transport measurements.

4.3. Multi-digit device based on valleytronics

4.3.1. General power-dependent photocurrent trends

Power dependence measurements were measured at room temperature via an on-off procedure where the initial I_{ds} was measured in the dark state, I_d , and every subsequent photocurrent under illumination, I_{ill} , was measured with a specific configuration of excitation wavelength and polarization. Figure 35 shows the $(I_{ds}-I_d)$ vs t graphs with sequentially increasing incident light intensity for Z900Zig and Z900Arm. We see from the graphs that $I_{p,Z900Zig} > I_{p,Z900Arm}$ for all excitation intensities, which is the key feature that corresponds to the fundamental valleytronics property of SnS.

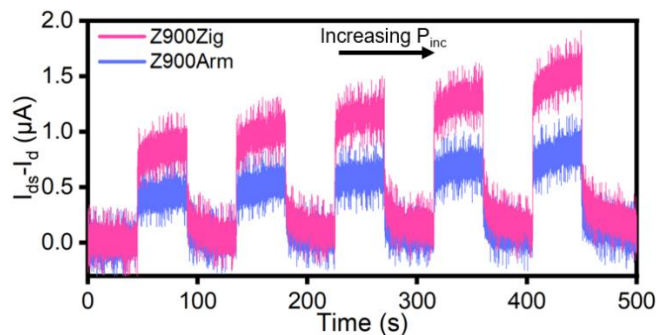


Figure 35: $I_{ds}-I_d$ versus t curve for Z900Zig and Z900Arm, performed with sequentially on-off procedure with five increasing excitation intensities. The $I-t$ relationships show clear biexponential trends upon excitation (rising curve) and deexcitation (decay curve). Valley selectivity is manifested in the distinct $I_{p,Z900Zig}-I_{p,Z900Arm}$ for all excitation intensities.

The I_p values for the all other configurations are consolidated and presented in Fig. 2b and Fig. 2c. We observe that $I_{p,A900Zig} > I_{p,A900Arm}$, which demonstrates that the valley selection rules for excitation is strictly optically dependent. For completeness of the investigation of band-to-band transitions at each valley, we also show the presence of selection rules for $h\nu > E_{g,Zig}$, presented as $I_{p,Z650Arm} > I_{p,Z650Zig}$ and $I_{p,A650Arm} > I_{p,A650Zig}$, which can be attributed to the larger absorption coefficient for light polarized along armchair (Arm) compared with zigzag (Zig) at 650nm or $h\nu > E_{g,Zig}$ in general [8].

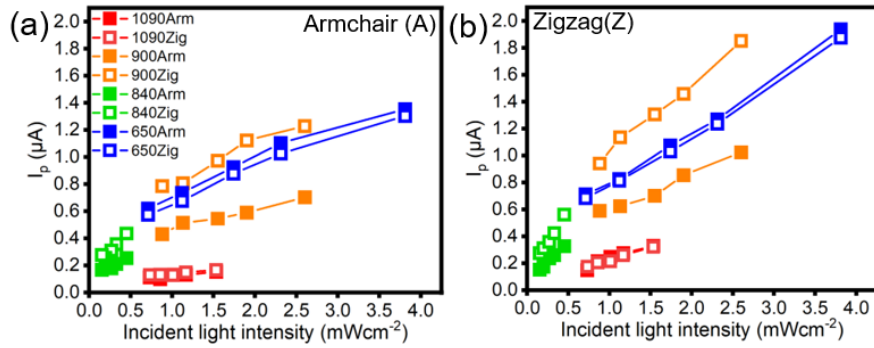


Figure 36: (a) I_p versus P_{inc} values for current detected along the armchair direction. Valley selectivity is clearly shown as $I_{p,A900Zig} > I_{p,A900Arm}$ and $I_{p,A840Zig} > I_{p,A840Arm}$. Anisotropic absorption is validated by $I_{p,A650Arm} > I_{p,A650Zig}$. Non-zero and similar $I_{p,A1090Arm}$ and $I_{p,A1090Zig}$ shows the presence of in-gap states. (b) I_p versus P_{inc} values for current detected along the zigzag direction, giving similar trends between excitation polarization directions. (a) and (b) gives multiple distinct I_p values at a constant P_{inc} for different configurations.

4.3.2. Biexponential, fast and slow switching times

From Figure 35, we observe that both rising and decay of I_{ds} upon excitation and removal of excitation (deexcitation), respectively, follow biexponential trends:

$$I_{ds} - I_d = I_{p,decay} + A_{fast} e^{-\frac{t-t_0}{\tau_{fast}}} + A_{slow} e^{-\frac{t-t_0}{\tau_{slow}}}$$

where t_0 offsets the curve to begin to rise at $t = 0$ s, A_{fast} and A_{slow} are coefficients with units of current, and τ_{fast} and τ_{slow} are the switching time values for the fast and slow components respectively. Figure 37 shows representative biexponential fittings of Z900Zig and Z900Arm at the highest power setting, where the two distinct time values can be observed. At room temperature, $\tau_{fast} \approx 70$ ms and $\tau_{slow} \approx 15$ s for all configurations (Figure 38). This signifies the presence of at least two separate mechanisms that contributes to I_p . I_{ds} -T measurements, were then conducted to reveal the nature of such mechanisms, presented in a later part of the chapter.

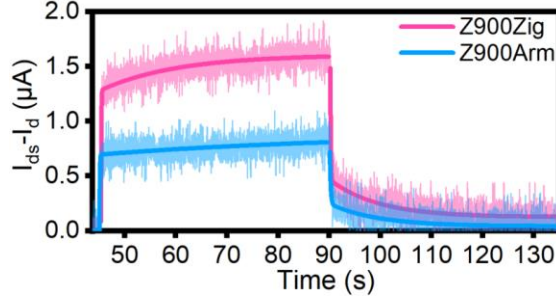


Figure 37: $I_{ds}-I_d$ versus t curves (lighter shades) for Z900Zig and Z900Arm at the highest power setting at room temperature were both fitted with biexponential trends (darker fits). Both rising and decay profiles fit well with the biexponential fits and they give two, fast and slow, distinct characteristic times.

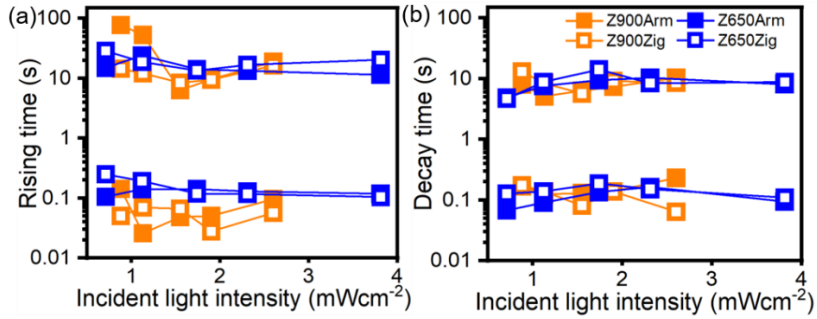


Figure 38: (a) Rising and (b) decay times for Z900Arm, Z900Zig, Z650Arm, and Z650Zig respectively, showing the presence of a slow and fast time and a general lack of dependence of switching time values on incident light intensities.

4.3.3. Identification of multiple states

Figure 36 show the I_p versus incident light intensity values of all photoresponse measurement configurations. Contrary to typical anisotropic photodetectors that give two different I_p values that corresponds to two states [85], our device can exist in at least eight different states at a fixed incident light intensity due to the valleytronic behavior as stipulated in Figure 30. This is the first demonstration of a practical valleytronics-driven multi-digit optoelectronic device.

I_p measurements performed using 1090nm excitation have substantial values without excitation polarization selectivity. This shows in-gap absorption and points towards the presence of in-gap defect states, which aligns with common understanding that SnS is generally p type doped with Sn vacancies, V_{Sn}^{2-} [88]. The involvement and effects of these states in the valleytronics behaviour of SnS will be further discussed later in this chapter. We note that this abovementioned I_p that result from in-gap absorption can provide two additional states for our device. I_p measurements performed using 1300nm excitation give no observable photoresponse, showing that in-gap absorption does not occur at $h\nu < 0.95\text{eV}$.

We consolidated the I_p values for the above-mentioned, proposed states that corresponds to the various configurations and present them as a histogram in Figure 39. The states are clearly discernible from each other. Note that these I_p values are normalized to a low incident light intensity of 1.5mWcm^{-2} and the states can become more distinct at larger intensities.

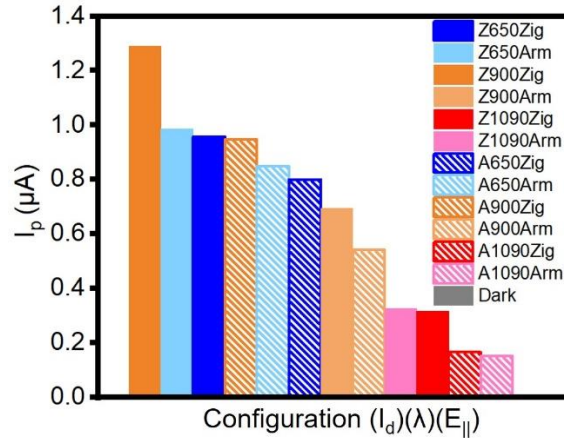


Figure 39: Histogram showing I_p of various configurations obtained from Figure 36 and normalized to an incident light intensity of 1.5mWcm^{-2} .

4.3.3.1. Signal to noise ratio

The robustness of the I_p signals as distinct states depends on the signal to noise, S/N , ratio. We calculated the noise of our signals by first finding the difference between the experimental data and the fitted biexponential curve for all data points, which can then be plotted as a histogram. Figure 40 shows the histogram obtained from a typical measurement of Z900Zig at the highest power setting at room temperature, which can be fitted using a Lorentzian distribution, giving a noise value of $\Gamma=4.12 \times 10^{-8}\text{A}$. Using $I_{p,Z900Zig} - I_{p,Z900Arm}$ as an example, we obtain ΔI_p to be $7.19 \times 10^{-7}\text{A}$. The S/N ratio of our device can thus be up to 17.5; the states can be distinctly identified.

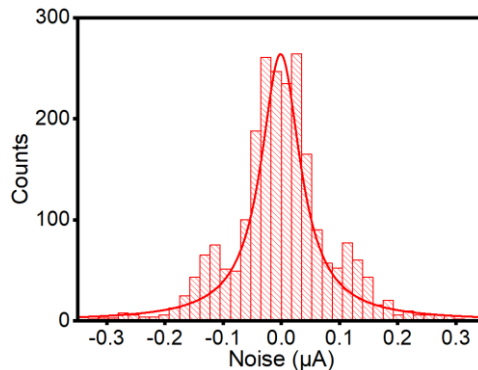


Figure 40; Histogram of noise. Difference in fitted exponential curves and experimental data was calculated for a representative Z900Zig rising curve at the highest power setting at room temperature. The resulting histogram presents a distribution of noise values, which can then be fitted with a Lorentz distribution to give the noise of our measurements.

4.3.3.2. Non-ideal manifestation of valley selectivity in photoresponse

While these measurements show distinct differences in I_p for different states, the selection rules are not ideally manifested. For example, $I_{p,900\text{Arm}}$ should be 0A according to symmetry since absorption should not occur for 900Arm [8]. Substantial values for $I_{p,900\text{Arm}}$ present a limitation to the practicality of the device by obscuring the distinction between the states that have been defined by each optoelectronic configuration described in Figure 30. This limitation can be partly attributed to defect states as observed with 1090nm excitation (Figure 36) and forms the other key factor to understanding the device apart from the trends in switching times.

As low temperature measurements were subsequently conducted for these analyses, I_p measurements with 840nm excitation were conducted to ensure that trends at low temperature are not due to the increase in bandgap values as temperature decreases [8]. Figure 36 shows that the photoresponse of 840nm and 900nm excitation aligned very well, ascertaining the validity of the measurements in the above-mentioned respect.

4.3.4. Key performance of device characterized as a photodetector

4.3.4.1. Responsivity

Analyses of key photodetector figures of merit under each configuration were carried out, further ascertaining the practicality of the device. Figure 41 shows the responsivity, R , of the device, defined as the photocurrent per incident unit optical power [89].

$$R = \frac{I_p}{P_{inc}A}$$

where P_{inc} is the incident light intensity and A is the active area denoted as the sample area not covered by the electrodes. R is large for all configurations and remains within the same order of magnitude at higher P_{inc} .

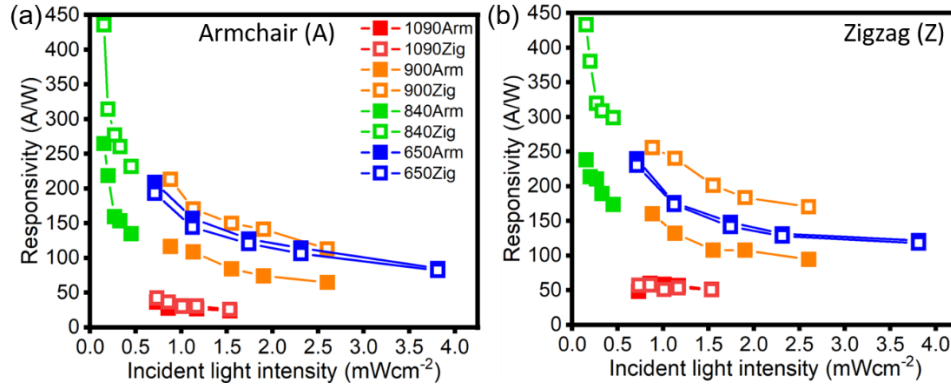


Figure 41: R versus incident light intensity for electrode direction along (a) armchair and (b) zigzag respectively.

Note that the use of this measured area as A will give an underestimate and thus lower bound of all calculated figures of merits since most of the carrier transport occurs in a narrow channel near the central axis of the electrodes, as shown in our COMSOL calculations (Figure 34).

Even with the lower bound estimation, we obtained R of up to $\sim 430 \text{ A/W}$ within the range of our incident light intensities, comparable to reported values [56] [80]. Large R values are important for optoelectronic switches as they ensure that light-matter interactions can be converted into electrical outputs with high fidelity.

4.3.4.2. Differential responsivity, ΔR

We demonstrate the superior anisotropy of our device by comparing the difference in responsivity of the material for incident excitation polarization along the two major directions, ΔR , as these two cases correspond to two distinct states in the devices. ΔR is a practical figure of merit that reflects the robustness of the material as a switch because it contains information on both photoresponse (implied in R) and anisotropy.

We calculated ΔR for reported work in black phosphorus [90], ReSe_2 [91], and GeAs_2 [92], as well as both valley-selective ($\lambda=840 \text{ nm}$ and $\lambda=900 \text{ nm}$) and non-valley-selective ($\lambda=650 \text{ nm}$) regimes of SnS in this work. Our comparison (Figure 42) shows ΔR of up to 195 A/W in our work in the valley-selective regime, which is ~ 21 times that of the non-valley-selective regime and at least two orders larger than that of other materials. This shows that ΔR is larger for our valleytronics-driven device as compared with other devices that have anisotropy simply driven by differences in absorption coefficients.

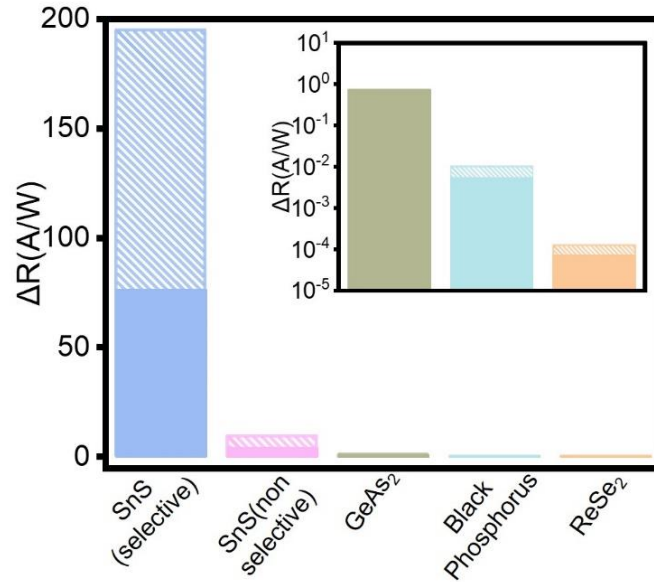


Figure 42: Summary of ΔR values for photoresponse of reported anisotropic materials, including black phosphorus, GeAs₂, and ReSe₂. ΔR of SnS in this work in the valley-selective regime is orders of magnitude larger than the reported materials and SnS in the non-valley-selective regime.

4.3.4.3. Specific detectivity

A figure of merit that is defined from the responsivity, R , is the specific detectivity, D^* , defined as detector output signal-to-noise ratio at 1 Watt of input radiation normalized to a detector with a unit active area and a unit bandwidth [93].

$$D^* = \frac{R\sqrt{A}}{\sqrt{2qI_d}}$$

where A is the active area, q is the elementary charge and I_d is the dark current. The calculated values are presented in Figure 43, giving D^* values that ranges from 4.87×10^{10} Jones to 2.53×10^{11} Jones, which is comparable to reported values of 3×10^9 Jones to 7.1×10^{11} Jones [80].

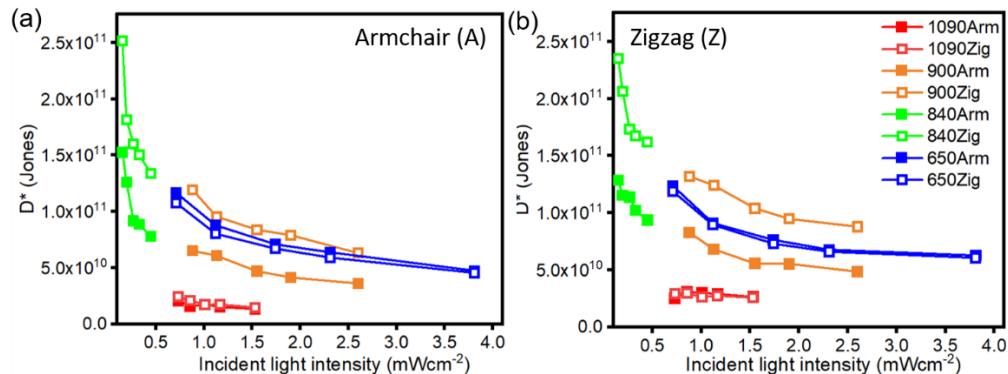


Figure 43: D^* versus incident light intensity for electrode direction along (a) armchair and (b) zigzag respectively.

4.3.4.4. External quantum efficiency, η

Akin to R , the external quantum efficiency, η , is the measure of ratio of number of charge carriers contributing to I_p to the number of incident photons of a given energy shone on the active area of the device [93]. We can obtain η from R using

$$\eta = R \frac{h\nu}{q}$$

where q is the elementary charge and $h\nu$ is the photon energy. The calculated values are presented in Figure 44, giving η values that ranges from $1.30 \times 10^{-40}\%$ to $6.44 \times 10^{-40}\%$, which are comparable to reported values of $1.3 \times 10^{-10}\%$ to $4.75 \times 10^{-50}\%$ [80].

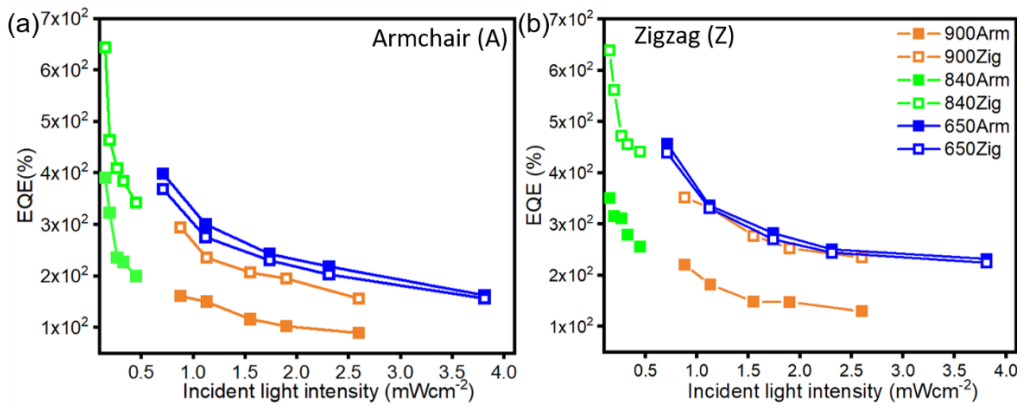


Figure 44: η versus incident light intensity for electrode direction along (a) armchair and (b) zigzag respectively.

4.3.4.5. Noise equivalent power, NEP

Another way to visualize the S/N ratio of an optoelectronic device is to use the reciprocal of D^* , given as the noise equivalent power, NEP. NEP is defined as the signal power that gives a S/N ratio of one in a one hertz output bandwidth [89].

$$NEP = \frac{\sqrt{A\Delta f}}{D^*} = \frac{i_{noise}}{R}$$

where A is the active area, D^* is the specific detectivity and Δf , the working frequency, is taken to be 1Hz by convention. The relationship between NEP and the root-mean-squared noise current, i_{noise} , is also given in the equation above, showing that the low NEP values signify low noise for our device. Calculated values of NEP are presented in Figure 45, giving

values that ranges from $5.64 \times 10^{-15} \text{WHz}^{-1/2}$ to $1.26 \times 10^{-15} \text{WHz}^{-1/2}$, which are comparable to reported values of $4.6 \times 10^{-12} \text{WHz}^{-1/2}$ to $1.8 \times 10^{-15} \text{WHz}^{-1/2}$ [94] [95].

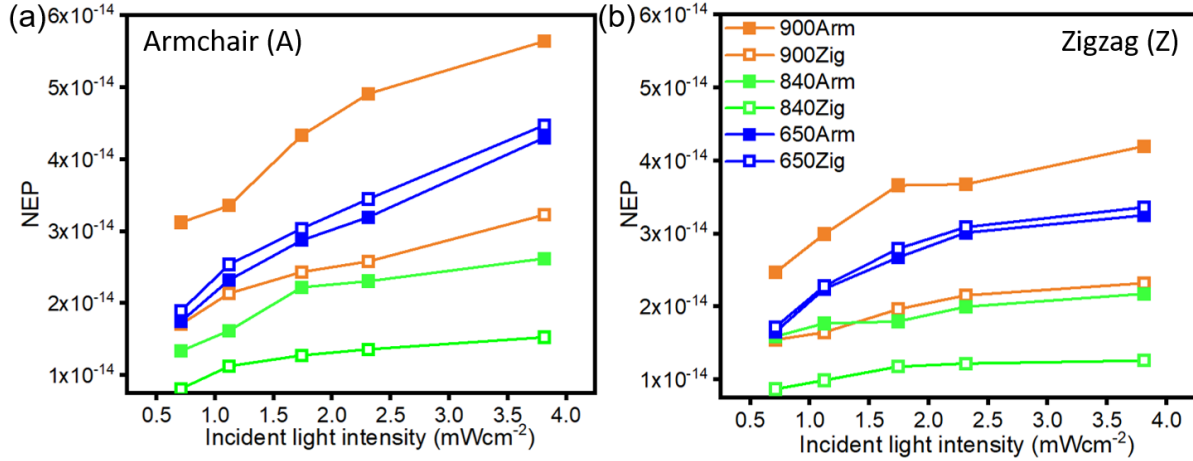


Figure 45: NEP versus incident light intensity for electrode direction along (a) armchair and (b) zigzag respectively.

4.3.5. Power-dependent I_p and relation to recombination mechanism

One way to quantify the sensitivity of photodetectors to illumination is via the exponential relationship between I_p and P_{inc} , given as $I_p \propto P_{inc}^\beta$, where the exponent $\frac{1}{3} < \beta < 1$. Greater β means greater sensitivity of I_p to P_{inc} . β values of 1, $\frac{1}{2}$, and $\frac{1}{3}$ represent ideally, unimolecular (charge carriers reside at and recombine at recombination states), bimolecular (band-to-band recombinations), and diffusion-limited recombination respectively [96]. We present the $\ln(I_p)$ versus $\ln(P_{inc})$ fits in Figure 46. β takes values from 0.42 to 0.72 for our device.

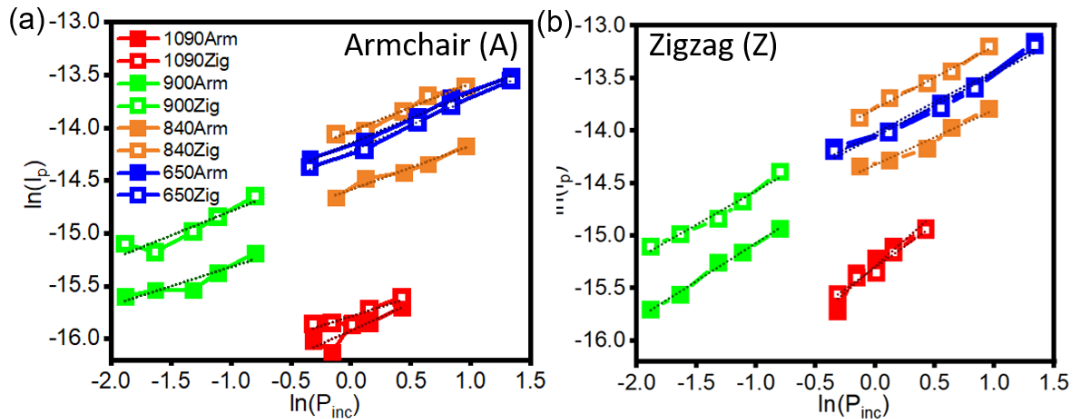


Figure 46: $\ln(I_p)$ versus $\ln(P_{inc})$ for electrode direction along (a) armchair and (b) zigzag respectively. The exponent $I_p \propto P_{inc}^\beta$ can be fitted from the slope of the graphs, giving values that ranges from 0.42 to 0.72.

SnS has a large absorption coefficient [78], which means that absorption near the surface will be significant for thick samples and diffusion-limited recombination will take place [96]. This explains for β values less than $\frac{1}{2}$, which is theoretically not allowed if recombination is strictly unimolecular or bimolecular. The measured β is much higher than $\frac{1}{3}$, which means that both unimolecular and bimolecular recombination occur in the device, signifying the significant presence of recombination states contributing to I_p . Note that for valley selectivity, a compromise on high sensitivity in favour of carriers residing in band edges have to be achieved.

4.4. Understanding fundamental mechanisms effecting photoresponse

4.4.1. Temperature-dependent I_p

As mentioned above, the two practical limitations of the multi-digit device are the lack of complete selectivity and presence of slow switching times. To understand the fundamental mechanisms governing such phenomena, we conducted temperature-dependent I_{ds-t} measurements and analysed the trends. Figure 47 shows a series of on-off measurements for Z900Zig and Z900Arm conducted at various temperatures, T , ranging from 80K to 300K at 20K intervals. We chose the largest setting used in Figure 35 for P_{inc} . The graphs are normalized by I_d and offset along the vertical axis with an equal magnitude for comparison of the absolute values of I_p .

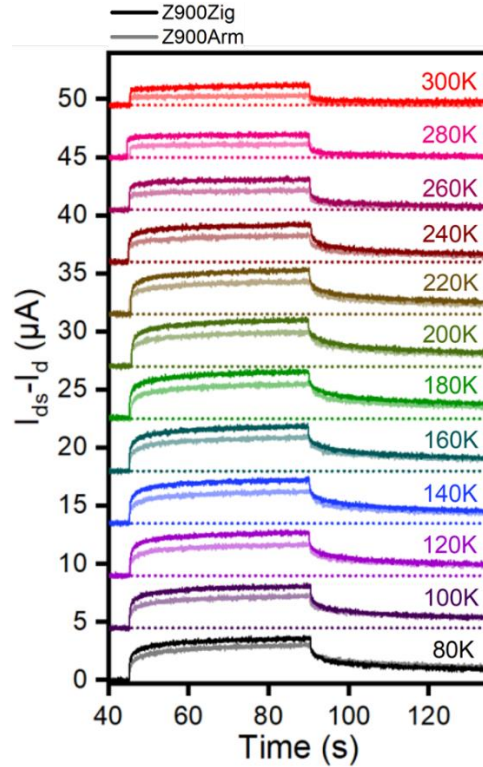


Figure 47: $I_{ds}-I_d$ versus t curves for Z900Zig and Z900Arm, performed with an on-off procedure at the highest excitation intensity of our light source. The same measurement was conducted from 80K to 300K at 20K intervals. Graphs are offset by a fixed magnitude.

4.4.1.1. Key temperature-dependent photoresponse features

Several key T-dependent photoresponse features can be observed from Figure 47.

First, I_p remains relatively constant across all T at low T for both Zig and Arm polarizations. However, beyond ~ 220 K, I_p begins to decrease with temperature for both polarizations.

Second, while I_p decreases for both directions, the difference in $I_{p,Z900Zig}$ and $I_{p,Z900Arm}$ remains relatively constant across all T. This leads to an increase in selectivity with T above ~ 220 K, as defined by $I_{p,Z900Zig}/I_{p,Z900Arm}$ (Figure 48a), from ~ 1.3 to ~ 2.0 . The relative lack of T dependence for $I_{p,Z900Zig}/I_{p,Z900Arm}$ at low T indicates the presence of a non-selective component of I_p that will be deactivated as T increases while the selective component remains relatively T-independent. We note that $I_{p,Z650Zig}/I_{p,Z650Arm}$ remains close to and slightly lower than 1 across all T and can be explained by the slight difference in absorption for Zig and Arm polarizations that can be observed from Figure 31.

Third, the fast rising (decay) processes show a sharp decrease in switching time with the increase of T beyond ~ 220 K, as evidenced by the more pronounced transition from the initial fast increase (decrease) in I_{ds} upon excitation (deexcitation). Figure 48b shows the quantitative trends of the switching times using Z900Zig as an example. It can be observed that while the τ_{slow} remains relatively constant across all T, τ_{fast} decreases from ~ 300 ms

below 220K to ~ 70 ms at 300K, which signifies that multiple I_p -contributing mechanisms make up the fast component.

For completeness, we show in Figure 48c that I_d has a slow increasing trend at low T and fast increasing trend at high T, which corresponds to common understanding of the transition from an extrinsic conduction regime to intrinsic conduction regime for a typical semiconductor [97]. It can also be observed that $I_{d,Z} > I_{d,A}$ for all T, showing that the difference in mobility remains similar across all T and should not be the primary reason for any feature observed in I_p when T is varied.

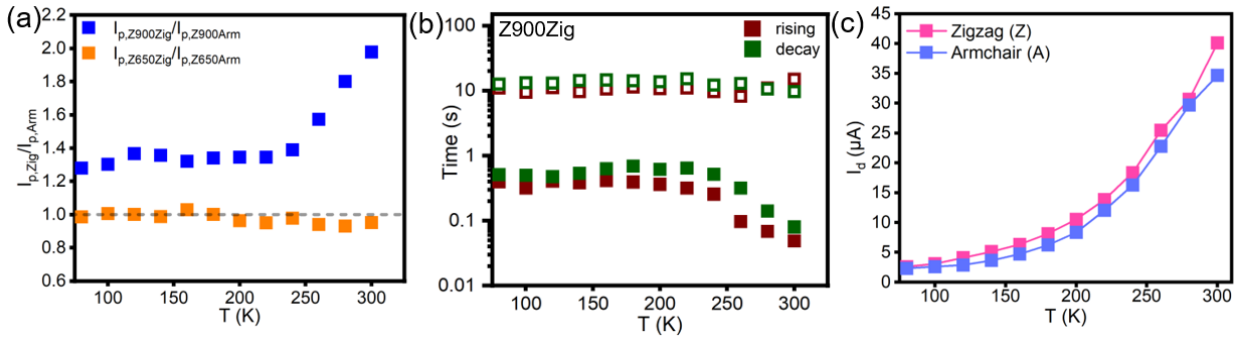


Figure 48: (a) $(I_{p,Zig}/I_{p,Arm})$ versus T results. $I_{p,Z900Zig}/I_{p,Z900Arm}$ stays relatively constant with a value of ~ 1.3 at low T and rises sharply at ~ 220 K to a value of ~ 2.0 at 300K. This increase in selectively can be attributed to the deactivation of a non-selective component with T above ~ 220 K. $I_{p,Z650Zig}/I_{p,Z650Arm}$ stays close to but slightly lower than 1 at all T, showing the difference in absorption coefficient along armchair and zigzag. (b) Switching time, τ , versus T, showing both fast and slow components of the biexponential fits for both rising and decay curves. The slow component has a relatively T-insensitive τ_{slow} at ~ 15 s. The fast component remains relatively constant at ~ 300 ms at low T but decreases beyond ~ 220 K to ~ 70 ms at 300K. (c) I_d -T results of the device measured along armchair and zigzag, showing that $I_{d,Z} > I_{d,A}$ for all T. I_d remains low at low T and increases sharply at high T, signifying the typical semiconductor behaviour that transitions from extrinsic to intrinsic conduction regimes as T increases.

4.4.2. Analysis of I_p -contributing mechanisms

To understand the contributing mechanisms of I_p , we analysed the T-dependence of respective components of the on-off curves for various configurations. Because τ_{slow} is much longer than τ_{fast} , the fast process dominates the initial photoresponse and the slow process dominates for the remaining time. We can therefore model the rising and decay curves to have a slow process that follows the fast process temporally.

Figure 49a shows the schematic of a typical on-off curve, where the I_p can be separately viewed from a perspective of a rising process and decay process:

$$I_p = I_{Rising,slow} + I_{Rising,fast} = I_{Decay,slow} + I_{Decay,fast} + I_{PPC}$$

where I_{PPC} is the persistent photocurrent that represents current in excess of I_d even after deexcitation.

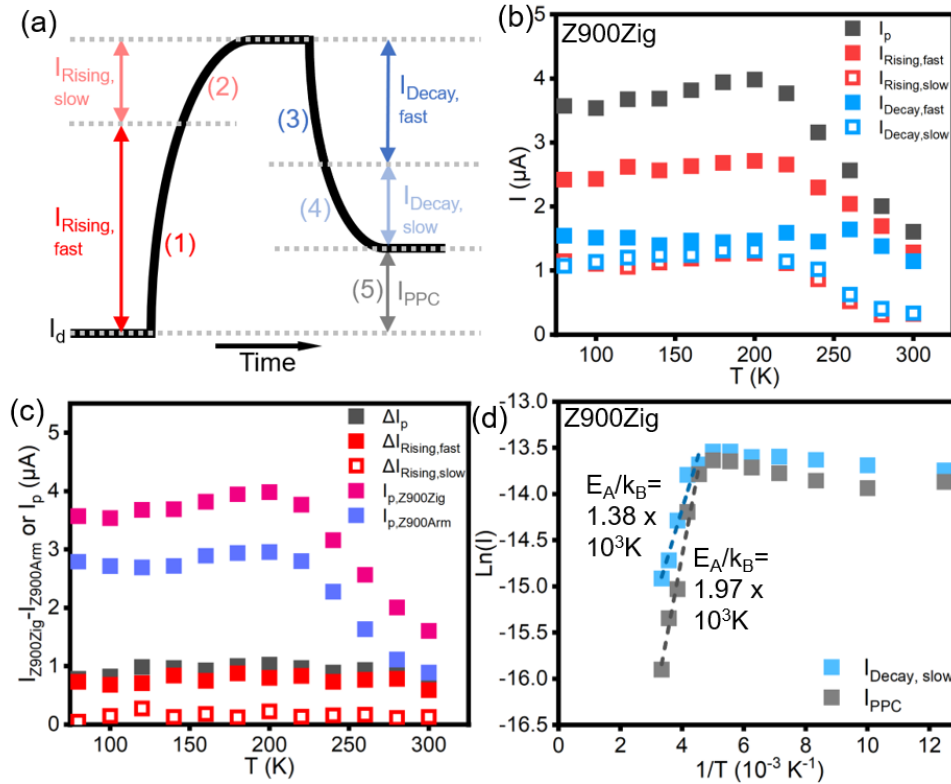


Figure 49: Analysis of current contributions and correlation to fundamental mechanisms related to recombination/ trap states. (a) Schematic of a typical on-off curve investigated in this work, plotted as $I_{ds}-I_d$ versus t . The photocurrent, I_p , can be viewed from the perspective of a rising curve or decay curve. This rising curve can be decomposed into a fast (1) component that is temporally followed by a slow (2) component. These two processes are characterized by currents, $I_{Rising,fast}$ and $I_{Rising,slow}$, and switching times, $\tau_{Rising,fast}$ and $\tau_{Rising,slow}$, respectively. The decay curve can also be decomposed into a fast (3) component that is temporally followed by a slow (4) component, but also possesses a persistent photocurrent, PPC, (5) component that gives a residual current greater than I_d . These three processes are characterized by currents, $I_{Decay,fast}$, $I_{Decay,slow}$, and I_{PPC} , and switching times, $\tau_{Decay,fast}$, $\tau_{Decay,slow}$ and τ_{PPC} , respectively. Note that τ_{PPC} is modelled as being infinitely large. (b) I - T measurements results for Z900Zig. $I_{Rising,slow}$ is almost identical to $I_{Decay,slow}$ (open squares), demonstrating that the slow components of the rising and decay curves are mirror and reverse process. I_p , $I_{Rising,fast}$ and $I_{Decay,fast}$ (solid squares) tend towards each other beyond $\sim 220K$, showing the diminishing slow process and PPC that can be attributed to deactivate of trap states. (c) I_p - T measurements results for Z900Zig and Z900Arm, showing similar trends of constant values at low T that decreases beyond $\sim 220K$. The difference, $\Delta I_p = I_{p,Z900Zig} - I_{p,Z900Arm}$ is also plotted, giving a constant value independent of T for all T , and can be almost fully attributed to $\Delta I_{Rising,fast}$. This means that the selective component of I_p is mostly due to the fast component. $\Delta I_{Rising,slow}$ is negligible for all T . (d) $\ln(I)$ versus $1/T$ for $I_{Decay,slow}$ and I_{PPC} . The slope of these two curves at T beyond $220K$ signifies the activation energy, E_A , of trap states based on an Arrhenius relationship.

Figure 49b shows the trends in I_p , $I_{Rising,slow}$, $I_{Rising,fast}$, $I_{Decay,slow}$, and $I_{Decay,fast}$ with T for Z900Zig. Z900Zig was chosen as the example here because of the large selective component in I_p , as shown previously in Figure 48b. As observed in Figure 47, I_p stays relatively constant with

the increase in T until $\sim 220\text{K}$ before it drops to less than half the initial value at 300K . Similar trends also occur for $I_{\text{Rising,slow}}$, $I_{\text{Rising,fast}}$, and $I_{\text{Decay,slow}}$.

4.4.2.1. Relating slow rising and decay times

Figure 49b shows that the values of $I_{\text{Rising,slow}}$ and $I_{\text{Decay,slow}}$ are almost identical for all T and therefore can be attributed to mirror and reverse processes. Further, as τ_{slow} remains relatively constant with T (Figure 48b), the slow component of I_p is likely to be contributed by a single mechanism. We thus attribute $I_{\text{Rising,slow}}$ ($I_{\text{Decay,slow}}$) to the interaction of “trap” states with the band edges to attain steady state upon the excitation (deexcitation) and formation of electron-hole pairs. This agrees with the observation (Figure 49a) that the slow processes occur temporally after the fast processes.

4.4.2.2. Relating fast rising and decay times

Because $I_{\text{Rising,slow}}$ and $I_{\text{Decay,slow}}$ are mirror processes, charge carrier generated via the fast rising process, $I_{\text{Rising,fast}}$, has to eventually contribute to $I_{\text{Decay,fast}}$ or remain as I_{PPC} . As mentioned, $I_{\text{Rising,fast}}$ is contributed by the electron-hole pairs generated via the absorption of photons upon excitation. Therefore, $I_{\text{Decay,fast}}$ can be attributed to the recombination of electron-hole pairs upon deexcitation. The presence of PPC means that some of the charge carriers are unable to recombine upon such deexcitation, presumably being trapped. Figure 49b shows that $I_{\text{Decay,fast}}$ approaches $I_{\text{Rising,fast}}$ at 300K . The diminishing PPC at higher T signifies the deactivation of charge carrier trapping at defect states. This can be attributed to the transition of these defect states from being recombination states (higher chance of recombination) to traps states (higher chance of thermal activation to band edges) at higher T [98], due to the shift in position of the quasi Fermi levels, E_F , away from the band edges [97].

4.4.2.3. Attributing switching times to fundamental mechanisms

Our analysis agrees well with mechanisms proposed by previous publications that observed biexponential rising and decay trends, where τ_{slow} and τ_{fast} are measured to be in the same order of magnitude as in this work [56] [80]. $I_{\text{Rising,fast}}$ and $I_{\text{Rising,slow}}$ are attributed to the photoconductive and photogating effects respectively [99]. The photoconductive effect is limited by the carrier transit time, which agrees with the hypothesis that the decreasing τ_{fast} with T is due to two different mechanisms. We attribute the faster mechanism of $I_{\text{Rising,fast}}$ to be carrier transit at the band edges while the slower mechanism to be carrier transit at recombination/ trap states which are deactivated at higher T . The photogating effect stipulate that carriers at such recombination/ trap states can act as local gating that generates opposite charge carriers very slowly to ensure electroneutrality. The fact that $I_{\text{Rising,slow}}$ and $I_{\text{Decay,slow}}$ decrease at high T while at a constant τ_{slow} further reinforces the notion that the slow process is triggered by the occupation of the recombination/ trap states.

4.4.2.4. Contributions of valley excitation to selectivity in I_p

Figure 49c shows that both $I_{p,Z900Zig}$ and $I_{p,Z900Arm}$ decrease sharply after $\sim 220K$, which signifies the loss of charge carriers that contributes to the photoresponse at the steady state of each T. This follows the general observed trend for other measured values in this work. However, the difference between $I_{p,Z900Zig}$ and $I_{p,Z900Arm}$, which is a measure of the selectivity of the system, remains constant with T. This means that the contributions to the valley-selective component of I_p is T-independent, which agrees with prior understanding that valleytronics-enabled phenomena in SnS is band-to-band symmetry-driven [8] and thus should not involve T-dependent interactions with trap states.

Figure 49c also shows that the difference in photocurrents for the two polarization configurations, $\Delta I_p = I_{p,Z900Zig} - I_{p,Z900Arm}$, is almost totally accounted for by the difference in the fast rising process, $\Delta I_{Rising,fast} = I_{Rising,fast,Z900Zig} - I_{Rising,fast,Z900Arm}$, while the difference in the slow rising process, $\Delta I_{Rising,slow} = I_{Rising,slow,Z900Zig} - I_{Rising,slow,Z900Arm}$, is almost negligible. This further substantiates the notion that the valley selective component, as manifested in ΔI_p , excludes contributions from trap states manifested in $\Delta I_{Rising,slow}$, and that the slow components, I_{slow} , has a lack of direct relationship with the excitation process.

The non-valley-selective components of $I_{Rising,fast}$ follows the trend of $I_{p,Z900Arm}$, of which the sharp decrease after $\sim 220K$ signifies the deactivation of the non-selective component. Charge carriers that contribute to $I_{Rising,fast}$ will subsequently either recombine, contributing to $I_{Decay,fast}$, or remain as I_{PPC} . While both $I_{Rising,fast}$ and $I_{Decay,fast}$ contains significant contributions by both selective and non-selective (non-band-to-band) contributions, the trend in I_{PPC} can be attributed totally to the non-selective trap states.

4.4.2.5. Quantifying trap states

Using the Arrhenius relationship, $I \propto e^{\frac{E_A}{k_B T}}$, we fitted the slopes of the $\ln(I)$ vs $1/T$ curves for $I_{Decay,slow}$ and I_{PPC} of Z900Zig for values above 220K, where conduction transits from an extrinsic to intrinsic regime and the effects of trap states start to have a T dependence, to estimate the activation energy, E_A , of the trap states (Figure 49d). We obtained E_A values of 0.12eV and 0.17eV respectively, which agrees with the typical calculated acceptor level above the ΓX valence band maximum, $E_{v,\Gamma X}$, of $\sim 0.21eV$ for p-type V_{Sn}^{2-} [8] [71] [88] and also ascertain the prior observation that in-gap absorption only occur at $h\nu > 0.95eV$.

Further, at the typical self-doped dopant concentration of $\sim 10^{15}cm^{-3}$ to $\sim 10^{18}cm^{-3}$ [88], $E_F - E_{v,\Gamma X}$ takes values of $\sim 0.25eV$ to $\sim 0.59eV$ at room temperature [71]. Since $E_F - E_{v,\Gamma X} \propto T$ [97], $E_F - E_{v,\Gamma X}$ reduces to $\sim 0.07eV$ to $\sim 0.16eV$ at 80K; E_F drops below that of the acceptor level with a decrease in temperature. This supports the observations in the fast rising and decay times analyses, as the acceptor states transitions from being recombination states to traps states at higher T.

4.5. Concluding remarks

In this chapter, we conducted optoelectronic measurements on SnS using a typical anisotropic photocurrent device and show that the photocurrent takes distinct values depending on the combination of excitation wavelength, excitation polarization, and current direction. This constitutes a multi-digit device based on the symmetry-dependent valleytronics principles of SnS as different excitation configurations selectively populate different valleys. We further elucidate the mechanisms that limit the performance of the device, namely the lack of complete selectivity of the photocurrent and the presence of slow switching times.

Such limitations arise due to the presence of defect states that can be attributed to the self-doping of V_{Sn}^{2-} . We envision that the reduction of these trap states via advancements in synthesis techniques will improve the device performance drastically in the following ways. First, the removal of the non-selective component for I_p will allow the realization of a true valleytronics switch, where the off state gives $I_p=0A$ and thus a practical on-off ratio. Second, both the removal of I_{slow} and trap state contributions to I_{fast} will greatly increase the switching time, τ . The remaining τ_{fast} will also be further improved since the carrier transit time will be much faster with less defects affecting the mean free path of the carriers. Third, with less defects, the reduction in I_d will indirectly lead to a higher on-off ratio, thus allowing smaller devices and lower incident intensities to be used. Note that a smaller device will also improve τ_{fast} via the reduction of total defect concentration.

Chapter Five

5. Outlook and future directions

5.1. Review of work in this thesis and limitations

This thesis focuses on the work done on IV-VI monochalcogenides, predominantly SnS, in its application as a novel valleytronic system.

5.1.1. Summary of Chapter 1

Chapter 1 reviewed the status of valleytronics in currently known materials and the vastly different origins of valleytronics effects. Subsequently, the limitations of such materials, mostly the stringent experimental conditions in generating valley polarization, are mentioned. We used those limitations as a starting point in our search for a novel valleytronic material.

5.1.2. Summary of Chapter 2

In Chapter 2, we identified the presence of a novel form of valleytronics that phenomenologically follows the general definition of valleytronics; we observed two distinct bandgaps in the reciprocal space of SnS that can be selectively populated. The fact that temperature, size, and external bias constraints are lifted for SnS valleytronics presents the potential for practical usage of the system. We provide experimental evidence of optical selection, proving the presence of light-matter interaction. Our theoretical efforts via group theory arguments also support this observation.

However, even as both our PVD and CVD methods yield plates that are thicker and wider than exfoliated ones, and that our optical result generally remain the same across synthesis methods, we still did not manage to control the size of the plates via growth parameter variations. The general spread of sizes from growth to growth remain similar as long as plates are grown and further tuning of growth parameters to more extreme conditions generally led to the deposition of SnS₂ and/ or Sn particles/ films. Because of this, thickness effects, surface effects, and edge effects, etc cannot be investigated.

We also encountered difficulty in exfoliating thin (less than a few layers) SnS pieces that are large enough for optical measurements. This also forms part of the motivation of our parametric study. However, this bid was also unsuccessful.

5.1.3. Summary of Chapter 3

In Chapter 3, we generalized our novel valleytronics and show that because the effect is purely symmetry dependent, it remains robust across both SnS and SnSe, and varies continuously across all intermediate alloy compounds, $\text{SnS}_x\text{Se}_{1-x}$. In our alloy studies, we utilized similar optical methods as presented in Chapter 2 and explained such retention of valleytronics using theoretical means. The more specific calculations presented this time round clearly identified and separated orbital contributions to the CB and VB of both valleys, showing that the orbital contributions and symmetry remains the same across all alloy compositions. Simultaneous tunability of band gap values with retention of valley behaviour was also shown to be possible because of varying contributions from the hybridised 4p and 3p bands of Se and S respectively.

However, attempts to synthesize other IV-VI alloy compounds were unsuccessful, further reinforcing the need for more precise growth methods that are applicable to other materials. This will not only broaden the tunability regime of IV-VI materials, but also enhance the completeness of our claim that such valleytronics can be generalized. Further, it will be interesting to find out if there is any interesting behaviour when the alloys containing Ge transitions from a two-valley bandstructure to a single global band gap in the Γ point. We foresee that the transitions will be continuous, since we expect to have the hybridization of Ge and Sn p orbital bands. However, the valleytronic behaviour when such transitions occur remains to be investigated.

5.1.4. Summary of Chapter 4

Chapter 4 talks about the application of SnS in an optoelectronic device based on valleytronics principles, effectively serving as a first demonstration of a true valleytronic device. Our optoelectronic device was fabricated in a simple photodetector configuration. With that, we varied our excitation wavelengths, excitation polarization and current flow direction to generate a series of combinations that gives distinct photocurrent response. This presents a straightforward way to utilize our non-degenerate valleys, which practically constitutes a multi-digit setup per device; this fulfils the aim of having complementary degrees of freedom. Analyses of the photocurrents under different configurations and the dependence on excitation intensity and temperature further revealed insights on the valleytronic transitions within SnS. We also set up defect models to explain such observations, giving a glimpse at the fundamental mechanisms of the electronic transitions at the valleys.

The completion of the device work opened more possibilities in using such valleytronics effect practically. However, for that to happen, materials improvements must be performed. One important aspect limiting the device in our proof of concept demonstration is the lack of perfect valleytronics selectivity and slow switching times, both attributed to defect states generated by self-doped V_{Sn}^{2+} . Materials improvements will aid in the progress of this direction.

Also, in terms of device structure, we know that the thickness of our bulk SnS is much larger than the maximum thickness where it still can be turned off as a field effect transistor [100], which limits its practicality. There are also various device structures or material systems that has yet to be explored.

In view of the abovementioned progress and limitations, we can further discuss the potential improvements in the material system and the field in general.

5.2. Potential improvements in synthesis

Our project is mainly focused on elucidating the valleytronics effect in SnS and, to a certain extent, $\text{SnS}_x\text{Se}_{1-x}$. With improvements in synthesis, several relevant materials can then be investigated.

5.2.1. Monolayer SnS and its advantageous attributes

The initial phase of this work is focused on the synthesis of bulk SnS. However, it is not a hard requirement that the bulk form of SnS is desired or even preferred. While bulk SnS has its merits in the relaxation of thickness requirements, monolayer SnS has the advantage of being much thinner, hence allowing improvements in device performances such as carrier transit time, ease of being turned off, and compactness.

That aside, monolayer SnS, while theoretically will retain the valleytronic properties [29], has various other properties not present in the bulk or any other thicknesses. For example, orthorhombic SnS, or IV-VI monochalcogenides in general, are predicted to have in-plane ferroelectricity due to the anharmonicity of atomic positions and thus ionic potential leading to spontaneous electric polarization [101] [102]. This is effectively a form of multiferroics, since the valleytronic properties of SnS can be considered as a tunable polarization termed ferrovalley [103].

The perquisite of ferroelectricity that is absent in bulk SnS is the absence of inversion symmetry. However, it has been proposed that if alternate layers in SnS can be flipped, inversion symmetry will be broken, and the interlayer coupling will transit from being antiferroelectric to ferroelectric [102]. This extension of properties that used to strictly require monolayer into the bulk regime can potentially greatly increase the flexibility of sample size requirements. Note that while there are also various known metastable phases of Sn and S [36], these phases do not possess valleytronics properties and should not be considered for our purpose.

5.2.2. Synthesis of other members of IV-VI monochalcogenides

Due to our limited understanding of the PVD and CVD growth processes as well as the lack of access to more sophisticated growth equipment that specializes in IV-VI

monochalcogenides synthesis, we are only able to grow SnS, SnSe, and the intermediate alloys. There are still many synthesis techniques left to be explored. Two main directions can be pursued: (i) synthesis of bulk crystals for exfoliation (assuming slight variations in sample quality greatly affects the ease of exfoliation) and (ii) modifications of techniques commonly used to grow films and/ or nanostructures (to bypass the large sensitivity of PVD or CVD techniques to the pressure of precursors).

There is an abundance of literature detailing the synthesis of different morphologies of IV-VI monochalcogenides. Interested readers are referred to the introductions of [36] and [104], where they summarise the methods for SnS synthesis.

5.3. Identification of symmetry-driven valleytronics in other material systems

5.3.1. Truly multifunctional material systems

Since valleytronics in SnS is purely symmetry-dependent, it is not hard to imagine that any material that has similar symmetry can theoretically possess valleytronics. The two criteria for valleytronics are then the presence of anisotropy and CBM-VBM pairs at more than one \mathbf{k} point. Searching for other valleytronic materials is important for the following reasons.

First, the combination of valleytronics properties and other properties will elevate the status of the material to that of a multifunctional system. While valleytronics is primarily envisioned as an information storage method, specific applications may have more stringent requirements, such as temperature resistance or high strength. Niche applications can benefit from such multifunctional materials.

Second, much like III-V semiconductors, there is a limit to the tunability of a certain family of materials in terms of wavelength ranges. Expanding the bandgap values to non-visible regimes will be greatly increase the applicability of such valleytronics.

5.4. Revealing fundamental valleytronics mechanisms in SnS

Our device work has revealed fundamental mechanisms governing the photoresponse of the material and points towards possible routes to performance improvements via improvements in material's quality. When that happens, the device performance will be limited by mechanisms governing the light-matter interaction aspect. One way to reveal such mechanisms is thus to elucidate key aspects of valley dynamics and depolarization in the system [105]. Ultrafast optical measurement techniques [106] can be used to obtain various lifetime values corresponding to the processes.

The correlation between the degree of polarization and lifetime values is [107]

$$P = \frac{P_0}{1 + \frac{\tau}{\tau_s}}$$

where P_0 is the initially created polarization, τ is the electron-hole pair/ recombination lifetime and τ_s is the polarization decay/ scattering time. By obtaining estimates of the lifetimes, we will be able to correlate the time-integrated P values with the maximum/ initially created P_0 values. This allows us to see if the system is robust at the point of excitation/ polarization. From the equation, we can also see that we want the recombination lifetime to be much smaller than the polarization decay time so that we can leverage on the valley selectivity. The experiments that will be performed are as such (Note that for non-degenerate valleys, anisotropic polarization decays may occur, which means the lifetimes for different excitations may differ greatly, making the system more interesting):

5.4.1. Time-resolved PL (TRPL) measurements

Using a pulsed laser with pico/ femtosecond pump pulses, the samples can be excited and the variation of PL intensity with time can be detected by coupling the spectrometer with a streak camera with picosecond resolution [105] [107]. Since the repetition rate of the pump pulses is in the range of tens of nanoseconds, the PL intensity obtained within the next hundreds of picoseconds will be due to recombination of carriers excited by only one pulse. Thus, the decay in PL intensity can be observed clearly. The decay trend will then be fitted with multi-exponential fits to obtain lifetime values, which are measures of scattering or recombination times. As a general rule, the fast decay processes are usually attributed to radiative recombination while the slow decay processes are generally attributed to remnant recombination from scattered carriers. For SnS, different linearly polarization excitations will allow the excitation and probing of both valleys separately. Probing both PL peaks' decays under parallel and cross polarization will also allow lifetimes for the same and different valleys as compared to the excitation polarization to be obtained and thus correlated to the inter and intravalley degrees of polarization.

5.4.2. Transient absorption (TA) measurements

While TRPL generally gives recombination lifetimes, linearly polarized transient absorption gives measures of intervalley scattering [108]. Using a pump-probe setup, the sample can be excited using a linearly polarized femtosecond pump pulse aligned to one of the main axes. White light probe pulses with the same repetition rate can then be shone on the sample. The reflection signal of the white light pulse can then be collected with CCD detection that is synced to the probe pulse. Since the initial laser pulse selectively excites a valley, the white light pulse can be polarized in the same (SP) or perpendicular (PP) direction to probe the same valley or different valley. With spectra taken at various pump-probe decay time, the evolution of the absorption profiles for both valleys can be seen. The evolution of features in the absorption profiles can be used to probe the carrier dynamics and varying the excitation

wavelength can elucidate effects of the band structure due to excitation, especially the difference between on and off-resonance excitation.

References

- [1] J. R. Schaibley, H. Yu, G. Clark, P. Rivera, J. S. Ross, K. L. Seyler, W. Yao and X. Xu, "Valleytronics in 2D materials," *Nature Reviews Materials*, vol. 1, p. 16055, 2016.
- [2] X. Xu, W. Yao, D. Xiao and T. F. Heinz, "Spin and pseudospins in layered transition metal dichalcogenides," *Nature Physics*, vol. 10, pp. 343-350, 2014.
- [3] L. J. Sham, S. J. A. Jr., A. Kamgar and D. C. Tsui, "Valley-Valley Splitting in Inversion Layers on a High-Index Surface of Silicon," *Physical Review Letters*, vol. 40, no. 472, 1978.
- [4] K. Takashina, Y. Ono, A. Fujiwara, Y. Takahashi and Y. Hirayama, "Valley Polarization in Si(100) at Zero Magnetic Field," *Physical Review Letters*, vol. 96, no. 236801, 2006.
- [5] O. Gunawan, Y. P. Shkolnikov, K. Vakili, T. Gokmen, E. P. D. Poortere and M. Shayegan, "Valley Susceptibility of an Interacting Two-Dimensional Electron System," *Physical Review Letters*, vol. 97, no. 186404, 2006.
- [6] Y. P. Shkolnikov, E. P. D. Poortere, E. Tutuc and M. Shayegan, "Valley Splitting of AlAs Two-Dimensional Electrons in a Perpendicular Magnetic Field," *Physical Review Letters*, vol. 89, no. 22, 2002.
- [7] J. Isberg, M. Gabrysch, J. Hammersberg, S. Majdi, K. K. Kovi and D. J. Twitchen, "Generation, transport and detection of valley-polarized electrons in diamond," *Nature Materials*, vol. 12, pp. 760-764, 2013.
- [8] S. Lin, A. Carvalho, S. Yan, R. Li, S. Kim, A. Rodin, L. Carvalho, E. M. Chan, X. Wang, A. H. C. Neto and J. Yao, "Accessing Valley Degree of Freedom in Bulk Tin(II) Sulfide at Room Temperature," *Nature communications*, vol. 9, no. 1455, 2018.
- [9] S. Lin, Z. Fang, T. Hou, T. W. Hsu, C. H. So, C. Yeoh, R. Li, Y. Liu, E. M. Chan, Y.-L. Chueh, B. Tang, K. Persson and J. Yao, "Continuously tunable valleytronics with symmetry-retaining high polarization degree in SnS_xSe_{1-x} model system," *submitted*, 2019.
- [10] S. Lin, T. W. Hsu, S. Lou, Y.-L. Chueh and J. Yao, "Multi-bit Tin(II) Sulfide optoelectronic device based on fundamental valleytronics principles," *submitted*, 2019.
- [11] W.-T. Hsu, Y.-L. Chen, C.-H. Chen, P.-S. Liu, T.-H. Hou, L.-J. Li and W.-H. Chang, "Optically initialized robust valley-polarized holes in monolayer WSe₂," *Nature Communications*, vol. 6, pp. 1-7, 2015.

- [12] K. F. Mak, K. He, J. Shan and T. F. Heinz, "Control of valley polarization in monolayer MoS₂ by optical helicity," *Nature Nanotechnology*, vol. 7, pp. 494-498, 2012.
- [13] D. Xiao, G.-B. Liu, W. Feng, X. Xu and W. Yao, "Coupled Spin and Valley Physics in Monolayers of MoS₂ and Other Group-VI Dichalcogenides," *Physical Review Letters*, vol. 108, p. 196802, 2012.
- [14] H. Zeng, J. Dai, W. Yao, D. Xiao and X. Cui, "Valley polarization in MoS₂ monolayers by optical pumping," *Nature Nanotechnology*, vol. 7, pp. 490-493, 2012.
- [15] D. Vanderbilt, Physics 682 textbook, Spring 2016, New Brunswick: Rutgers University, 2016.
- [16] K. F. Mak, K. L. McGill, Park and P. L. McEuen, "The valley Hall effect in MoS₂ transistors," *Science*, vol. 344, no. 6191, pp. 1489-1492, 2014.
- [17] W. Yao, D. Xiao and Q. Niu, "Valley-dependent optoelectronics from inversion symmetry breaking," *Physical Review B*, vol. 77, p. 235406, 2008.
- [18] G. Moody, J. Schaible and X. Xu, "Exciton dynamics in monolayer transition metal dichalcogenides," *Journal of the Optical Society of America B*, vol. 33, no. 7, pp. 39-49, 2016.
- [19] Y. Li, J. Ludwig, T. Low, A. Chernikov, X. Cui, G. Arefe, Y. D. Kim, A. M. v. d. Zande, A. Rigosi, H. M. Hill, S. H. Kim, J. Hone, Z. Li, D. Smirnov and T. F. Heinz, "Valley Splitting and Polarization by the Zeeman Effect in Monolayer MoSe₂," *Physical Review Letters*, vol. 113, p. 266804, 2014.
- [20] A. Castellanos-Gomez, L. Vicarelli, E. Prada, J. O. Island, K. L. Narasimha-Acharya, S. I. Blanter, D. J. Groenendijk, M. Buscema, G. A. Steele, J. V. Alvarez, H. W. Zandbergen, J. J. Palacios and H. S. J. v. d. Zant, "Isolation and characterization of few-layer black phosphorus," *2D Materials*, vol. 1, p. 025001, 2014.
- [21] T. Li and G. Galli, "Electronic Properties of MoS₂ Nanoparticles," *Journal of Physical Chemistry C*, vol. 111, pp. 16192-16196, 2007.
- [22] "Periodic Table of Elements," International Union of Pure and Applied Chemistry, 1 December 2018. [Online]. Available: <https://iupac.org/what-we-do/periodic-table-of-elements/>. [Accessed 28 March 2019].
- [23] L. C. Gomes and A. Carvalho, "Phosphorene analogues: Isoelectronic two-dimensional group-IV monochalcogenides with orthorhombic structure," *Physical Review B*, vol. 92, no. 085406, 2015.

- [24] W. Setyawan and S. Curtarolo, "High-throughput electronic band structure calculations: Challenges and tools," *Computational Materials Science*, vol. 49, no. 2, pp. 299-312, 2010.
- [25] P. Giannozzi, S. Baroni, N. Bonini, M. Calandra, R. Car, C. Cavazzoni, D. Ceresoli, G. L. Chiarotti, M. Cococcioni, I. Dabo, A. D. Corso, S. d. Gironcoli, S. Fabris, G. Fratesi, R. Gebauer, U. Gerstmann, C. Gougoussis, A. Kokalj, L. Michele, L. Martin-Samos, N. Marzari, F. Mauri, R. Mazzarello, S. Paolini, A. Pasquarello, L. Paulatto, C. Sbraccia, S. Scandolo, G. Sclauzero, A. P. Seitsonen, A. Smogunov, P. Umari and R. M. Wentzcovitch, "Journal of Physics: Condensed Matter," *QUANTUM ESPRESSO: a modular and open-source software project for quantum simulations of materials*, vol. 21, no. 39, 2009.
- [26] N. Troullier and J. L. Martins, "Efficient pseudopotentials for plane-wave calculations," *Physical Review B*, vol. 43, no. 3, p. 1993, 1991.
- [27] J. P. Perdew, K. Burke and M. Ernzerhof, "Generalized Gradient Approximation Made Simple," *Physical Review Letters*, vol. 78, no. 18, p. 3865, 1997.
- [28] M. S. Dresselhaus, G. Dresselhaus and A. Jorio, *Group Theory: Application to the Physics of Condensed Matter*, Berlin: Springer, 2008.
- [29] A. S. Rodin, L. C. Gomes, A. Carvalho and A. H. C. Neto, "Valley physics in tin (II) sulfide," *Physical Review B*, vol. 93, no. 045431, pp. 1-5, 2016.
- [30] A. Gelessus, "Character table for point group C3h," 23 May 2018. [Online]. Available: <http://symmetry.jacobs-university.de/cgi-bin/group.cgi?group=503&option=4>. [Accessed 29 March 2019].
- [31] G. F. Koster, *Properties of the thirty-two point groups*, Cambridge: M.I.T. Press, 1963.
- [32] G. Wang, C. Robert, M. M. Glazov, F. Cadiz, E. Courtade, T. Amand, D. Lagarde, T. Taniguchi, K. Watanabe, B. Urbaszek and X. Marie, "In-Plane Propagation of Light in Transition Metal Dichalcogenide Monolayers: Optical Selection Rules," *Physical Review Letters*, vol. 119, p. 047401, 2017.
- [33] Z. Mutlu, R. J. Wu, D. Wickramaratne, S. Shahrezaei, C. Liu, S. Temiz, A. Patalano, M. Ozkan, R. K. Lake, K. A. Mkhoyan and C. S. Ozkan, "Phase Engineering of 2D Tin Sulfides," *Small*, vol. 12, no. 22, pp. 2998-3004, 2016.
- [34] J. Xia, X.-Z. Li, X. Huang, N. Mao, D.-D. Zhu, L. Wang, H. Xu and X.-M. Meng, "Physical vapor deposition synthesis of two-dimensional orthorhombic SnS flakes with strong

- angle/temperature-dependent Raman responses," *Nanoscale*, vol. 8, pp. 2063-2070, 2016.
- [35] R. B. Darling, "EE-527: MicroFabrication Physical Vapor Deposition," [Online]. Available: <http://mmrc.caltech.edu/PVD/manuals/PhysicalVaporDeposition.pdf>. [Accessed 29 March 2019].
- [36] L. A. Burton and A. Walsh, "Phase Stability of the Earth-Abundant Tin Sulfides SnS, SnS₂, and Sn₂S₃," *The Journal of Physical Chemistry C*, vol. 116, no. 45, p. 24262–24267, 2012.
- [37] V. Piacente, S. Foglia and P. Scardala, "Sublimation study of the tin sulphides SnS₂, Sn₂S₃ and SnS," *Journal of Alloys and Compounds*, vol. 177, pp. 17-30, 1991.
- [38] R. Li, "MSE Masters degree Project Report," Berkeley, 2017.
- [39] J. R. Brent, D. J. Lewis, T. Lorenz, E. A. Lewis, N. Savjani, S. J. Haigh, G. Seifert, B. Derby and P. O'Brien, "Tin(II) Sulfide (SnS) Nanosheets by Liquid-Phase Exfoliation of Herzenbergite: IV–VI Main Group Two-Dimensional Atomic Crystals," *Journal of the American Chemical Society*, vol. 137, no. 39, pp. 12689-12696, 2015.
- [40] M. Wortis, "Chemistry and Physics of Solid Surfaces VII," in *Equilibrium Crystal Shapes and Interfacial Phase Transitions*, Berlin, Springer, 1988, pp. 367-405.
- [41] X. Xu, Q. Song, H. Wang, P. Li, K. Zhang, Y. Wang, K. Yuan, Z. Yang, Y. Ye and L. Dai, "In-Plane Anisotropies of Polarized Raman Response and Electrical Conductivity in Layered Tin Selenide," *ACS Appl. Mater. Interfaces*, vol. 9, no. 14, p. 12601–12607, 2017.
- [42] I. H. Malitson, "Interspecimen Comparison of the Refractive Index of Fused Silica," *Journal of the Optical Society of America*, vol. 55, no. 10, pp. 1205-1209, 1965.
- [43] P. B. Johnson and R. W. Christy, "Optical Constants of the Noble Metals," *Physical Review B*, vol. 6, no. 12, p. 4370, 1972.
- [44] A. Perot and C. Fabry, "On the Application of Interference Phenomena to the Solution of Various Problems of Spectroscopy and Metrology," *Astrophysical Journal*, vol. 9, no. 87, 1899.
- [45] K. L. Chopra, *Thin Film Phenomena*, New York: McGraw-Hill Book Company, 1969.
- [46] Y. Hishikawa, N. Nakamura, S. Tsuda, S. Nakano, Y. Kishi and Y. Kuwana, "Interference-Free Determination of the Optical Absorption Coefficient and the Optical Gap of Amorphous Silicon Thin Films," *Japanese Journal of Applied Physics*, vol. 30, no. 5, pp. 1008-1014, 1991.

- [47] J. Tauc, "Optical properties and electronic structure of amorphous Ge and Si," *Materials Research Bulletin*, vol. 3, no. 1, pp. 37-46, 1968.
- [48] Y. P. Varshni, "Temperature Dependence of the Energy Gap in Semiconductors," *Physica*, vol. 34, pp. 149-154, 1967.
- [49] Y. Jin, B. Song, Z. Jia, Y. Zhang, C. Lin, X. Wang and S. Dai, "Improvement of Swanepoel method for deriving the thickness and the optical properties of chalcogenide thin films," *Optics Express*, vol. 25, no. 1, pp. 440-451, 2017.
- [50] N. Ravindra, P. Ganapathy and J. Choi, "Energy gap–refractive index relations in semiconductors – An overview," *Infrared Physics & Technology*, vol. 20, pp. 21-29, 2007.
- [51] S.K.Tripathy, "Refractive indices of semiconductors from energy gaps," *Optical Materials*, vol. 46, pp. 240-246, 2015.
- [52] B. Zhu, H. Zeng, J. Dai, Z. Gong and X. Cui, "Anomalously robust valley polarization and valley coherence in bilayer WS₂," *Proceedings of the National Academy of Sciences*, vol. 11, no. 32, pp. 11606-11611, 2014.
- [53] L. Makinistian and E. A. Albanesi, "On the band gap location and core spectra of orthorhombic IV-VI compounds SnS and SnSe," *Physica Status Solidi B*, vol. 246, no. 1, pp. 183-191, 2009.
- [54] D. K. Ferry, "Chapter 2 Electronic Structure," in *Semiconductors Bonds and Bands*, Bristol, IOP Publishing Ltd, 2013, p. 1.
- [55] F. Zocchi and V. Piacente, "Sublimation enthalpy of tin monoselenide," *Journal of Materials Science Letters*, vol. 14, pp. 235-237, 1995.
- [56] Q. Li, A. Wei, J. Lu, L. Tao, Y. Yang, D. Luo, J. Liu, Y. Xiao, Y. Zhao and J. Li, "Synthesis of Submillimeter-Scale Single Crystal Stannous Sulfide Nanoplates for Visible and Near-Infrared Photodetectors with Ultrahigh Responsivity," *Advanced Electronic Materials*, vol. 4, no. 7, p. 1800154, 2018.
- [57] J.-H. Ahn, M.-J. Lee, H. Heo, J. H. Sung, K. Kim, H. Hwang and M.-H. Jo, "Deterministic Two-Dimensional Polymorphism Growth of Hexagonal n-Type SnS₂ and Orthorhombic p-Type SnS Crystals," *Nano Letters*, vol. 15, pp. 3703-3708, 2015.
- [58] E.Schönherr and W.Stetter, "Growth germanium monosulfide single crystals by sublimation," *Journal of Crystal Growth*, vol. 30, no. 1, pp. 96-98, 1975.
- [59] M. Vollmer, K.-P. Möllmann and J. A. Shaw, "The optics and physics of near infrared imaging," in *Education and Training in Optics and Photonics*, Bordeaux, 2015.

- [60] M. Zhang, J. Wu, Y. Zhu, D. O. Dumcenco, J. Hong, N. Mao, S. Deng, Y. Chen, Y. Yang, C. Jin, S. H. Chaki, Y.-S. Huang, J. Zhang and L. Xie, "Two-Dimensional Molybdenum Tungsten Diselenide Alloys Photoluminescence Raman Scattering and Electrical Transport," *ACS Nano*, vol. 8, no. 7, p. 7130–7137, 2014.
- [61] Y. Chen, D. O. Dumcenco, Y. Zhu, X. Zhang, N. Mao, Q. Feng, M. Zhang, J. Zhang, P.-H. Tan, Y.-S. Huang and L. Xie, "Composition-dependent Raman modes of Mo_{1-x}W_xS₂ monolayer alloys," *Nanoscale*, vol. 6, p. 2833, 2014.
- [62] S. Susarla, A. Kutana, J. A. Hachtel, V. Kochat, A. Apte, R. Vajtai, J. C. Idrobo, B. I. Yakobson, C. S. Tiwary and P. M. Ajayan, "Quaternary 2D Transition Metal Dichalcogenides (TMDs) with Tunable Bandgap," *Advanced Materials*, vol. 29, no. 35, p. 1702457, 2017.
- [63] Q. Feng, N. Mao, J. Wu, H. Xu, C. Wang, J. Zhang and L. Xie, "Growth of MoS₂(1-x)Se_{2x} (x = 0.41–1.00) Monolayer Alloys with Controlled Morphology by Physical Vapor Deposition," *ACS Nano*, vol. 9, no. 7, p. 7450–7455, 2015.
- [64] C. S. Jung, F. Shojaei, K. Park, J. Y. Oh, H. S. Im, D. M. Jang, J. Park and H. S. Kang, "Red-to-Ultraviolet Emission Tuning of Two-Dimensional Gallium Sulfide/Selenide," *ACS Nano*, vol. 9, no. 10, p. 9585–9593, 2015.
- [65] I. Vurgaftman and J. R. Meyer, "Band parameters for III–V compound semiconductors and their alloys," *Journal of Applied Physics*, vol. 89, p. 5815, 2001.
- [66] L. Vegard, "Die Konstitution der Mischkristalle und die Raumfüllung der Atome," *Zeitschrift für Physik*, vol. 17, p. 5, 1921.
- [67] R. E. Nahory, M. A. Pollack, W. D. Johnston and R. L. Barns, "Band gap versus composition and demonstration of Vegard's law for In_{1-x}Ga_xAs_yP_{1-y} lattice matched to InP," *Applied Physics Letters*, vol. 33, p. 659, 1978.
- [68] S. Adachi, "II-V Ternary and Quaternary Compounds," in *Springer Handbook of Electronic and Photonic Materials*, Switzerland, Springer International Publishing, 2017, p. 733.
- [69] T. Schmidt, K. Lischka and W. Zulehner, "Excitation-power dependence of the near-band-edge photoluminescence of semiconductors," *Physical Review B*, vol. 16, no. 45, pp. 8989-8994, 1992.
- [70] V. A. Fonoberov, K. A. Alim, A. A. Balandin, F. Xiu and J. Liu, "Photoluminescence investigation of the carrier recombination processes in ZnO quantum dots and nanocrystals," *Physical Review B*, vol. 73, no. 165317, 2006.

- [71] Z. Xiao, F.-Y. Ran, H. Hosono and T. Kamiya, "Route to n-type doping in SnS," *Applied Physics Letters*, vol. 106, p. 152103, 2015.
- [72] S. Hao, V. P. Dravid, M. G. Kanatzidis and C. Wolverton, "Research Update: Prediction of high figure of merit plateau in SnS and solid solution of (Pb,Sn)S," *APL Materials*, vol. 4, p. 104505, 2016.
- [73] H. R. Chandrasekhar, R. G. Humphreys, U. Zwick and M. Cardona, "Infrared and Raman spectra of the IV-VI compounds SnS and SnSe," *Physical Review B*, vol. 15, no. 4, pp. 2177-2183, 1977.
- [74] T. H. Patel, R. Vaidya and S. G. Patel, "Anisotropic behaviour of semiconducting tin monosulphoselenide single crystals," *Bulletin of Materials Science*, vol. 26, no. 6, pp. 569-574, 2003.
- [75] G. Kresse and J. Furthmüller, "Efficient iterative schemes for ab initio total-energy calculations using a plane-wave basis set," *Physical Review B*, vol. 54, p. 11169-11186, 1996.
- [76] P. E. Blöchl, "Projector augmented-wave method," *Physical Review B*, vol. 50, p. 17953-17979, 1994.
- [77] K. T. R. Reddy, N. K. Reddy and R. W. Miles, "Photovoltaic properties of SnS based solar cells," *Solar Energy Materials & Solar Cells*, vol. 90, p. 3041-3046, 2006.
- [78] W. Albers, C. Haas, H. J. Vink and J. D. Wasscher, "Investigations on SnS," *Journal of Applied Physics*, vol. 32, no. 10, pp. 2220-2225, 1961.
- [79] P. Sinsersuksakul, L. Sun, S. W. Lee, H. H. Park, S. B. Kim, C. Yang and R. G. Gordon, "Overcoming Efficiency Limitations of SnS-Based Solar Cells," *Advanced Energy Materials*, vol. 4, p. 1400496, 2014.
- [80] B. Wang, S. P. Zhong, Z. B. Zhang, Z. Q. Zheng, Y. P. Zhang and H. Zhang, "Broadband photodetectors based on 2D group IVA metal chalcogenides semiconductors," *Applied Materials Today*, vol. 15, pp. 115-138, 2019.
- [81] T. S. Reddy and M. C. S. Kumar, "Co-evaporated SnS thin films for visible light photodetector applications," *RSC Advances*, vol. 6, p. 95680, 2016.
- [82] A. J. Biacchi, S. T. Le, B. G. Alberding, J. A. Hagmann, S. J. Pookpanratana, E. J. Heilweil, C. A. Richter and A. R. H. Walker, "Contact and Noncontact Measurement of Electronic Transport in Individual 2D SnS Colloidal Semiconductor Nanocrystals," *ACS Nano*, vol. 12, pp. 10045-10060, 2018.

- [83] J. He, D. He, Y. Wang, Q. Cui, M. Z. Bellus, H.-Y. Chiu and H. Zhao, "Exceptional and Anisotropic Transport Properties of Photocarriers in Black Phosphorus," *ACS Nano*, vol. 9, no. 7, p. 6436–6442, 2015.
- [84] Z. Tian, C. Guo, M. Zhao, R. Li and J. Xue, "Two-Dimensional SnS: A Phosphorene Analogue with Strong In-Plane Electronic Anisotropy," *ACS Nano*, vol. 11, no. 2, pp. 2219-2226, 2017.
- [85] Z. Zhang, J. Yang, K. Zhang, S. Chen, F. Mei and G. Shen, "Anisotropic photoresponse of layered 2D SnS-based near infrared photodetectors," *Journal of Materials Chemistry C*, vol. 5, p. 11288, 2017.
- [86] J. Bullock, M. Amani, J. Cho, Y.-Z. Chen, G. H. Ahn, V. Adinolfi, V. R. Shrestha, Y. Gao, K. B. Crozier, Y.-L. Chueh and A. Javey, "Polarization-resolved black phosphorus/molybdenum disulfide mid-wave infrared photodiodes with high detectivity at room temperature," *Nature Photonics*, vol. 12, pp. 601-607, 2018.
- [87] H. A. Hashem and S. Abouelhassan, "Dielectric and Thermodynamic Properties of Tin (II) Sulfide Thin Films," *Chinese Journal of Physics*, vol. 43, p. 5, 2005.
- [88] Y. Kumagai, L. A. Burton, A. Walsh and F. Oba, "Electronic Structure and Defect Physics of Tin Sulfides: SnS, Sn₂S₃, and SnS₂," *Physical Review Applied*, vol. 6, p. 014009, 2016.
- [89] P. Bhattacharya, A. D. Stiff-Roberts and S. Chakrabarti, "Mid-infrared Quantum Dot Photodetectors," in *Mid-infrared Semiconductor Optoelectronics*, London, Springer, 1006, pp. 487-513.
- [90] H. Yuan, X. Li, F. Afshinmanesh, W. Li, G. Xu, J. Sun, B. Lian, A. G. Curto, G. Ye, Y. Hikita, Z. Shen, S.-C. Zhang, X. Chen, M. Brongersma, H. Y. Hwang and Y. Cui, "Polarization-sensitive broadband photodetector using a black phosphorus vertical p–n junction," *Nature Nanotechnology*, vol. 10, pp. 707-713, 2015.
- [91] E. Zhang, P. Wang, Z. Li, H. Wang, C. Song, C. Huang, Z.-G. Chen, L. Yang, K. Zhang, S. Lu, W. Wang, S. Liu, H. Fang, X. Zhou, H. Yan, J. Zou, X. Wan, P. Zhou, W. Hu and F. Xiu, "Tunable Ambipolar Polarization-Sensitive Photodetectors Based on High-Anisotropy ReSe₂ Nanosheets," *ACS Nano*, vol. 10, p. 8067–8077, 2016.
- [92] L. Li, P. Gong, D. Sheng, S. Wang, W. Wang, X. Zhu, X. Shi, F. Wang, W. Han, S. Yang, K. Liu, H. Li and T. Zhai, "Highly In-Plane Anisotropic 2D GeAs₂ for Polarization-Sensitive Photodetection," *Advanced Materials*, vol. 30, no. 50, p. 1804541, 2018.

- [93] X. Zhou, L. Gan, W. Tian, Q. Zhang, S. Jin, H. Li and Y. Bando, "Ultrathin SnSe 2 Flakes Grown by Chemical Vapor Deposition for High-Performance Photodetectors," *Advanced Materials*, vol. 27, p. 8035–8041, 2015.
- [94] H. Wang and D. H. Kim, "Perovskite-based photodetectors: materials and devices," *Chemical Society Reviews*, vol. 46, p. 5204, 2017.
- [95] O. Lopez-Sanchez, D. Lembke, M. Kayci, A. Radenovic and A. Kis, "Ultrasensitive photodetectors based on monolayer MoS₂," *Nature Nanotechnology*, vol. 8, pp. 497-501, 2013.
- [96] G. H. Heilmeyer and S. E. Harrison, "Implications of the Intensity Dependence of Photoconductivity in Metal-Free Phthalocyanine Crystals," *Journal of Applied Physics*, vol. 34, no. 9, p. 2732, 1963.
- [97] C. Hu, "Electrons and Holes in Semiconductors," in *Modern Semiconductor Devices for Integrated Circuits*, Prentice Hall, 2010, pp. 1-34.
- [98] R. H. Bube, *Photoconductivity of solids*, New York: Wiley, 1960.
- [99] M. Buscema, J. O. Island, D. J. Groenendijk, S. I. Blanter, G. A. Steele, H. S. J. v. d. Zant and A. Castellanos-Gomez, "Photocurrent generation with two-dimensional van der Waals semiconductors," *Chemical Society Reviews*, vol. 44, p. 3691, 2015.
- [100] S. Sucharitakul, U. R. Kumar, R. Sankar, F.-C. Chou, Y.-T. Chen, C. Wang, C. He, R. He and X. P. A. Gao, "Screening limited switching performance of multilayer 2D semiconductor FETs: the case for SnS," *Nanoscale*, vol. 8, p. 19050, 2016.
- [101] R. Fei, W. Kang and L. Yang, "Ferroelectricity and Phase Transitions in Monolayer Group-IV Monochalcogenides," *Physical Review Letters*, vol. 117, p. 097601, 2016.
- [102] M. Wu and X. C. Zeng, "Intrinsic Ferroelasticity and/or Multiferroicity in Two-Dimensional Phosphorene and Phosphorene Analogues," *Nano Letters*, vol. 16, pp. 3236-3241, 2016.
- [103] X.-W. Shen, W.-Y. Tong, S.-J. Gong and C.-G. Duan, "Electrically tunable polarizer based on 2D orthorhombic ferrovalley materials," *2D Materials*, vol. 5, p. 011001, 2018.
- [104] M. Liu, L. Wang, L. Zhou, S. Lei, J. Joyner, Y. Yang, R. Vajtai, P. Ajayan, B. I. Yakobson and P. Spanos, "Characterization of tin(II) sulfide defects/vacancies and correlation with their photocurrent," *Nano Research*, vol. 10, no. 1, pp. 218-228, 2017.

- [105] G. Wang, L. Bouet, D. Lagarde, M. Vidal, A. Balocchi, T. Amand, X. Marie and B. Urbaszek, "Valley dynamics probed through charged and neutral exciton emission in monolayer WSe₂," *Physical Review B*, vol. 90, no. 075413, 2014.
- [106] D. Sun, J.-W. Lai, J.-C. Ma, Q.-S. Wang and J. Liu, "Review of ultrafast spectroscopy studies of valley carrier dynamics in two-dimensional semiconducting transition metal dichalcogenides," *Chinese Physics B*, vol. 26, no. 3, p. 037801, 2017.
- [107] D. Lagarde, L. Bouet, X. Marie, C. R. Zhu, B. L. Liu, T. Amand, P. H. Tan and B. Urbaszek, "Carrier and Polarization Dynamics in Monolayer MoS₂," *Physical Review Letters*, vol. 112, p. 047401, 2014.
- [108] C. Mai, A. Barrette, Y. Yu, Y. G. Semenov, K. W. Kim, L. Cao and K. Gundogdu, "Many-Body Effects in Valleytronics: Direct Measurement of Valley Lifetimes in Single-Layer MoS₂," *Nano Letters*, vol. 14, pp. 202-206, 2014.
- [109] T. Hong, B. Chamlagain, W. Lin, H.-J. Chuang, M. Pan, Z. Zhou and Y.-Q. Xu, "Polarized photocurrent response in black phosphorus field-effect transistors," *Nanoscale*, vol. 6, p. 8978, 2014.